Theoretical Studies of Structural and Electronic Properties of Donor-Acceptor Polymers

DISSERTATION

zur Erlangung des akademischen Grades

Doctor rerum naturalium
(Dr. rer. nat.)

vorgelegt

dem Bereich Mathematik und Naturwissenschaften
der Technischen Universität Dresden

von

M. Sc. Florian Günther

geboren am 05.12.1989 in Karl-Marx-Stadt

Eingereicht am 26.04.2018
Verteidigt am 05.07.2018

Gutachter:	Prof. Dr. Gotthard Seifert
	Prof. Dr. Sibylle Gemming

Diese Dissertation wurde in der Zeit von 10/2013 bis 04/2018 im Institut für Physikalische Chemie der TU Dresden und dem Helmholtz-Zentrum Dresden-Rossendorf e.V. angefertigt.

ACKNOWLEDGEMENTS

This thesis has been carried out with great support from my colleagues, my friends, and my family to whom I express my deepest acknowledgments. I cordially thank my supervisors **Prof. Dr. Sibylle Gemming** and **Prof. Dr. Gotthard Seifert** for giving me the opportunity to carry out the studies reported in this thesis. They guided me throughout this work, supported me in my research interests, and always had an open ear for me. An equivalent thanks goes to **Dr. Anton Kiriy**, who also provided inspiring ideas and constant support to my work.

Since funding is an important issue in science, it is a pleasure for me to thank the *Helmholtz-Zentrum Dresden-Rossendorf e.V.* (**HZDR**) and the cluster of excellence *Center for Advancing Electronics Dresden* (**cfaed**) of the *Technische Universität Dresden* for financing my PhD position. Special thanks goes to cfaed for supporting my first research stay at the *University of São Paulo* (USP) in São Carlos, Brazil, with the Inspire Grant. Furthermore, I thank the *Deutscher Akademischer Austauschdienst e.V.* (**DAAD**) for financing my exchange year at the USP São Carlos with a scholarship. I am moreover very thankful for getting support by the *International Helmholtz Research school* **NanoNet** of HZDR.

During my time as PhD student, I collaborated with a lot of excellent scientists from different institutes who I would like to thank. In particular, I want to mention **Dr. Tim Erdmann**, **Dr. Yevhen Karpov**, **M.Sc. Dmitry Skidin**, who provided me with some experimental data for my thesis.

In sciences, extensive discussions are one key for obtaining profound knowledge. Because of this, I thank all my colleagues who shared numerous coffee and lunch breaks with me and used the opportunity to give helpful advice and critical remarks to my research. In particular, I would like to mention in random order: **Dr. Tommy Lorenz, Dr. Jeffrey Kelling, Dr. Jan-Ole Joswig, M.Sc. Lokamani, M.Sc. David Teich, and Dr. Diana Tranka**. A special thanks goes to **Dr. Jens Kunstmann**, **Dr. Igor Baburin** and **Prof. Arnulf Möbius** for proofreading parts of this thesis. I am also grateful to **Dipl.-Phys. Knut Vietze** for his kind and patient support in computer-technical questions and to **Antje Völkel** and **Susann Gebel** for their help with administration tasks.

I furthermore express my deepest thanks to **Prof. Dr. Ubirajara Pereira Rodrigues-Filho** and his group for their hospitality during my visits in Brazil, especially to **Mateus B. Simões** and to **Prof. Hidetake Imasato**. In the time of my stays in São Carlos, I did not only learn a lot of new skills, but also found many new friends and collaboration partners.

Finally, I thank my parents **Maj and Steffen Günther** and my whole family for their moral support for the duration of my studies, especially during my stays abroad. Last but not least, I want to conclude by extending heartfelt gratitude to my beautiful fiancée **Mariana Simões Floria** for her unconditional love. Without her constant motivation and support, I would not have taken important opportunities.

ABSTRACT

The development of new electronic devices requires the design of novel materials since the existing technologies are not suitable for all applications. In recent years, semiconducting polymers (SCPs) have evolved as fundamental components for the next generation of costumer electronics. They provide interesting features, especially flexibility, light weight, optical transparency and low-cost processability from solution.

The research presented in this thesis was devoted to theoretical studies of donor-acceptor (DA) copolymers formed by electron-deficient 3,6-(dithiophene-2-yl)-diketopyrrolo[3,4-c]pyrrole (TDPP) and different electron-rich thiophene compounds. This novel type of SCPs has received a lot of attention due to experimental reports on very good electronic properties which yielded record values for organic field-effect transistor applications. In order to get a deeper understanding of the structural and electronic properties, the main objective of this work was to study this material type on the atomic scale by means of electronic structure methods. For this, density functional theory (DFT) methods were used as they are efficient tools to consider the complex molecular structure.

This work comprises three main parts: a comparative study of the structural and the electronic properties of TDPP based DA polymers obtained by means of different theory levels, the calculation of the intermolecular charge transfer between π-π stacked DA polymer chains based on the Marcus transfer theory and investigations of molecular p-doping of TDPP based DA polymers. For the first, DFT using different functionals was compared to the density functional based tight binding (DFTB) method, which is computationally very efficient. Although differences in structural properties were observed, the DFTB method was found to be the best choice to study DA polymers in the crystalline phase. For the second, correlations between the molecular structure and the reorganization energy are found. Moreover, the dependency of the electronic coupling element on the spatial shape of the frontier orbitals is shown. Furthermore, a Boltzmann-type statistical approach is introduced in order to enable a qualitative comparison of different isomers and chemical structures. For the last part, the p-doping properties of small, multi-polar dopant molecules with local dipole provided by cyano groups were investigated theoretically and compared with experimental observations. The one with the strongest p-doping properties was studied in this work for the first time on a theoretical basis. Comparing these different p-dopants, rich evidence was found supporting the experimentally observed doping strength.

CONTENTS

I Introduction 1

1 Organic Semiconductors 3

1.1 Novel Materials for New Electronic Devices 3

1.2 Semiconducting Polymers 4

1.3 Donor-Acceptor Polymers 5

1.4 Concept of Doping in Conjugated Polymers 7

2 Motivation and Goal 9

2.1 Motivation 9

2.2 Objectives of the Work 10

2.3 Outline 10

II Theory and Methods 13

3 Electronic Structure Theory 15

3.1 Fundamentals of Quantum Mechanics 15

3.1.1 The Schrödinger Equation 15

3.1.2 Born-Oppenheimer Approximation 16

3.1.3 Periodic Boundary Conditions 17

3.2 Density Functional Theory 18

3.2.1 Introduction 18

3.2.2 Hohenberg-Kohn Theorems 19

3.2.3 The Kohn-Sham Equations 19

3.2.4 Exchange-Correlation Functionals 21

3.2.5 Basis Sets 21

3.2.6 Population Analyses 22
3.3 Density Functional based Tight Binding 24
3.4 Further Aspects 26
3.4.1 Geometry Optimization 26
3.4.2 Dispersion Interaction in DFT Methods 27

4 Modeling of the Electronic Transport 29
4.1 Introduction 29
4.2 Electrical Conductivity 29
4.3 Marcus Transfer Theory 30
4.3.1 Introduction 30
4.3.2 General Theory 31
4.3.3 The Fragment Approach 33
4.3.4 The Reorganization Energy 33
4.3.5 The Electronic Coupling Element 34

III Results 37

5 Geometry and Electronic Structure of Monomer and Oligomer Models 39
5.1 Introduction 39
5.2 Computational Details 40
5.3 Structural Aspects 41
5.3.1 Monomer Model of TDPP 41
5.3.2 Thiophene Compounds 44
5.3.3 Oligomer Models of Thieno[3,2-b]thiophene 46
5.3.4 Interactions in 2,2′:5′,2″-terthieno[3,2-b]thiophene Dimers 48
5.3.5 Analysis of STM Images 50
5.4 Electronic Structure of TDPP-TT models 54
5.4.1 The Monomer Model 54
5.4.2 Oligomer and Polymer Models 56
5.5 Summary and Conclusions 60

6 Inter-molecular Charge Transfer between Donor-Acceptor Polymers 61
6.1 Introduction 61
6.2 Computational Details 62
6.2.1 Molecular Models 62
6.2.2 Methods and Parameters 63
6.2.3 Working Strategy 64
6.3 The Reorganization Energy 65
6.4 The Coupling Element 66
6.4.1 Dependence on the Stacking Geometry 66
6.4.2 Average Value Approaches 71

6.5 Transfer Rates and Mobilities 73
6.6 Summary and Conclusions 75

7 Molecular p-Doping of Donor-Acceptor Polymers 77
7.1 Introduction 77
7.2 Observations from Experiment 79
7.3 Computational Details 80
7.4 Isolated Models 81
7.5 Charge Transfer and Formation Energies 82
7.6 Electronic Structure of CT Complexes 86
7.7 Summary and Conclusions 91

IV Summary 93

8 Conclusions and Future Prospectives 95
8.1 Overview 95
8.2 Conclusions 96
  8.2.1 Geometry and Electronic Structure of Monomer and Oligomer Models 96
  8.2.2 Inter-molecular Charge Transfer between Donor-Acceptor Polymers 97
  8.2.3 Molecular p-Doping of Donor-Acceptor Polymers 97
8.3 Outlook 98

V Appendix 101

A Derivation of the Marcus Formula 103
A.1 One-Dimensional Reaction Coordinate 103
A.2 Multi-Dimensional Reaction Coordinate 105

B Simple One-Dimensional Quantum Well Model 107

C Benchmarks for the Calculation the of Coupling Element 111

D Average Value Approaches of the Coupling Element 115

E Doping Properties in F4-TCNQ:4T Complexes 117

Bibliography 121

List of Figures 143

List of Tables 147

List of Abbreviations 149

Part I

Introduction

1 ORGANIC SEMICONDUCTORS

1.1 NOVEL MATERIALS FOR NEW ELECTRONIC DEVICES

Our daily life is strongly influenced by and based on electronic devices. More and more inventions are introduced and combined with existing technologies to improve their performance, to make them more user-friendly or to be applicable in new fields. The visions of our future are guided by self-driving cars, smart homes and other intelligent devices that are meant to make our life easier. However, for the development of such technologies, the currently used materials such as bulk semiconductors might not be suitable in all cases. Therefore, novel materials have to be designed to render such applications possible.

Organic semiconductors are one class of these new types of materials. Due to their inherent plastic properties, in particular flexibility, light weight, optical transparency, and low-cost processability from solution, they are evolving as promising candidates for a new generation of consumer electronics. Thereby, field-effect transistors (OFETs) [1–4], organic solar cells (OSCs) [5, 6], and organic light-emitting diodes (OLEDs) [4] are the major developments in the field of organic electronics (OEs). Other devices, such as radio-frequency identification tags [7], organic electrochromic devices [8], thermoelectric generators [9, 10], batteries [11, 12] and sensors [13] support the idea that organic material can provide all functionalities required for electronics.

On macroscopic scale, semiconductor materials are mainly characterized by two quantities: the charge carrier mobility μ and the charge carrier density η [14, 15]. Their product is proportional to the electrical conductivity σ, which denotes the electric current caused by an electric field. Among others, it affects the on-off current ratio in a transistor device. In general, a large value of σ and consequently large values of μ and η are desired. Moreover, the mobility determines how fast the charge carriers drift through the active area and therefore substantially influences the maximum switching frequencies.

The efficiency of organic semiconductors, however, is much lower than the one of conventional materials. While crystalline silicon exhibits mobilities above 10^3 cm^{2}V^{-1}s^{-1} [16], organic materials yield values which are three and more orders of magnitude smaller. Therefore, it is nowadays supposed that OEs will enable new electronic consumer applications rather than substitute the existing silicon technologies [17, 18]. For instance, the concepts of wearable electronics [19, 20] and e-papers [21] do not profit from fast processors, but from other properties such as flexibility, cheap production, and light weight [17]. Hence, organic semiconductors are intensively studied and the corresponding device performances are tried to be improved as much as possible. Especially, the development of OFETs with enhanced electrical properties is expected to be trend-setting as they are required as fundamental switching units in printed logic circuits [22, 23]. Moreover, investigating OFETs also provides important insights into the charge transport properties in semiconducting materials [24]. Therefore, designing novel materials with improved features is a major research task in OEs.

1.2 SEMICONDUCTING POLYMERS

Polymers form a remarkable class of compounds. They are long chain-like molecules consisting of well-defined repeat units, the spatial alignment of which are typically limited to a short range. On the one hand, common polymers such as polyethylene, polyvinylchloride or polyethylene-terephthalate are well known as flexible thin foils being electrically insulating [25]. On the other hand, so-called conjugated polymers, which exhibit backbones of alternating single and double bonds, have been found to show electrically conductive behavior. Here, the linkage of aromatic units leads to the formation of a delocalized electronic π-system which enables an electronic transport through the systems. Moreover, the energy gap between the highest occupied molecular orbital (HOMO) and the lowest unoccupied molecular orbital (LUMO) shrinks in comparison to the non-polymerized compounds. Partial oxidation, referred to as doping in this context, results in an increase of σ by several orders of magnitude, exceeding the range of semiconductors (10^{-6} Sm^{-1} $< \sigma <$ 10^{2} Sm^{-1}) and reaching the performance of metallic conductors (10^{2} Sm^{-1} $< \sigma <$ 10^{8} Sm^{-1}) [26–29]. This discovery by MacDiarmid, Shirakawa and Heeger was honored with the Nobel Prize in chemistry in 2000 [30] because it opened the door to the rapidly growing field of semiconducting polymers (SCPs).

The first generation of SCPs, such as polyacetylene (PA), poly(p-phenylene) (PPP), polythiophene (PT), polypyrrole (PPy), polyaniline (PANI), and poly(ethylene dioxythiophene) (PEDOT), was based on a π-conjugated backbone only [26], see Fig. 1.1. Especially electrical conductivity upon doping was studied on these early representatives. However, they show a low solubility and are therefore difficult to process. To overcome this difficulty, the representatives of the second generation of SCPs were equipped with solubilizing side-chains. The resulting

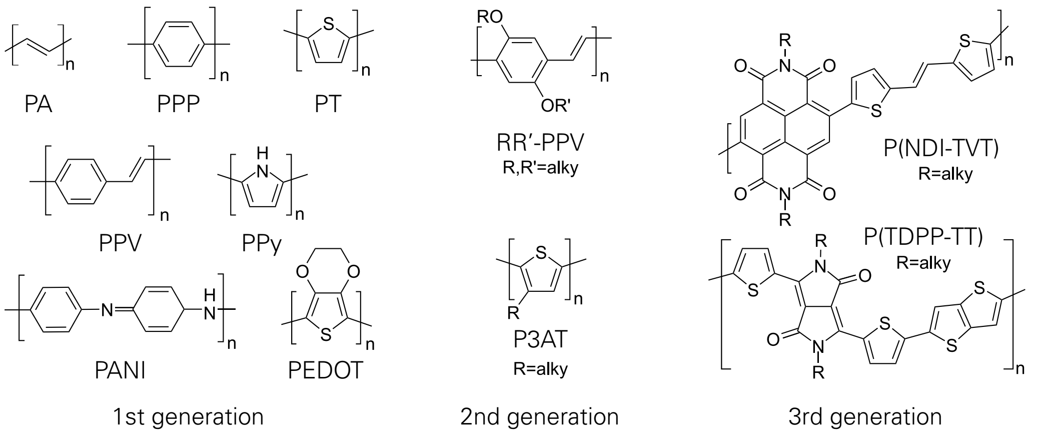

Figure 1.1: Most common representatives of the 1st, 2nd and 3rd generation of SCP.

poly(2,5-dialkoxy-p-phenylene vinylene)s (RR′-PPVs) and poly(3-alkylthiophene)s (P3ATs) became the most studied materials in this area. The improved solubility ensured a more controlled synthesis leading to less structural defects and molecular weight. This subsequently resulted in better ordering in the thin-film state, presenting a semi-crystalline lamellar structure [31]. Further developments of controlled chain growth polymerization methods allowed additional improvements of the thin-film microstructures and consequently raised the hole mobility from 10^{-5} to 0.1 $cm^2V^{-1}s^{-1}$ [32–34]. This made poly(3-hexylthiophene) (P3HT) to be the benchmark system for semiconducting organic materials for several years. The large electron concentration in thiophene compounds, however, leads to high-lying HOMO energies and hence to a facile oxidation by air and other electron acceptors [35–37]. Therefore, new chemical structures have been designed in order to reduce the number of electron-donating atoms or substituents. This resulted in new solution-processable PTs, such as polyquarterthiophene or poly(2,5-bis(3-alkylthiophen-2-yl)thieno-[3,2-b]thiophene)s. Based on these approaches, the hole mobility could be increased to the remarkable value of 1.0 $cm^2V^{-1}s^{-1}$ [38, 39].

1.3 DONOR-ACCEPTOR POLYMERS

Another approach to reduce the oxidation propensity is lowering the HOMO energy by incorporating electron-deficient co-monomers into the polymer skeleton. This yielded the third generation of SCPs and to donor-acceptor (DA) polymers [40]. Typically, the HOMO of such an alternating co-polymer system is mainly determined by the electron-rich component, while the LUMO resembles more that of the electron-poor component [41]. Besides the reduced HOMO energy, DA polymers also exhibit smaller band gaps, because the conjugation of electron-rich and electron-poor units facilitate orbital hybridization. Hence, this material class is not only interesting for OFET but also for OSC applications [41].

Figure 1.2 schematically depicts the HOMO and LUMO energies of 2,2′-bithiophene

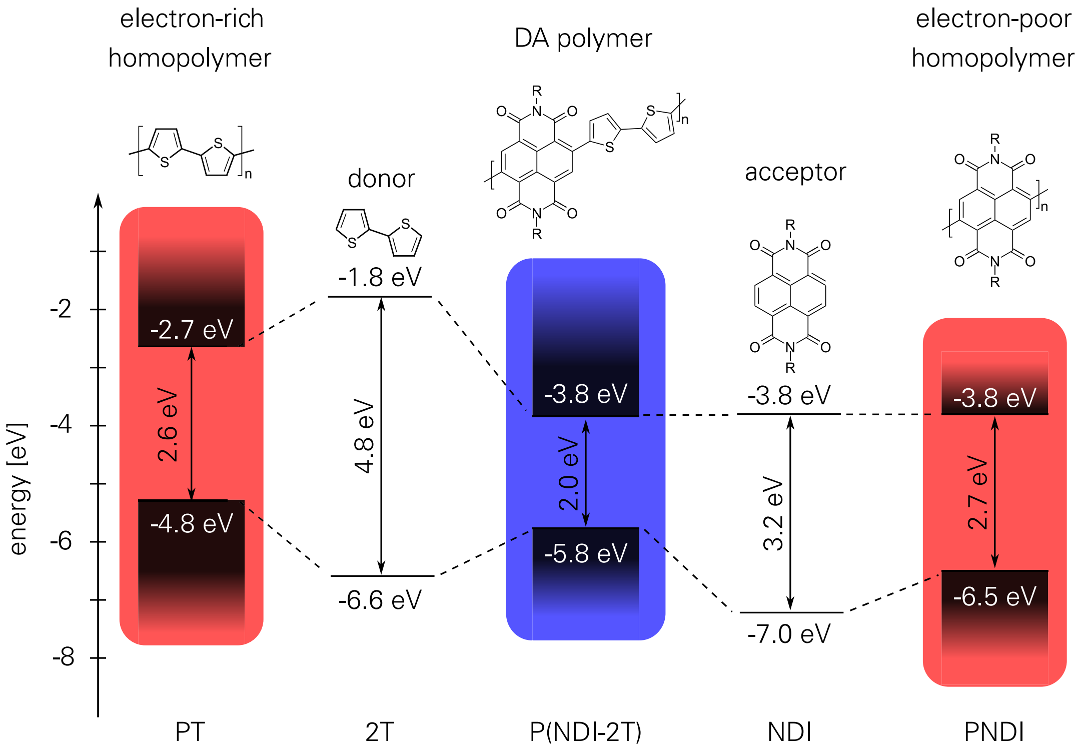
electron-rich homopolymer
DA polymer
electron-poor homopolymer
donor
acceptor
energy [eV]
-2
-4
-6
-8
-2.7 eV
2.6 eV
-4.8 eV
-1.8 eV
4.8 eV
-6.6 eV
-3.8 eV
2.0 eV
-5.8 eV
-3.8 eV
3.2 eV
-7.0 eV
-3.8 eV
2.7 eV
-6.5 eV
PT
2T
P(NDI-2T)
NDI
PNDI

Figure 1.2: Energy level diagram of the frontier orbital of 2T [42] and NDI [43] in comparison to the corresponding homopolymers PT [44] and PNDI [45], as well as to the DA copolymer P(NDI-2T) [46]. The electron-rich PT exhibits a high-lying and the electron-poor PNDI a low-lying HOMO, whereas the DA copolymer P(NDI-2T) yields an HOMO energy in between and a reduced band gap.

(2T) and naphthalenetetracarboxylic diimide (NDI). The corresponding homopolymers PT and poly(naphthalenetetracarboxylic-diimide) (PNDI) yield high and low-lying HOMO levels of −4.8 eV [44] and −6.5 eV [45], respectively. On the contrary, the DA copolymer poly(naphthalenetetracarboxylic-diimide-bithiophene) (P(NDI-2T)) exhibits a HOMO of −5.8 eV [46], as it is desired for good transistor performances [1]. Moreover, reduced band gap compared to the homopolymer cases is obtained. With this type of SCP, an electron mobility above 1.0 $cm^2V^{-1}s^{-1}$ could be obtained [47, 48].

Recently, another system has received a lot of attention as acceptor moiety. In 2012, Ong *et al.* reported on a DA copolymer from TDPP as acceptor and thieno[3,2-b]thiophene (TT) as donor. This P(TDPP-TT) copolymer yielded excellent hole mobilities of up to 10.5 $cm^2V^{-1}s^{-1}$ [49]. Further modifications of the chemical structure, such as optimizing the solubilizing side-chains, replacing thiophene by pyridine units or considering other thiophene based compounds as donor moiety enabled the fabrication of semiconducting films with efficient ambipolar transport properties [50, 51].

1.4 CONCEPT OF DOPING IN CONJUGATED POLYMERS

Most of π-conjugated polymers in their pristine state possess rather low electrical conductivity values because of a small number of intrinsic charge carriers and the low charge carrier mobility. In order to increase the charge carrier density, additional electron-withdrawing or electron-donating components can be admixed to the semiconducting material. This process, which is referred to as molecular or chemical doping, distinguishes itself from the conventional doping of bulk semiconductors. While the doping of silicon means substitution of atoms in a covalently bound lattice, molecular doping of conjugated polymers generally refers to charge transfer occurring between molecular components in a film. This intermolecular type of doping, where the dopant is not covalently bound to the semiconducting host, opens possibilities for many different geometrical configurations, exhibiting different degrees of electronic interaction and resulting in a variation in doping efficiency [52]. Hence, the underlying concept of the charge transfer (CT) from the dopant to the semiconductor is different in nature compared to the doping of inorganic systems.

In order to describe the interaction between the dopant and the organic semiconductor material, two models have been proposed: the integer CT model and the hybrid CT complex model [53]. In the first case, p-type doping occurs when the dopant LUMO level lies below the HOMO of the polymer and the electronic levels do not hybridize. In this picture, an electron is transferred from the SCP to the dopant, resulting in the formation

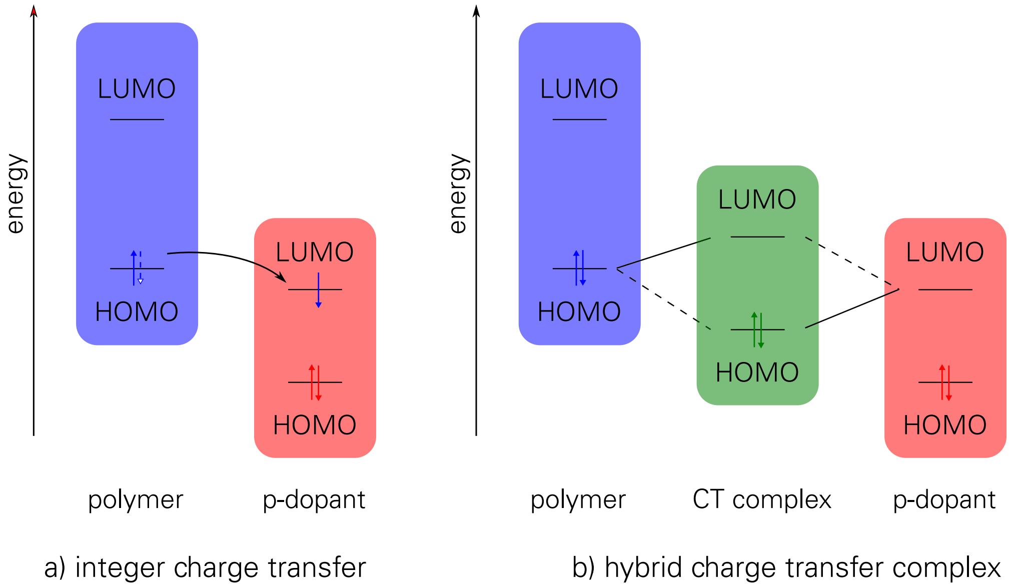

a) integer charge transfer b) hybrid charge transfer complex

Figure 1.3: Schematic sketch of the two models used to describe molecular p-doping. In the integer CT model (a), an electron is completely transferred and occupies the LUMO of the dopant, while a hole is created in the polymer. In case of the hybrid CT complex model (b) new electronic states are formed. Here, the CT is characterized by the contribution of the individual compounds to the hybridized orbitals.

of a hole in the semiconducting region, see Fig. 1.3 a). Rich evidence in favor of this model has been reported [54–56]. The second model considers the formation of new electronic levels as hybridization of the dopant and the polymer orbitals. Here, the CT is characterized by the contribution of the individual compounds to these wave functions of the CT complex. Numerous examples for CT complexes have been reported, but only a few for conjugated π-systems [55].

2 MOTIVATION AND GOAL

2.1 MOTIVATION

Since the discovery of conductive polymers [26–29], OEs have established themselves as their own field in both academia and industry. Over the past years, the performances of OE devices have been tremendously enhanced by the invention of new synthesis strategies, by improved device fabrication methods and by selective designs of novel chemical structures. However, there is still a long way ahead to realize the new applications as they had been promised by the leading scientists of the area [17, 18, 57].

Besides experimental developments such as advanced fabrication techniques and improved device architectures, theoretical models are needed which enable scientists to predict the most suitable material for a given application. In order to develop such an approach, however, it is first necessary to evaluate if a proposed model is able to predict the physical properties of a system with a given molecular structure. This task is particularly challenging since the morphologies of organic materials vary from highly ordered crystalline to highly disordered amorphous structures. In these two opposite cases, the underlying transport mechanisms are typically characterized by different quantities. Analyzing the impact of the chemical structure on the transport-defining quantities and comparing the obtained results with experimental observations is the first step necessary to decide whether or not a model is appropriate to describe the electronic transport in SCPs. In case of mismatches, the model, the simulation approaches or the experimental treatments have to be refined.

The research reported in this thesis has been motivated by the discovery of TDPP-based DA polymers and their high record mobility values. This has raised the question in which way the molecular structure affects the transport properties when considered on a theoretical basis. Moreover, this research was performed in collaboration with experimental groups involved in the synthesis and the characterization of these materials.

2.2 OBJECTIVES OF THE WORK

Despite intensive investigations on TDPP-based DA polymers, a systematic study of the electronic structure with focus on the impact of the molecular structure has not been performed so far, although it should gives important insight into the charge transport in this class of materials. Thus, the major aim of this work is to consider these materials on a theoretical basis and to analyze their electronic properties.

An appropriate theory level has to be chosen which is capable of handling the complex molecular structure in an efficient, but yet accurate way. Since the transport properties are particularly sensitive to conformational changes—especially to deviations from the planarity of the conjugated system—stereo chemical aspects have to be carefully analyzed. The insights gained from these investigations can help to design new molecular structures with the structural aspects favoring desired physical properties. Moreover, the charge transport in DA copolymer films had to be modeled. Here, the hopping transfer between π-π-stacked chains is the bottleneck for achieving charge transport on the macroscopic scale. Modeling this electronic transfer and determining its dependency on the molecular structure is therefore another objective of the present thesis. Furthermore, the molecular doping of TDPP-based DA polymers systems have to be considered on a theoretical basis. For the recently evolved third generation SCPs, new challenges arise compared to the first and second generation SCPs. One of them is the dependency of the doping strength on the positioning of the dopant with respect to the donor and acceptor moieties. Hence, the CT has to be systematically studied and different CT complexes formations have to be considered.

The objectives of this work can be grouped into three main parts:

1. to perform a comparative study of intra- and inter-molecular interactions which govern the geometry and the electronic structure of TDPP based DA copolymers
2. to look for correlations between the molecular design and the inter-chain charge transfer rates in π-π stacks
3. to carry out a systematic investigation of the charge transfer between molecular p-dopants and π-conjugated DA copolymer systems

2.3 OUTLINE

This thesis is organized as follows: In the next part, the theoretical background and the used computational methods are briefly introduced. Chapter 3 gives an overview on the fundamentals of quantum-mechanics and on *first principles* methods. In particular, density functional theory (DFT) methods are discussed since they were mainly used throughout this work. In Chapter 4, the concepts of electronic transport are described. Here, the focus is on the Marcus transfer theory, a frequently used approach to model a number of important processes, e.g. the calculation the CT in conjugated systems.

Because of this the corresponding transport formula is derived and its applicability discussed. Furthermore, the fragment approach is introduced which enables accessing the required quantities by DFT methods.

The third part of this thesis includes the obtained results and their discussions in line with the three objectives stated in Section 2.2. In Chapter 5, the stereochemical aspects of TDPP and thiophene based systems are analyzed by means of different *first principles* methods. Here, the main focus is on the mutual alignment of subunits within a chain. Planarity is particularly important, not only in view of justifying the model of π-π stacked chains, but also with respect to real systems since non-planar structures show higher disorder and therefore worse electronic properties. For this reason, the twisted configurations are studied in detail with an emphasis on the model size and on the interactions in π-π stacked systems. Moreover, the electronic structure and the contributions of the donor and acceptor moieties to the molecular orbitals are analyzed. In the sixth chapter, the intermolecular CT between π-π stacked DA polymer chains is studied employing the Marcus transfer theory. The required quantities are calculated and their dependencies on the molecular structure are discussed. In the last chapter of part three, the molecular p-doping of P(TDPP-TT) is considered as a case study for DA copolymers. For this, different small, multi-polar dopant molecules with local dipole provided by cyano groups are investigated and HOMO and LUMO of isolated models and CT complex structures are considered.

Finally, the work is summarized and concluded in the last part of the thesis, Chapter 8. Moreover, an outlook of potential further investigations is given.

Part II

Theory and Methods

3 ELECTRONIC STRUCTURE THEORY

3.1 FUNDAMENTALS OF QUANTUM MECHANICS

3.1.1 The Schrödinger Equation

In quantum-mechanics, the many-body wave function $|\Psi\rangle$ fully characterizes all properties of a physical system [58]. In general, it is a complex function which depends on the time t, all the spatial coordinates $\{\vec{r}_i\}$ and other degrees of freedom of the particles.

The main equation to determine the wave function in a non-relativistic theory is the so-called Schrödinger equation [59]:

$$\widehat{H}\,|\Psi\rangle = (\widehat{T} + \widehat{V})\,|\Psi\rangle = \left(\sum_i -\frac{\hbar^2}{2m_i}\frac{\partial^2}{\partial \vec{r}_i^{\,2}} + \widehat{V}(\{\vec{r}_i\}, t)\right)|\Psi\rangle = \mathrm{i}\hbar\frac{\partial}{\partial t}\,|\Psi\rangle \ . \tag{3.1}$$

It arises from the classical Hamilton function, where the quantum mechanical operators of location $\hat{\vec{r}}_i$, linear momentum $\hat{\vec{p}}_i$ and energy $\hat{E}$ are substituted for the corresponding terms of classical physics.

If the potential $\widehat{V}$ does not explicitly depend on the time, the following product ansatz can be used:

$$\left|\Psi(\{\vec{r}_i\}, t)\right\rangle = \left|\Psi_r(\{\vec{r}_i\})\right\rangle |\Psi_t(t)\rangle \ . \tag{3.2}$$

This leads to the so-called stationary Schrödinger equation,

$$\widehat{H}\left|\Psi_r(\{\vec{r}_i\})\right\rangle = E\left|\Psi_r(\{\vec{r}_i\})\right\rangle \ , \tag{3.3}$$

where E is a real number. It can be interpreted as the total energy of the system being described by the quantum mechanical state $|\Psi\rangle$.

3.1.2 Born-Oppenheimer Approximation

In systems relevant for chemistry, the considered particles are the electrons and the nuclei so that the Hamiltonian can be written as

$$\widehat{H} = \widehat{T}_e + \widehat{T}_n + \widehat{V}_{ee} + \widehat{V}_{en} + \widehat{V}_{nn} \,. \tag{3.4}$$

Here, $\widehat{T}_e$ and $\widehat{T}_n$ are the kinetic energy operators for the electrons and the nuclei, respectively, whereas $\widehat{V}_{ee}$, $\widehat{V}_{en}$ and $\widehat{V}_{nn}$ are the potentials that describe the electron-electron, electron-nucleus and nucleus-nucleus interactions.

Since the masses of the nuclei are several orders of magnitudes larger than those of electrons, the core motions happen on a larger time scale. Hence, the nuclei can hypothetically be considered as in rest [60]. Employing a product ansatz to decouple the wave function into an electronic and a nuclear part,

$$|\Psi_r\rangle = \left|\Psi_r^{\mathrm{e}}(\{\vec{r}_i\})\right\rangle \left|\Psi_r^{\mathrm{n}}(\{\vec{R}_\alpha\})\right\rangle \,, \tag{3.5}$$

yields the electronic Schrödinger Equation,

$$\left(\widehat{T}_e(\{\vec{r}_i\}) + \widehat{V}_{en}(\{\vec{r}_i\}, \{\vec{R}_\alpha\}) + \widehat{V}_{ee}(\{\vec{r}_i\})\right) \left|\Psi_r^{\mathrm{e}}(\{\vec{r}_i\})\right\rangle = \hat{H}_e \left|\Psi_r^{\mathrm{e}}(\{\vec{r}_i\})\right\rangle = E_e \left|\Psi_r^{\mathrm{e}}(\{\vec{r}_i\})\right\rangle \,, \tag{3.6}$$

and the Schrödinger equation for the nuclei,

$$\left(\widehat{T}_n(\{\vec{R}_\alpha\}) + \widehat{V}_{nn}(\{\vec{R}_\alpha\}) - E_e\right) \left|\Psi_r^{\mathrm{n}}(\{\vec{R}_\alpha\})\right\rangle = E \left|\Psi_r^{\mathrm{n}}(\{\vec{R}_\alpha\})\right\rangle \,. \tag{3.7}$$

Considering the positions of the nuclei as constant parameters, the electronic wave function $\left|\Psi_r^{\mathrm{e}}(\{\vec{r}_i\})\right\rangle$ and the electronic energy E_e are uniquely defined for any set of $\{\vec{R}_\alpha\}$. Treating the cores as classically resting objects, the total energy is given by the sum of the electronic part and the repulsion of the nuclei,

$$E_{tot} = E_e(\{\vec{R}_\alpha\}) + V_{nn}(\{\vec{R}_\alpha\}) \,. \tag{3.8}$$

The wave function $\left|\Psi_r^{\mathrm{e}}(\{\vec{r}_i\})\right\rangle$ depends on the whole set of electronic coordinates $\{\vec{r}_i\}$. In quantum chemistry, this many-body problem is translated into a picture where each electron is described by an individual single-particle wave function $|\psi_i\rangle$ which is referred to as orbital. For this, the single-particle Schrödinger equation,

$$\hat{h}\,|\psi_i\rangle = \epsilon_i\,|\psi_i\rangle \,, \tag{3.9}$$

is considered. Due to the Pauli principle, each of these electronic state can be occupied once—or twice according to the spin degeneration. In the ground state, the orbitals with the lowest eigenenergies are filled in line with the aufbau principle. The energy between the highest occupied and the lowest unoccupied state is called the Fermi energy ϵ_F.

3.1.3 Periodic Boundary Conditions

In order to describe a system which shows a well-defined structure, such as crystals or conjugated polymers, periodic systems can be studied [61]. In these models, surface or termination effects are suppressed and an ideal infinite system is described. Moreover, the total number of atoms is reduced compared to large systems. A periodic potential, however, yields further properties of the eigenfunctions $|\psi\rangle$ and eigenvalues of the Schrödinger equation.

The Bloch-Theorem [62, 63] states that for a potential with translational symmetry, $V(\vec{r}) = V(\vec{r} + \vec{R})$, the corresponding Schrödinger equation yields a set of eigenfunctions,

$$\psi_{\vec{k}}(\vec{r}) = \exp\left(\mathrm{i}\vec{k}\vec{r}\right) u(\vec{r}), \tag{3.10}$$

where $u(\vec{r})$ is a periodic function with the same periodicity as the potential, $u(\vec{r}) = u(\vec{r} + \vec{R})$. Furthermore, the eigenvalues $\epsilon_{\vec{k}}$ are dependent on the index vector $\vec{k}$, which is called crystal momentum or quasi momentum. This dependency is the basis for the band structure model. Note that the mapping from $\vec{k}$ to $\psi_{\vec{k}}$ and $\epsilon_{\vec{k}}$ is not unique. Due to the periodicity of the perfactor $\exp\left(\mathrm{i}\vec{k}\vec{r}\right)$, only values for which $\left|\vec{k}\vec{r}\right| \leq \pi/2$ holds have to be considered. The corresponding region of the k-space is called first Brillouin zone. Depending on the space group of the system, high symmetry points can be classified. By definition, the Γ point corresponds to $\vec{k} = (0, 0, 0)$ whereas others are located at the boundary of the first Brillouin zone.

When two quantum systems couple, a bonding and an anti-bonding state are formed [15, 61, 64], where the first is always lower in energy, see Fig. 3.1. When more systems are combined, this concept proceeds so that the wave function with the lowest eigenenergy shows the smallest number of nodal surfaces and the one with the highest exhibits nodes between each subsystem. For an infinite extended system, this behavior is captured by $\vec{k}$. The corresponding eigenvalues $\epsilon_{\vec{k}}$ form a continuous spectrum, the band structure. Similar to the non-periodic case, these bands are filled according to the total number of electrons within the system. The last filled band is called the valence band and the first unoccupied one is referred to as the conduction band.

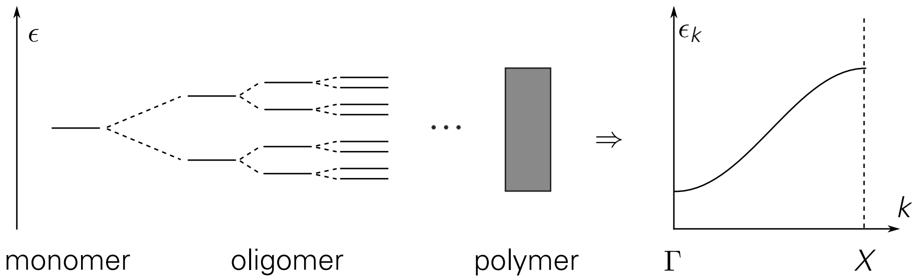

Figure 3.1: Schematic plot of the transition from an energetic state of a monomer to the electronic band structure of an one-dimensional periodic structure.

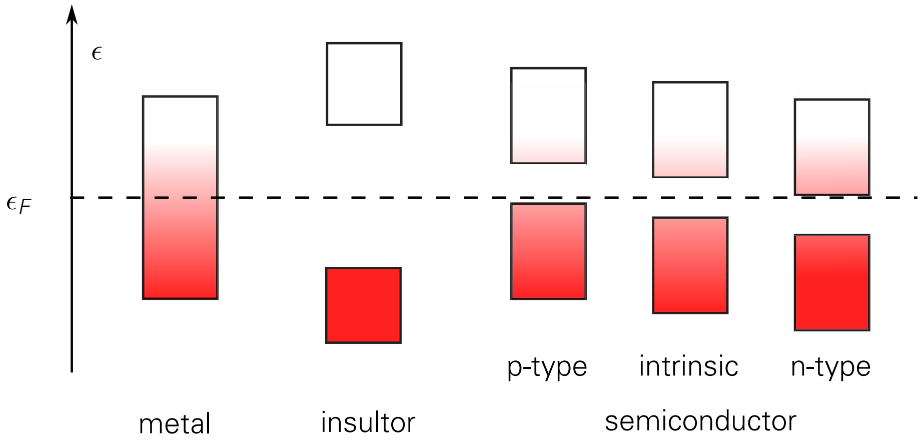

Figure 3.2: Schematic presentation of the electronic bands of metals, insulators and semiconductors depending on the band gap and the position of the Fermi energy ϵ_F. The shading represents the occupation according to the Fermi-Dirac statistics [64].

As depicted in Fig. 3.2, the electronic properties of a material can be classified according to the positioning of the Fermi energy and the gap between the valence and the conduction band [15, 61, 64]. When the Fermi energy lies within a band, the electrons can easily be excited into states above ϵ_F as it is described by the Fermi-Dirac distribution [15, 61, 64]. These electrons—the holes created by the excitation—behave like free particles. As a consequence, the material is an electronic conductor and is therefore considered a metal. When ϵ_F lies in between two bands, the system is an insulator, because no free charge carrier is available. However, excitations to the valence band by thermal or optical effects are still possible if the band gap is small. These materials are called semiconductors and are the key to modern electronics. By doping the material with additional electron-donating or electron-withdrawing compounds the position of the Fermi energy is modified. In this case, one type of charge carriers—electrons or holes—is dominant leading to n-type or p-type semiconductors.

3.2 DENSITY FUNCTIONAL THEORY

3.2.1 Introduction

The main task of quantum-chemical methods is to determine the electronic energy E_e and the electronic wave function $|\Psi\rangle$ for a given number of electrons N_e and a given number of nuclei N_α with positions $\vec{R}_\alpha$. For this the electronic many-particle Schrödinger equation, Eq. (3.6), has to be solved. Once it is found, $|\Psi\rangle$ can be used to calculate all physical properties of the system, e.g. electronic transport or optical properties. Among the large number of different quantum mechanical approaches, the present thesis uses density functional theory (DFT) methods [65, 66]. In this section, their basic ideas are therefore briefly described.

Instead of attempting to approximate the many-body wave function $|\Psi\rangle$ as it is done by *ab initio* approaches, DFT is based on the electronic density ρ, which is defined as

$$\rho(\vec{r}) = N_e \int |\Psi(\vec{r}, \vec{r}_2, \vec{r}_3, \dots, \vec{r}_{N_e})|^2 \mathrm{d}^3 r_2 \mathrm{d}^3 r_3 \dots \mathrm{d}^3 r_{N_e} \,. \tag{3.11}$$

A more detailed knowledge of the many-particle wave function is not necessary and consequently enables the calculation of larger molecular systems at much lower computational costs. Because of this, DFT has become a very popular alternative to the *ab initio* methods.

3.2.2 Hohenberg-Kohn Theorems

In 1964, Hohenberg and Kohn formulated and proved the following two theorems [67]:

1st Hohenberg-Kohn theorem. *The external potential V_{ext} and thus the total energy, is an unique functional of the electron density $\rho(\vec{r})$.*

2nd Hohenberg-Kohn theorem. *The density that minimizes the total energy is the exact ground state density.*

The first Hohenberg-Kohn theorem states that the electronic part of the energy can be written as

$$E_{\text{DFT}}[\rho(r)] = F[\rho(r)] + E_{\text{ext}}[\rho(r)] \,. \tag{3.12}$$

Therein, the second term corresponds to the interaction of the electrons and the external potential V_{ext} generated by the nuclei,

$$E_{\text{ext}}[\rho] = \int \rho(\vec{r}) V_{\text{ext}}(\vec{r}) \mathrm{d}^3 r \quad \text{with} \quad V_{\text{ext}}(\vec{r}) = \sum_{\alpha}^{N_n} \frac{Z_\alpha}{|\vec{r} - \vec{R}_\alpha|} \,. \tag{3.13}$$

The functional $F[\rho]$ is an universal but unknown functional that comprises all inner interaction of the system. These are the kinetic part of the energy $T[\rho]$ and the electron-electron interaction $E_{ee}[\rho]$,

$$F[\rho] = T[\rho] + E_{ee}[\rho] \,. \tag{3.14}$$

The second theorem gives a starting point to deduce the ground state density and hence all other properties of the system. Since there is no analytical expression for $F[\rho]$, however, a few further assumptions have to be made first.

3.2.3 The Kohn-Sham Equations

In 1965, Kohn and Sham developed a scheme that approximates the functional $F[\rho]$ by expressing the charge density ρ as the sum of the absolute square of single-particle wave functions $\left|\psi_i^{\mathrm{KS}}\right\rangle$ [68],

$$\rho(\vec{r}) = \sum_{i=1}^{N_e} \left|\psi_i^{\mathrm{KS}}\right|^2 . \tag{3.15}$$

These so-called Kohn-Sham (KS) orbitals describe a system of non-interacting electrons but with the same density as the "real" system. For $\left|\psi_i^{\mathrm{KS}}\right\rangle$, the kinetic energy can be expressed via

$$T_{\mathrm{KS}} = \sum_{i=1}^{N_e} \left\langle \psi_i^{\mathrm{KS}} \middle| \hat{t} \middle| \psi_i^{\mathrm{KS}} \right\rangle = -\frac{1}{2} \sum_{i=1}^{N_e} \left\langle \psi_i^{\mathrm{KS}} \middle| \frac{\partial^2}{\partial \vec{r}^2} \middle| \psi_i^{\mathrm{KS}} \right\rangle . \tag{3.16}$$

The difference of the "real" kinetic energy and this approximation is mainly determined by the correlation $T_C[\rho]$.

The energy term $E_{ee}[\rho]$ from Eq. (3.14) can be written as the sum of a mean-field interaction of the electrons, the so-called Hartree term $E_{\mathrm{H}}[\rho]$, and a second term, which comprises all remaining interactions and is mainly governed by the exchange interactions $E_{\mathrm{X}}[\rho]$. With this, Eq. (3.12) can be rewritten as

$$E_{\mathrm{DFT}}[\rho(r)] = T_{\mathrm{KS}} + E_H[\rho(r)] + E_{\mathrm{ext}}[\rho(r)] + \underbrace{T_C[\rho(r)] + E_{\mathrm{X}}[\rho(r)]}_{=E_{\mathrm{XC}}[\rho(r)]} . \tag{3.17}$$

Therein, T_{KS} is given by Eq. (3.16), $E_{\mathrm{ext}}[\rho(r)]$ by Eq. (3.13) and $E_H[\rho(r)]$ by

$$E_H[\rho(\vec{r})] = \frac{1}{2} \int \rho(\vec{r}) V_{\mathrm{H}}[\rho(\vec{r})] \mathrm{d}^3 r \quad \text{with} \quad V_H[\rho(\vec{r})] = \int \frac{\rho(\vec{r}')}{|\vec{r} - \vec{r}'|} \mathrm{d}^3 r' . \tag{3.18}$$

The unknown terms $T_C[\rho(r)]$ and $E_{\mathrm{X}}[\rho(r)]$ are combined to the so-called exchange-correlation (XC) functional $E_{\mathrm{XC}}[\rho(r)]$. Up to this point, DFT is formally seen as an exact theory, as all interactions which are not considered yet or described wrongly can be incorporated in $E_{\mathrm{XC}}[\rho(r)]$.

Inserting Eq. (3.15) to Eq. (3.17) enables the application of the variation principle with respect to $|\psi_i\rangle$. That way, a set of single-particle equations is obtained, the so-called KS equations:

$$\hat{h}^{\mathrm{KS}} \left|\psi_i^{\mathrm{KS}}\right\rangle = \epsilon_i \left|\psi_i^{\mathrm{KS}}\right\rangle \quad \text{with} \quad \hat{h}^{\mathrm{KS}} = \hat{t} + V_{eff}^{\mathrm{KS}} , \tag{3.19}$$

and

$$V_{eff}^{\mathrm{KS}}[\rho(\vec{r})] = V_H[\rho(\vec{r})] + V_{\mathrm{ext}} + V_{\mathrm{XC}}[\rho(\vec{r})] \quad \text{with} \quad V_{\mathrm{XC}}[\rho(\vec{r})] = \frac{\partial}{\partial \rho} E_{\mathrm{XC}}[\rho(\vec{r})] . \tag{3.20}$$

The KS potential obtained has to be chosen in such a way that the resulting KS orbitals yield the ground state electron density of the real system. Multiplying Eq. (3.19) with $\left\langle\psi_i^{\mathrm{KS}}\right|$ and summing up all occupied states followed by comparing to Eq. (3.17), the total energy of the system can be formulated as[1]

$$E_{\mathrm{DFT}}[\rho(\vec{r})] = \sum_{i=1}^{N_e} \epsilon_i - E_{\mathrm{H}}[\rho(\vec{r})] + E_{\mathrm{XC}}[\rho(\vec{r})] - \int \rho(\vec{r}) V_{\mathrm{XC}}[\rho(\vec{r})] \mathrm{d}^3 r \,. \tag{3.21}$$

3.2.4 Exchange-Correlation Functionals

In order to apply the KS method to relevant systems, an expression for the unknown functional $E_{\mathrm{XC}}[\rho]$ is necessary. Over the years, many expressions were derived which can be grouped into three classes: local density approximation (LDA), generalized gradient approximation (GGA) and hybrid functionals.

In the first case, $E_{\mathrm{XC}}[\rho]$ is approached by using expressions of the homogeneous electron gas [69]. Here, the exchange E_{X} is exactly defined [69] whereas the correlation T_C can be approximated by functions obtained from many-body perturbation theory [70] or from fitting very accurate numerical quantum Monte-Carlo simulations [71]. The most common ones are the Vosko-Wilk-Nusair (VWN) [72], the Perdew-Zunger (PZ81) [73], the Cole-Perdew (CP) [74] and the Perdew-Wang (PW92) [75] correlation expressions.

The more accurate GGA functionals include the gradient and higher derivatives of $\rho(\vec{r})$ turning them computationally more expensive. Typically, exchange and correlation are again expressed in individual terms. The Becke-88 functional [76] is commonly considered for the exchange, whereas the functional of Lee, Yang and Parr [77] gives an expression for the correlation. Their combination is often referred to as BLYP functional. Another GGA functional was proposed by Perdew, Burke and Ernzerhof (PBE) [78]. It is known for its general applicability and produces accurate results for a wide range of systems.

Some important quantities, however, such as the binding energy, are overestimated by the functionals described so far. Apart from that, the Hartree-Fock (HF) method underestimates the binding energy, so that the idea of hybrid functionals is to mix these approaches. The most famous representative of this class is the B3LYP (Becke, three-parameter, Lee-Yang-Parr) functional, in which the LDA, the HF and the Becke GGA exchanges as well as the LDA and the LYP correlations are combined.

3.2.5 Basis Sets

In order to solve the analytic eigenvalue equation of DFT, numerical routines have to be used since analytical solutions are not possible. Thus, Eq. (3.19) has to be translated into a general algebraic eigenvalue problem. For that reason, a set of basis functions is introduced $\{|\varphi_n\rangle\}$ and the wave function is expressed as a linear combination. In case of a complete basis, which means i.a. considering an infinite number of basis functions, such a decomposition would be exact. In practice, however, only a finite number can be considered so that the obtained solutions are approximations only. In order to optimize them, the basis set has either to be very large or to be chosen carefully. Over the time, many different ideas of basis sets were discussed with different advantages concerning size, numerical handling or physical interpretation. Most common nowadays are local basis sets and plane waves, but projected augmented waves or muffin-tin orbitals are used as well [79].

---

[1] Note that $\sum_i \langle\psi_i| V |\psi_i\rangle = \int V \sum_i |\psi_i|^2 \mathrm{d}^3 r = \int V\rho \mathrm{d}^3 r$.

For systems on the atomic scale, it is practically useful to refer to the orbitals of the constituent atoms. Hence, the molecular orbitals (MOs) are expressed as a linear combination of atomic orbitals (LCAO),

$$|\psi_n\rangle = \sum_{\alpha} \sum_{i \in \alpha} c_{ni}^{(\alpha)} \left| \varphi_i^{(\alpha)} \right\rangle \tag{3.22}$$

where α labels the atoms and i the corresponding AOs. This enables a straightforward chemical interpretation of the results and is therefore used in the presented thesis.

Typically, either Gaussian-type orbitals (GTO),

$$\left| \varphi^{\mathrm{GTO}}(\vec{r}) \right\rangle \propto x^a y^b z^c e^{-\zeta r^2} \quad \text{with} \quad a + b + c = m, \tag{3.23}$$

or Slater-type orbitals (STO),

$$\left| \varphi^{\mathrm{STO}}(\vec{r}) \right\rangle \propto r^{n-1} \cdot e^{-\zeta r} Y_{lm} \left(\frac{\vec{r}}{r} \right), \tag{3.24}$$

are considered. Here, n, l and m are the quantum numbers of the corresponding atomic orbital (AO) and Y_{lm} the spherical harmonics. In both cases, the exponent ζ determines the decay of the basis function and has to be chosen for each atom and each combination of quantum numbers n and l.

When only one of these zeta-functions—either GTO or STO—is considered for each AO, the basis set is called single-zeta (SZ) or minimal basis. As to increase the number of basis functions and hence the quality of the obtained MOs, two or even three zeta-functions per AO can be considered. These basis sets are called double-zeta (DZ) or triple-zeta (TZ) basis sets, respectively. To allow the description of polarization effects, it is necessary to include further basis functions with a higher angular momentum l than the valence orbital. The resulting basis sets are called double-zeta polarised (DZP), triple-zeta polarised (TZP), triple-zeta douple-polarised (TZ2P), etc. Although the concept of these basis sets seems to be straightforward, it is differently implemented in each software package.

3.2.6 Population Analyses

One property which is important for the modeling and the understanding of interacting atoms is the concept of partially charged atoms. For this, the spatially distributed charge density $\rho(\vec{r})$ has to be "divided" among the atoms. When a LCAO basis is used, Eq. (3.22), the gross orbital population (GOP),

$$q_n^{(\alpha)} = \sum_{i\in\alpha}\sum_{\beta}\sum_{j\in\beta} c_{ni}^{(\alpha)} c_{nj}^{(\beta)} \left\langle \varphi_i^{(\alpha)} | \varphi_j^{(\beta)} \right\rangle , \tag{3.25}$$

can be used to calculate the contribution of an atom α to the MO $|\psi_n\rangle$

The Mulliken population [80, 81] assigns the electronic charge to a given atom α by summing the GOPs over the occupied states

$$q_{\text{Mulliken}}^{(\alpha)} = \sum_n q_n^{(\alpha)} . \tag{3.26}$$

Because of the dependence of the overlap $\left\langle \varphi_i^{(\alpha)} | \varphi_j^{(\beta)} \right\rangle$, $q_{\text{Mulliken}}^{(\alpha)}$ strongly dependents on the choice of the basis set. As a consequence, the Mulliken approach is not the proper choice to derive partial charges when large and diffuse basis sets are used.

Another approach known to be basis independent is the Hirschfeld population analysis. Here, weight functions $w_\alpha(\vec{r})$ are introduced, given by the unrelaxed superposition of the atomic densities $\rho^{(\alpha)}$,

$$w_\alpha^{\text{H}}(\vec{r}) = \frac{\rho^{(\alpha)}(\vec{r}_\alpha)}{\sum_\beta \rho^{(\beta)}(\vec{r}_\beta)} \quad \text{with} \quad \vec{r}_\alpha = \vec{r} - \vec{R}_\alpha . \tag{3.27}$$

With this, the Hirschfeld population is given by

$$q_{\text{Hirschfeld}}^{(\alpha)} = \int \rho(\vec{r}) w_\alpha^{\text{H}}(\vec{r}) \mathrm{d}\vec{r} . \tag{3.28}$$

Another class of population analyses can be formulated in a similar manner, but the weight functions w_α are chosen as

$$w_\alpha(\vec{r}) = \begin{cases} 1 & , \vec{r} \in \Omega_\alpha \\ 0 & , \text{else} \end{cases} . \tag{3.29}$$

Therein, the whole space is divided into cells Ω_α which contain exactly one atom α. The density within each cell is then attributed to the corresponding atoms. The easiest way to do so is the so-called Voronoi population analysis [82]. Here, the division of the space follows the same construction method as the Wigner-Seitz cell. This means, planes are drawn which perpendicularly bisect the lines in between the atoms.

Additionally to the versions described so far, many other methods such as natural bond order, Bader analyses, etc. exist. All of them have different properties and advantages for specific applications. In general, however, it should also be noted that none of them can be the ultimate analysis, since the picture of partial charges is a simplified model of the spatially distributed density.

3.3 DENSITY FUNCTIONAL BASED TIGHT BINDING

The density functional based tight binding (DFTB) [83–92] method can be understood as an approximate DFT scheme which keeps the essential features of the KS approach. By introducing simplifications, the corresponding Schrödinger equation has the same structure as the one of non-orthogonal tight binding or extended Hückel theory. However, the important advantage is that all matrix elements are calculated within KS DFT. DFTB has the computational speed of traditional semi-empirical quantum chemical methods but without demanding a large number of empirical parameters. Over the years, the DFTB approach has been systematically improved including a self-consistent charge extension (SCC-DFTB) [87], a formulation for the spin-dependent calculations [90] and a time-dependent description of excited states [91]. Nowadays, it is well qualified for the efficient calculation of structures and electronic properties of numerous systems including large molecules, clusters and solids.

The main approximations utilized are the following: First, according to Foulkes and Haydock [93], the density ρ is expressed with respect to a reference density ρ_0 and a fluctuation $\delta\rho$. Both of them are expressed as a superposition of spherical, atom centered terms $\rho^{(\alpha)}$ and $\delta\rho^{(\alpha)}$, respectively. Moreover, $E_{\mathrm{XC}}[\rho_0 + \delta\rho]$ is expanded in a Taylor series up to the second-order term

$$E_{\mathrm{XC}}[\rho_0+\delta\rho] \approx E_{\mathrm{XC}}[\rho_0] + \int \underbrace{\frac{\partial}{\partial\rho}E_{\mathrm{XC}}\bigg|_{\rho_0}}_{=V_{\mathrm{XC}}[\rho_0]} \delta\rho \mathrm{d}\vec{r} + \frac{1}{2}\iint \frac{\partial^2}{\partial\rho\partial\rho'}V_{XC}\bigg|_{\rho_0} \delta\rho \mathrm{d}\vec{r}\mathrm{d}\vec{r}' \tag{3.30}$$

With this, the total energy can be written as

$$\begin{aligned} E_{tot} \approx & \sum_i \langle\psi_i|\,\hat{t} + V_{\mathrm{ext}} + V_{\mathrm{H}}[\rho_0] + V_{\mathrm{XC}}[\rho_0]\,|\psi_i\rangle \\ & \underbrace{+\frac{1}{2}\iint \frac{\partial^2}{\partial\rho\partial\rho'}V_{\mathrm{XC}}\bigg|_{\rho_0} \delta\rho(\vec{r})\delta\rho(\vec{r}')\mathrm{d}\vec{r}\mathrm{d}\vec{r}' + \frac{1}{2}\iint \frac{\delta\rho(\vec{r})\delta\rho(\vec{r}')}{|\vec{r}-\vec{r}'|}\mathrm{d}\vec{r}\mathrm{d}\vec{r}'}_{=E_{2nd}} \\ & \underbrace{-E_{\mathrm{H}}[\rho_0] + E_{\mathrm{XC}}[\rho_0] - \int V_{\mathrm{XC}}[\rho_0(\vec{r})]\rho_0(\vec{r})\mathrm{d}\vec{r} + V_{nn}}_{=E_{rep}}\,. \end{aligned} \tag{3.31}$$

Second, the effective KS potential $V_{eff}^{\mathrm{KS}}[\rho_0]$ is expressed as a superposition of spherical, atom centered terms that correspond to the potentials of neutral atoms $V^{(\alpha)}$ with the atomic densities $\rho^{(\alpha)}$[2]

$$V_{eff}^{\mathrm{KS}}[\rho_0] = \sum_\alpha V^{(\alpha)}[\rho^{(\alpha)}(r_\alpha)] \quad \text{with} \quad r_\alpha = |\vec{r} - \vec{R}_\alpha|\,. \tag{3.32}$$

---

[2] This decomposition is obviously possible for V_{ext} and V_{H}. For V_{XC}, however, this is an approximation due to its non-linearity.

Third, a minimal valence basis is used, whereas the orthogonalization to the core states is kept by considering pseudo potentials. Assuming "weak" pseudo potentials, the corresponding terms, namely the crystal field and the three center terms, can be neglected so that only two center terms remain.

The fourth and last major simplification does not affect the calculation of the electronic part of the energy, but the total energy. The last line of Eq. (3.31) defines the repulsive energy. Due to the decomposition of the potentials into atomic parts, E_{rep} can be expressed as a sum of pairwise contributions. Although it is formally possible to access these terms directly, in practice they are fitted to full DFT calculations. However, it is particularly important to do these fits for appropriate reference systems, which describe the individual atoms with proper chemical environments.

Altogether, the secular equation which has to be solved is given by

$$\sum_i H_{ij} c_{in} = \epsilon_n^{\mathrm{DFTB}} S_{ij} c_{in} \, , \tag{3.33}$$

with

$$S_{ij} = \left\langle \varphi_j^{(\beta)} | \varphi_i^{(\alpha)} \right\rangle \, . \tag{3.34}$$

When the density fluctuation and consequently the contribution of E_{2nd} are neglected, the Hamilton matrix of DFTB is found as

$$H_{ij}^{\mathrm{DFTB}} = \begin{cases} \epsilon^{\mathrm{atom}} & , i = j \\ \left\langle \varphi_j^{(\beta)} \middle| \hat{t} + V^{(\alpha)}[\rho^{(\alpha)}] + V^{(\beta)}[\rho^{(\beta)}] \middle| \varphi_i^{(\alpha)} \right\rangle & , \beta \neq \alpha \\ 0 & , \text{else} \end{cases} \, . \tag{3.35}$$

Therein, ϵ^{atom} are the orbital energies of the isolated atoms and $V^{(\alpha)}[\rho^{(\alpha)}]$ the KS potentials of the neutral atoms. The basis functions $\left|\varphi_i^{(\alpha)}\right\rangle$ in the equations (3.34) and (3.35) are pseudo AOs which are obtained by solving the following KS equations:

$$\left[\hat{t} + V^{(\alpha)} + \left(\frac{r}{r_0} \right)^2 \right] \left| \varphi_i^{(\alpha)} \right\rangle = \tilde{\epsilon} \left| \varphi_i^{(\alpha)} \right\rangle \, . \tag{3.36}$$

The contraction potential $\left(\frac{r}{r_0}\right)^2$ has been added to form a more efficient basis set for molecular and solid-state systems, as introduced by Eschrig and coworkers [94, 95]. Here, r_0 is usually chosen as 1.85 up to 2.00 times the covalent radius of the atom. This results in basis functions which decay faster and therefore lead to smaller long-range contributions.

The Eqns. (3.34) and (3.35) consist of two-center integrals only. Therefore, they can be calculated and tabulated in advance as functions of the distance between atomic pairs. Thus, it is not necessary to recalculate any integral during an actual DFTB calculation. The pairwise tabulated integrals have to be transformed to the specific coordinate system by transformations of the angle-dependent part of the basis functions [96].

In order to take the second-order terms E_{2nd} into account, the charge fluctuations $\delta\rho^{(\alpha)}$

are required. In line with the minimal valence basis ansatz, the most obvious way to define $\delta\rho^{(\alpha)}$ is the Mulliken approach, see Section 3.2.6. One can show [87] that the Hamiltonian of the SCC-DFTB approach can be written as

$$H_{ij}^{\text{SCC-DFTB}} = H_{ij}^{\text{DFTB}} + \frac{1}{2} S_{ij} \sum_{\xi} \left(\gamma_{\alpha\xi} + \gamma_{\beta\xi}\right) \Delta q_{\xi} \quad \text{with} \quad i \in \alpha, j \in \beta \,. \tag{3.37}$$

where Δq_{ξ} is the charge of the atom ξ described by the corresponding fluctuation $\delta\rho^{(zeta)}$ and $\gamma_{\alpha\xi}$ a shorthand for the second derivative of the Hartree and exchange-correlation contributions with respect to charges. Since the charge Δq_{ξ} depend on the basis coefficients c_{in}, the eigenvalue problem in Eq. (3.33) has to be solved self-consistently. In contrast to a "full" DFT calculation, however, the self-consistency has to be achieved for the charges δq_{ξ} of the atoms instead of the charge density ρ. Such a restricted self-consistency is called a self-consistent charge (SCC) treatment.

In conclusion, (SCC-)DFTB is computationally more efficient than standard DFT methods, but requires much less empirical parameters than semi-empirical methods. Thus, it is very suitable to investigate the structural and electronic properties of large systems such as long polymer chains.

3.4 FURTHER ASPECTS

3.4.1 Geometry Optimization

Within the Born-Oppenheimer approximation, the total energy of an atomic system is defined for any given nuclei positions $\{\vec{R}_{\alpha}\}$. In order to find stable geometries of a chemical system, E_{tot} has to be minimized. For this purpose, numerics provide many strategies such as the steepest-decent method, conjugated gradients, the Broyden-Fletcher-Goldfarb-Shanno algorithm and more [97]. Most of them are based on the forces acting on the atoms which are given as the negative derivatives of the total energy with respect to the nuclei coordinates,

$$\vec{F}_{\alpha} = -\frac{\partial E_{tot}}{\partial \vec{R}_{\alpha}} = -\frac{\partial E_{e}}{\partial \vec{R}_{\alpha}} - \frac{\partial V_{nn}}{\partial \vec{R}_{\alpha}} \,. \tag{3.38}$$

Using the energy expression derived for DFT, Eq. (3.21), together with a LCAO basis, Eq. (3.22), one can show that the derivative of the basis coefficients c_{ni} can be eliminated and the remaining terms can be calculated analytically [98]. In particular, for the (SCC-)DFTB method the forces are given by [99]

$$\vec{F}_{\alpha} = -\sum_{n} \sum_{i,j} c_{ni} c_{nj} \left[\frac{\partial H_{ij}}{\partial \vec{R}_{\alpha}} - \epsilon_{n} \frac{\partial S_{ij}}{\partial \vec{R}_{\alpha}} \right] - \frac{\partial E_{rep}}{\partial \vec{R}_{\alpha}} . \tag{3.39}$$

Computing these derivatives can be performed efficiently, since the integrals and the repulsive potential ares stored in the tables.

3.4.2 Dispersion Interaction in DFT Methods

Dispersion interactions, although weak compared to chemical bonds, play a crucial role in a wide range of fields, e.g. in the π-π stacking of conjugated polymers. Standard DFT functionals, however, suffer from their inability to describe this interaction correctly. Although the E_{XC} must also include dispersion, commonly used LDA and GGA functionals do not cover the correlation between distant dipole density fluctuations [100]. Hence, they do not reproduce the well-known R^{-6} dependence of the dispersion interaction energy between two separate neutral fragments. In order to address this deficiency, various solutions have been proposed [100–106]. The easiest and most popular approach is adding an empirical term E_{disp} to the total energy.

In the widely-used Grimme dispersion [104, 105], the following expression is considered:

$$E_{\mathrm{disp}} = -s \sum_{\alpha \neq \beta} \frac{\sqrt{C_\alpha C_\beta}}{|\vec{R}_\alpha - \vec{R}_\beta|^6} f_d(|\vec{R}_\alpha - \vec{R}_\beta|) \,. \tag{3.40}$$

Therein, s is a global scaling factor, which adjusts the correction to the repulsive behavior of the chosen density functional. The function $f_d(R)$ is an appropriate step-function damping the R^{-6} dependency for small distances. The coefficients C_α are atomic parameters which are derived from the ionization potentials and the polarizability of each atom.

In the (SCC-)DFTB method, the dispersion energy is approximated in a similar way by considering pairwise Lennard-Jones potentials [103]. In order to suppress the R^{-12} singularity for short distances, where the interaction is already covered by the DFTB energy itself, the following expression is used:

$$E_{\mathrm{disp}}^{\alpha\beta}(R) = \begin{cases} d_{\alpha\beta}\left[-2\left(\frac{R_{\alpha\beta}}{R}\right)^6 + \left(\frac{R_{\alpha\beta}}{R}\right)^{12}\right] & , R \geq \frac{R_{\alpha\beta}}{\sqrt[6]{2}} \\ U_0 + U_1 R^5 + U_2 R^{10} & , R < \frac{R_{\alpha\beta}}{\sqrt[6]{2}} \end{cases} \,. \tag{3.41}$$

The parameters U_0, U_1 and U_2 are determined under the condition of a smooth potential. The depth $d_{\alpha\beta}$ and the distance $R_{\alpha\beta}$ are derived as geometrical mean value of atomic parameters which are taken from universal force-field parametrization [103, 107]. The total dispersion energy of the system is given by the sum over all pairwise contributions,

$$E_{\mathrm{disp}} = \frac{1}{2} \sum_{\alpha \neq \beta} E_{\mathrm{disp}}^{\alpha\beta}(|\vec{R}_\alpha - \vec{R}_\beta|) \,. \tag{3.42}$$

4 MODELING OF THE ELECTRONIC TRANSPORT

4.1 INTRODUCTION

In order to describe the transfer of electrons on a quantum mechanical level, two opposite extreme cases can be considered. On the one hand, the orbitals of the constituting units—typically atoms—have a large overlap leading to the formation of bonds and, for periodic systems, to the electronic band structure. In such a system, the electronic wave functions are delocalized over the system and can be modeled as (quasi-)free particles with an effective mass [61]. In this case, the transfer rate at which an electron moves from one side to the other is faster than the movements of the atoms. Due to this, the transfer can be considered of adiabatic nature.

On the other hand, in weakly bound systems the electrons localize at the different units and the transition to a neighboring center is described as a hopping process. In contrast to the first case, this transfer may involve changes in the geometry of the systems [108] so that the transfer is of non-adiabatic nature.

4.2 ELECTRICAL CONDUCTIVITY

To what extent a physical system is electrically conductive is described by the conductivity σ. It is defined as the ratio of the electrical current density $\vec{j}$ caused by an applied electrical field $\vec{E}$ [15, 61, 64],

$$\vec{j} = \sigma \vec{E} \,. \tag{4.1}$$

A simple approach to model σ is the Drude model [109]. It was formulated in 1900 by P. Drude and describes the electrons as free charge carriers, which are accelerated in the electrical field and decelerated by collisions with the atomic cores, phonons or other particles. The corresponding equation of motion is given by

$$m\frac{\partial \vec{v}_D}{\partial t} = -e\vec{E} - \frac{m}{\tau}\vec{v}_D\,, \tag{4.2}$$

where m is the mass, $\vec{v}_D$ the drift velocity, e the electronic charge, and τ the average time between subsequent collisions. Moreover, the electrical current density is defined as

$$\vec{j} = -e\eta\vec{v}_D\,, \tag{4.3}$$

with η being the density of charge carriers. For the equilibrium, $\frac{\partial \vec{v}_D}{\partial t} = 0$, one finds

$$\vec{j} = \frac{\tau e^2 \eta}{m}\vec{E}\,. \tag{4.4}$$

Comparing this to Eq. (4.1), the conductivity can be written as

$$\sigma = e\eta\mu \tag{4.5}$$

with the charge carrier mobility,

$$\mu = \frac{e\tau}{m}\,. \tag{4.6}$$

Although the Drude model depicts the electrical conductance in a qualitative way, the predicted conductivities are rather weak compared to experimental observations. In 1933, A. Sommerfeld and H. Bethe extended this theory by substituting a Fermi gas for the free electron picture [110]. This led to the same equations as stated above, but with two major modifications. First, only the electrons next to the Fermi energy are considered, and second, the mass m is substituted by an effective mass m^* which is given by the curvature of the bands,

$$m^* = \hbar^2 \left(\frac{\partial^2 \epsilon_{\vec{k}}}{\partial \vec{k}^2} \right)^{-1}\,. \tag{4.7}$$

4.3 MARCUS TRANSFER THEORY

4.3.1 Introduction

For hopping-based transport, the electrical conductivity σ can be qualitatively described in the same way as done in Eq. (4.5). The charge carrier mobility μ, however, originates from other models [108]. Using a simple Einstein diffusion model, it can be expressed via the hopping rate k and the mean hopping distance d:

$$\mu = \frac{ed^2k}{k_BT}\,. \tag{4.8}$$

In order to describe the rates at which an electron jumps from one chemical system to another, R.A. Marcus developed a theory which is nowadays called after him [111–114]. Originally, only electron transfer without large structural changes, so-called outer sphere electron transfer was considered [111–114]. Later it was extended to transfer processes in which geometry changes, so-called inner sphere electron transfer, are involved [115]. This theory is used to describe a number of important processes in chemistry and biology, including photosynthesis, corrosion, certain types of chemiluminescence and charge separation in solar cells. Furthermore, it is widely used to describe CT in organic systems. For his theory, R.A Marcus received the Nobel Prize of chemistry in 1992 [116].

In the following, the general theory and how to apply it to a given system will be described briefly. For a more complete overview, see Ref. 108.

4.3.2 General Theory

Considering a system which consists of two weakly coupled subsystems A and B, a CT from A to B occurs only if the two states $|\mu\rangle$ and $|\nu\rangle$ are degenerated in energy. Here, $|\mu\rangle$ and $|\nu\rangle$ indicate the two states where the considered charge—an electron or a hole—is either present on A or on B, respectively. The transition rate k_{AB} is given by the so-called Fermi's golden rule [117],

$$k_{AB} = \frac{2\pi}{\hbar} \int f(\vec{R}) \left| \langle \mu | \widehat{H}'(\vec{R}) | \nu \rangle \right|^2 \delta(E^\mu(\vec{R}) - E^\nu(\vec{R})) \mathrm{d}^{3N_n} R \, . \tag{4.9}$$

Therein, E^μ and E^ν denote the total energies of the respective states and the function $f(\vec{R})$ refers to a temperature-dependent weight function giving the probability for obtaining a configuration $\vec{R}$.[1] The operator $\widehat{H}'$ describes the weak coupling of the two systems and can be considered as a perturbation to the non-interacting case.

If the system is in the equilibrium, E^μ and E^ν can be approximated by harmonic potentials,

$$E^{\mu/\nu}(\vec{R}) = E^{\mu/\nu}(\vec{R}^{\mu/\nu}) + \sum_\xi \frac{\omega_\xi^2}{2} (R_\xi - R_\xi^{\mu/\nu})^2 \, . \tag{4.10}$$

where ω_ξ^2 are the vibrational frequencies and R_ξ the set of normal coordinates. Note that the same frequencies ω_ξ are used for both cases. In other words, it is assumed that the vibrational modes are independent from the charged states. Furthermore, the canonical distribution is considered for the weight function $f(\vec{R})$,

$$f(\vec{R}) = \frac{1}{Z} \exp \left[-\frac{E(\vec{R})}{k_B T} \right] \quad \text{with} \quad Z = \int \exp \left[-\frac{E(\vec{R})}{k_B T} \right] \mathrm{d}^{3N_n} R \, . \tag{4.11}$$

---

[1] In this notation $\vec{R}$ represents the whole set of the nuclear mass-weighted coordinates $\{\sqrt{m_\alpha}\vec{R}_\alpha\}$.

With this the integral of Eq. (4.9) can be solved.[2] One finds

$$k_{AB} = \frac{|T_{AB}|^2}{\hbar}\sqrt{\frac{\pi}{\lambda k_B T}}\exp\left[-\frac{(\Delta E + \lambda)^2}{4\lambda k_B T}\right] \tag{4.12}$$

with the electronic coupling element,

$$T_{AB} = \langle\mu|\,\widehat{H}'(\vec{R}^*)\,|\nu\rangle\ , \tag{4.13}$$

the reorganization energy,

$$\lambda = \sum_\xi \frac{\omega_\xi^2}{2}(R_\xi^\nu - R_\xi^\mu)^2 = E^\nu(\vec{R}^\mu) - E^\nu(\vec{R}^\nu) \tag{4.14}$$

and the energy difference between the two states $|\mu\rangle$ and $|\nu\rangle$,

$$\Delta E = E^\mu(\vec{R}^\mu) - E^\nu(\vec{R}^\nu)\,. \tag{4.15}$$

The configuration $\vec{R}^*$ refers to the orientation at which the transfer takes place.[3] Figure 4.1 shows a schematic plot of the two energy surfaces E^μ and E^ν along the nuclear coordinate.

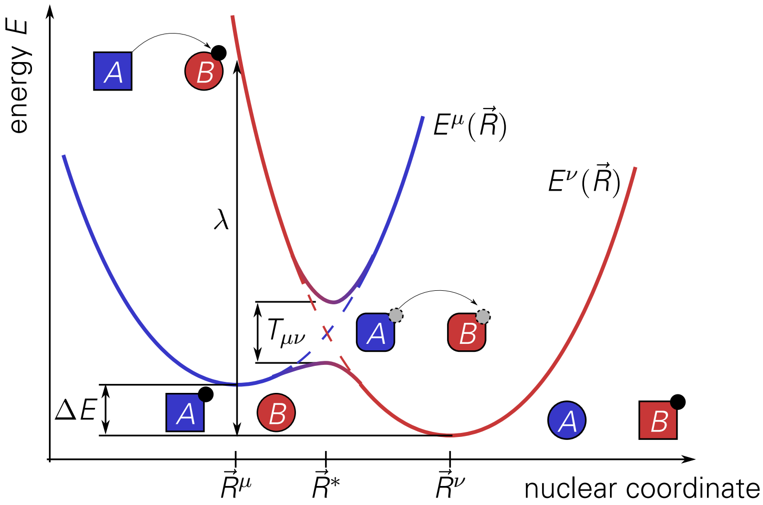

Figure 4.1: Schematic plot of the two energy surfaces for the states $|\mu\rangle$ and $|\nu\rangle$ where the charge is either on A or B, respectively. Squares indicate the geometry of the charged fragments whereas circles represent those of the neutral states. The black dot stands for the charge which is transferred from A to B.

---

[2] For details, see Appendix A.

[3] One should note that $\vec{R}^*$, at which the transfer takes place, can only be defined without further assumption for an one-dimensional coordinate. In general, $\widehat{H}'$ depends on $\vec{R}$ so that the integral of Eq. (4.9) cannot be solved easily. According to the Condon approximation, a constant value can be assigned to T_{AB} which justifies the evaluation of Eq. (4.13) for a single geometry $\vec{R}^*$ [108].

4.3.3 The Fragment Approach

In order to study the CT between two molecules by means of the Marcus theory, the three quantities T_{AB}, λ and ΔE have to be calculated. For this task quantum chemical methods can be used. Their application, however, leads to different challenges according to the applied theory level. While very accurate values can be obtained using *ab initio* calculations [118, 119], their computational cost are rather high so that they are limited to small systems. In order to treat models with a large number of atoms, mainly DFT-based methods have been developed. The most famous ones are the constrained density functional theory [120–122], the frozen-density embedding [123] and the fragment-orbital (FO) approach [124, 125]. The last is the most efficient scheme since it is easy to implement, especially for the evaluation of the coupling element. Because of this it is used in this thesis.

Assuming a weak interaction between the subsystems at which the charge can localize, the main influencing factors on the CT intuitively arise from the two sites A and B which are involved in the CT. Hence, it is efficient to consider A and B as isolated fragments [124, 125]. One should note, however, that neglecting the interactions between the fragments in the calculation of the energy, the structure and the FOs is of course a strong simplification and not feasible for all systems. For instance, the geometry of organic molecules might be different in crystals compared to the gas phase. It has been shown, however, that this approach works remarkably well for many applications in the field of OE [124, 126–128].

4.3.4 The Reorganization Energy

While deriving the Marcus formula, the reorganization energy λ was introduced, which simply indicates the energy needed to perform the CT without relaxation of the geometry. In this way, a large reorganization energy implies a strong geometry difference between the two states and thus a more unlikely CT.

Using the fragment approach, the individual contributions to λ can be obtained by relaxing the geometry of the individual fragments in the neutral and ionic states. The cationic case has to be studied for hole transport, whereas the anionic case is relevant to consider electron transfer.

Within the fragment approach the energy of the composed system, is given by the sum of the energies of the two subsystems

$$E^{\mu} = E_{\mathrm{c}}^{A} + E_{\mathrm{n}}^{B} \quad \text{and} \quad E^{\nu} = E_{\mathrm{n}}^{A} + E_{\mathrm{c}}^{B}, \tag{4.16}$$

where the indices n and c refer to the neutral and charged state of the fragments, respectively. Similarly, the geometry $\vec{R}$ is given as the superposition of the corresponding fragment configurations $\vec{R}^{A}$ and $\vec{R}^{B}$. Thus, the two equilibrium geometries $\vec{R}^{\mu}$ and $\vec{R}^{\nu}$ are given as

$$\vec{R}^{\mu} = \left(\vec{R}_c^A, \vec{R}_n^B\right) \text{ and } \vec{R}^{\nu} = \left(\vec{R}_n^A, \vec{R}_c^B\right) . \tag{4.17}$$

Hence, the reorganization energy can be calculated by

$$\lambda = \left[E_c^A(\vec{R}_n^A) - E_c^A(\vec{R}_c^A)\right] + \left[E_n^B(\vec{R}_c^B) - E_n^B(\vec{R}_n^B)\right] = \lambda_c^A + \lambda_n^B . \tag{4.18}$$

Note that λ consists of two terms: λ_c^A denotes the energy for bringing A from the charged to the neutral equilibrium geometry without transfer of the charge, whereas λ_n^B describes the opposite case for fragment B. Since for the CT both processes take place simultaneously, it is intuitive that λ is the sum of these two terms.

It should be noted, however, that when using the fragment approach only the inner reorganization λ_{in}, meaning the contribution of the involved sites, is considered. The outer reorganization λ_{out}, which describes the contributions of the environment, is neglected.

4.3.5 The Electronic Coupling Element

The coupling element T_{AB}, also known as diabatic coupling or transfer integral, contains most of the microscopic information. It is considered in various transport models from small polaron hopping [124, 129–131], coherent band [132, 133] and polaronic band transport [134]. T_{AB} is defined as the integral over $|\mu\rangle$ and $|\nu\rangle$ where $\hat{H}'$ is acting on one of them, see Eq. (4.13).

Within the fragment approach, the two many-body wave functions $|\mu\rangle$ and $|\nu\rangle$ can be constructed by the orbitals of the isolated fragments using a Slater determinant ansatz:[4]

$$|\mu\rangle = \frac{1}{\sqrt{N_A + N_B + 1}} \mathrm{SLT}\left(\left|\phi_1^{(\alpha)}\right\rangle, \ldots, \left|\phi_{N_A}^{(\alpha)}\right\rangle, \left|\phi_{N_A+1}^{(\alpha)}\right\rangle, \left|\phi_1^{(\beta)}\right\rangle, \ldots, \left|\phi_{N_B}^{(\beta)}\right\rangle\right) \tag{4.19}$$

and

$$|\nu\rangle = \frac{1}{\sqrt{N_A + N_B + 1}} \mathrm{SLT}\left(\left|\theta_1^{(\alpha)}\right\rangle, \ldots, \left|\theta_{N_A}^{(\alpha)}\right\rangle, \left|\theta_1^{(\beta)}\right\rangle, \ldots, \left|\theta_{N_B}^{(\beta)}\right\rangle, \left|\theta_{N_B+1}^{(\beta)}\right\rangle\right) . \tag{4.20}$$

Therein, $\phi_i^{(\alpha)}$ are the FOs of fragment A and $\phi_i^{(\beta)}$ the ones of B when the additional electron is on site A. Accordingly, when the charge is localized on site B, the FOs of A and B are denoted as $\theta_i^{(\alpha/\beta)}$. The numbers of electrons of the uncharged fragments A and B are referred to as N_A and N_B, respectively.

Replacing the exact perturbation Hamiltonian $\widehat{H}'$ with a sum of KS one-electron Hamiltonians,

$$\widehat{H}' = \sum_i \hat{h}_i , \tag{4.21}$$

Eq. (4.13) becomes a sum over products of integrals. According to the Slater-Condon rules [135, 136] these integrals are given by

---

[4] Here, only the case for an additional electron is presented. For hole transport the Slater determinant has to be formulated with the corresponding $N_A + N_B - 1$ FOs.

$$\left\langle \phi_i^{(\alpha)} | \theta_j^{(\alpha)} \right\rangle \approx \delta_{ij} \tag{4.22}$$

$$\left\langle \phi_i^{(\alpha)} | \theta_j^{(\beta)} \right\rangle \approx 0 \tag{4.23}$$

$$\left\langle \phi_i^{(\alpha)} \middle| \hat{h} \middle| \theta_j^{(\alpha)} \right\rangle = \zeta_{ij} \tag{4.24}$$

$$\left\langle \phi_i^{(\alpha)} \middle| \hat{h} \middle| \theta_j^{(\beta)} \right\rangle = \tau_{ij} \,. \tag{4.25}$$

More specifically, each summand consists of a product of $N_A + N_B$ integrals of Eq. (4.22) or Eq. (4.23) and one of Eq. (4.24) or Eq. (4.25). Thus, a non-vanishing contribution is only obtained if all factors Eq. (4.22) yield 1. This leads to a simplified representation of T_{AB}. In particular, the electronic coupling element for electron transfer is given by

$$T_{AB}^{e} = \left\langle \phi_{N_A+1}^{(\alpha)} \middle| \hat{h} \middle| \theta_{N_B+1}^{(\beta)} \right\rangle = \left\langle \phi_{\mathrm{LUMO}}^{(\alpha)} \middle| \hat{h} \middle| \theta_{\mathrm{LUMO}}^{(\beta)} \right\rangle \tag{4.26}$$

and for hole transfer by

$$T_{AB}^{h} = \left\langle \phi_{N_A}^{(\alpha)} \middle| \hat{h} \middle| \theta_{N_B}^{(\beta)} \right\rangle = \left\langle \phi_{\mathrm{HOMO}}^{(\alpha)} \middle| \hat{h} \middle| \theta_{\mathrm{HOMO}}^{(\beta)} \right\rangle \,. \tag{4.27}$$

One should note, however, that Eq. (4.23) assumes an orthogonality of the FOs of different fragments. This approximation is automatically fulfilled, when the FOs are represented in an orthogonal basis set. Alternatively, the values obtained from a non-orthogonal basis can be corrected via a Löwdin-like transformation [137]:

$$\tilde{T}_{AB} = T_{AB} - S_{AB} \frac{\epsilon_A + \epsilon_B}{2} \,. \tag{4.28}$$

In this equation, $S_{AB} = \left\langle \phi^{(\alpha)} | \theta^{(\beta)} \right\rangle$ is the overlap of the corresponding FOs and ϵ_A and ϵ_B are the associated on-site energies.

To calculate T_{AB} by means of Eq. (4.26) and Eq. (4.27), $\left|\phi^{(\alpha)}\right\rangle$, $\left|\theta^{(\beta)}\right\rangle$ and $\hat{h}$ are needed. As derived so far, they have to be evaluated for the transition geometry $\vec{R}^{*}$, which defines the the geometries of the subsystems, but also their relative orientation. When using DFT-based methods, $\left|\phi^{(\alpha)}\right\rangle$, $\left|\theta^{(\beta)}\right\rangle$ and $\hat{h}$ furthermore depend on the charge density ρ which has to be constructed in line with the assumptions made so far. The transition geometry $\vec{R}^{*}$, however, is unknown and the formally exact transition density is hard to access. Hence, further assumptions are required, which are summarized in Tab. 4.1. Within the fragment approach the neutral and the charged fragment geometries $\vec{R}_{\mathrm{n}}^{A/B}$ and $\vec{R}_{\mathrm{c}}^{A/B}$ are available, so that it is straightforward to use them. Moreover, for a system with a large number of electrons, the local changes of the density is small when N_A or N_B are varied. For simplicity it is therefore sufficient to consider the densities of the neutral cases being in line with the frozen orbital approximation. Thus, Eq. (4.26) and Eq. (4.27) can be calculated by using the HOMO and LUMO wave functions of the neutral fragments. In a fully rigorous way, $\hat{h}$ should be derived from the superposition of the fragment densities.

Table 4.1: Overview of further approximations for the geometry the elecronic density.

	geometry		electronic density	
quantity	exact	approximation	exact	approximation
$\left\|\phi^{(\alpha)}\right\rangle$	$\vec{R}_A^*$	$\vec{R}_A^{\mathrm{n}}$	$\rho_A(N_A \pm 1)$	$\rho_A(N_A)$
$\left\|\theta^{(\beta)}\right\rangle$	$\vec{R}_B^*$	$\vec{R}_B^{\mathrm{n}}$	$\rho_B(N_B \pm 1)$	$\rho_B(N_B)$
$\hat{h}$	$\vec{R}^*$	$\left(\vec{R}_A^{\mathrm{n}}, \vec{R}_B^{\mathrm{n}}\right)$	$\rho_A(N_A \pm 1) + \rho_B(N_B)$	$\rho_{A+B}(N_A + N_B)$

In practice, however, it is preferred to use the self-consistent density of the composed system which is easily available from common software packages. A critical study on the effect of different densities has been discussed in literature, where only minor corrections to these simplifications were found[138]. It can therefore be concluded that it is sufficient to calculate the coupling element in the here presented way.

In conclusion, the Marcus transfer theory together with the fragment approach offer the possibility to calculate the adiabatic CT rates, at which an electron hops from one localization center to another, by means of the DFT methods described in Chapter 3.

Part III

Results

5 GEOMETRY AND ELECTRONIC STRUCTURE OF MONOMER AND OLIGOMER MODELS

5.1 INTRODUCTION

In the past decades, organic materials with semiconducting properties were intensively studied by experiments and simulations [1, 139, 140]. For the first and second generation of conductive polymers many articles on different aspects were published. Due to their recent discovery, however, detailed studies on donor-acceptor (DA) polymers are still missing in the standard literature. Especially the impact of different orientations of the polymer backbone is poorly investigated for this kind of polymer class. Only very recently, the aspects of different conformations in P(TDPP-TT) have partially been addressed and reported [141].

To investigate a molecular system on the atomic scale, the specific conformation, i.e. the position of all atoms, is an important issue. For soft materials such as polymers or proteins, the orientations of individual units can be experimentally accessed, for instance via X-ray scattering, such as grazing-incidence wide angle X-ray scattering (GIWAXS) or near-edge X-ray absorption fine structure (NEXAFS) spectroscopy, or via magic-angle spin nuclear magnetic resonance (MAG NMR) spectroscopy [141]. Nevertheless, it is very challenging to precisely characterize the atomic-level backbone conformations in experiment. Simulating the materials using *ab initio*, *first principles* or empirical methods is therefore an efficient alternative to study the interactions determining the geometry and consequently to predict the most probable orientations.

To describe an electronic transfer process on a quantum theory level, knowledge of the electronic structure, i.e. the wave functions and their eigenenergies, is needed. On the one hand, the position of energetic levels, especially those of the highest occupied molecular orbital (HOMO) and lowest unoccupied molecular orbital (LUMO), are of interest. In organic semiconductors, these levels act like the valence and conduction band of bulk semiconductors. Hence, the HOMO-LUMO-gap indicates the conductivity of intrinsic semiconductors. On the other hand, the quantum mechanical wave functions are required in order to describe charge transfer processes. The spatial shape of the orbitals, the positions of nodal surfaces, and the localization lengths are important issues which influence the characteristics of the electronic transport.

While *ab initio* calculations require large computational resources and are therefore limited to systems with a small number of atoms, empirical force-field methods do not yield the electronic structure at all. Thus, *first principles* are the adequate compromise to study polymer materials.

This chapter is devoted to a detailed investigation of different orientations and the dependence of the corresponding total energies on internal degrees of freedom. For this, small models were studied motivated by the building blocks of the DA polymers considered in this thesis. By comparing the energies of different conformations, their stabilities and impacts on structurally induced effects are investigated. Here, the focus is on the dihedral angles between successive units, since the planarity is of crucial importance to achieve high electrical conductivity. The insights gained from these investigations can help to design new molecular structures with the geometrical aspects favoring desired physical properties. Moreover, this chapter also aims at considering the electronic structure and comparing different levels of theory to justify the adequacy for the further use in this thesis. Based on these results, first conclusions on the impact of the modeling and of the structural approximations are drawn. These studies are important not only to benchmark the used methods against already reported studies, but also to complete the missing information in the available literature.

5.2 COMPUTATIONAL DETAILS

To make use of the specific advantages of the different implementations of density functional theory (DFT) based methods, several software packages were used in this part of the thesis. Geometry optimizations with VWN [72], PBE [78] and B3LYP [77, 142] functionals were performed using the software SCM ADF 1.3 [123, 143, 144]. Calculations with the VWN and PBE functionals were cross-checked by deMon [145] and GAMESS [146]. In all cases, DZP basis sets were used. Moreover, density functional based tight binding (DFTB) calculations were performed using the DFTB+ software package [147] and the mio-1-1 parameters [87, 91]. They were obtained using the PBE functional to derive the on-site energies and the AOs of the free atoms as well as the two center integrals. The repulsive potentials were fitted against B3LYP calculations. For all calculations, the self-consistent charge schema was used.

Optimizations with fixed dihedral angles were performed using deMon. Only for calculations with the B3LYP functional the GAMESS software package was used, since hybrid functionals are not available in deMon.

For the calculations of π-π stacked 2,2′:5′,2″-terthieno[3,2-b]thiophene (3TT) models the Grimme dispersion correction was employed. For thiophene based systems, a good agreement of this approach compared with second-order Møller-Plesset perturbation theory (MP2) calculations was reported [148, 149].

5.3 STRUCTURAL ASPECTS

5.3.1 Monomer Model of TDPP

Due to their aromatic nature, both thiophene and diketopyrrolo[3,4-c]pyrrole (DPP) have planar structures. Assuming a fully planar structure also for TDPP, two configurations have to be considered, see Fig. 5.1. Referring to the position of the sulfur and the nitrogen atoms, these structures are called *trans*, Fig. 5.1a), and *cis*, Fig. 5.1b), configurations, respectively. The tables 5.1 and 5.2 summarize the bond lengths and angles as obtained from calculations with the different simulation methods.

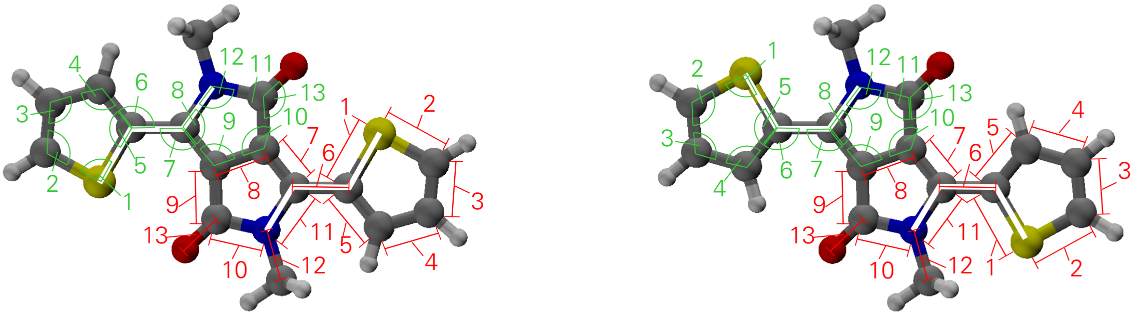

a) *trans*-configuration b) *cis*-configuration

Figure 5.1: Labeling of the bond lengths (red) and bond angles (green) in *trans* (a) and *cis* (b) orientations.

All considered methods yield similar results with variations in bond lengths and angles which are smaller than 2%. Overall, the PBE and B3LYP results show slightly larger distances than the ones obtained with VWN. The strongest deviation occurs for C-N bonds (d10, d11 and d12) of the DPP unit. The distances obtained from the DFTB calculation are in general larger than the VWN values and therefore closer to the results of PBE and B3LYP. Comparing the *cis* and *trans* results shows that the interaction of next nearest atoms is independent from the particular isomer, since all distances remain very similar when the thiophene rings are turned. The bond angles also show similar values for all different computational methods and for the two considered configurations. Here, *trans* and *cis* differ most in a6 and a7, which describe the orientation of the thiophene rings within the plane. The planarity of the individual units can easily be seen by the interior angle sums of the thiophene and DPP pentagons, which yield about 540° in all the cases.

Table 5.1: Bond lengths of TDPP monomer models in *cis* and *trans* configurations as obtained from DFT using different functionals and DFTB. The labeling is according to Fig. 5.1.

		trans				cis			
		VWN	PBE	B3LYP	DFTB	VWN	PBE	B3LYP	DFTB
d1	C-S	1.73 Å	1.75 Å	1.75 Å	1.74 Å	1.73 Å	1.75 Å	1.75 Å	1.73 Å
d2	S-C	1.69 Å	1.71 Å	1.71 Å	1.70 Å	1.69 Å	1.71 Å	1.71 Å	1.70 Å
d3	C-C	1.37 Å	1.37 Å	1.36 Å	1.39 Å	1.37 Å	1.37 Å	1.36 Å	1.39 Å
d4	C-C	1.39 Å	1.41 Å	1.40 Å	1.41 Å	1.39 Å	1.40 Å	1.40 Å	1.41 Å
d5	C-C	1.38 Å	1.39 Å	1.38 Å	1.40 Å	1.38 Å	1.39 Å	1.38 Å	1.40 Å
d6	C-C	1.41 Å	1.43 Å	1.43 Å	1.43 Å	1.41 Å	1.43 Å	1.43 Å	1.44 Å
d7	C-C	1.38 Å	1.39 Å	1.38 Å	1.40 Å	1.38 Å	1.40 Å	1.38 Å	1.40 Å
d8	C-C	1.40 Å	1.42 Å	1.41 Å	1.42 Å	1.40 Å	1.42 Å	1.42 Å	1.43 Å
d9	C-C	1.42 Å	1.44 Å	1.44 Å	1.44 Å	1.42 Å	1.44 Å	1.44 Å	1.46 Å
d10	C-N	1.43 Å	1.45 Å	1.45 Å	1.42 Å	1.42 Å	1.44 Å	1.43 Å	1.42 Å
d11	N-C	1.37 Å	1.39 Å	1.39 Å	1.39 Å	1.36 Å	1.38 Å	1.38 Å	1.38 Å
d12	N-C	1.42 Å	1.44 Å	1.45 Å	1.43 Å	1.42 Å	1.44 Å	1.45 Å	1.43 Å
d13	C-O	1.22 Å	1.23 Å	1.21 Å	1.24 Å	1.22 Å	1.23 Å	1.22 Å	1.23 Å

Table 5.2: Bond angles of TDPP monomer models in *cis* and *trans* configurations as obtained from DFT using different functionals and DFTB. The labeling is according to Fig. 5.1.

		trans				cis			
		VWN	PBE	B3LYP	DFTB	VWN	PBE	B3LYP	DFTB
a1	CSC	91.4°	91.4°	91.3°	92.1°	91.7°	91.6°	91.5°	93.1°
a2	SCC	112.9°	112.8°	112.7°	112.1°	112.2°	112.2°	112.3°	111.2°
a3	CCC	112.2°	112.4°	112.3°	112.7°	112.8°	112.9°	112.8°	113.0°
a4	CCC	112.0°	113.3°	113.3°	112.5°	112.6°	113.1°	113.3°	112.7°
a5	CCS	110.4°	110.2°	110.3°	110.6°	110.7°	110.1°	110.0°	110.0°
a6	CCC	129.5°	129.7°	130.4°	130.1°	123.9°	124.4°	124.3°	123.1°
a7	CCC	128.4°	128.6°	128.7°	129.7°	126.4°	126.7°	127.1°	126.3°
a8	CCN	106.8°	106.9°	107.1°	107.0°	107.1°	106.9°	107.0°	107.6°
a9	CCC	109.1°	109.2°	109.3°	109.3°	108.7°	109.0°	109.2°	108.8°
a10	CCC	108.7°	108.9°	108.5°	107.6°	108.8°	109.0°	108.5°	107.4°
a11	CCN	103.6°	103.3°	103.5°	105.1°	103.8°	103.3°	103.6°	104.7°
a12	CNC	111.7°	111.6°	111.5°	111.1°	111.7°	111.7°	111.7°	111.7°
a13	CCO	133.8°	133.9°	133.3°	129.8°	133.2°	134.4°	133.7°	132.4°

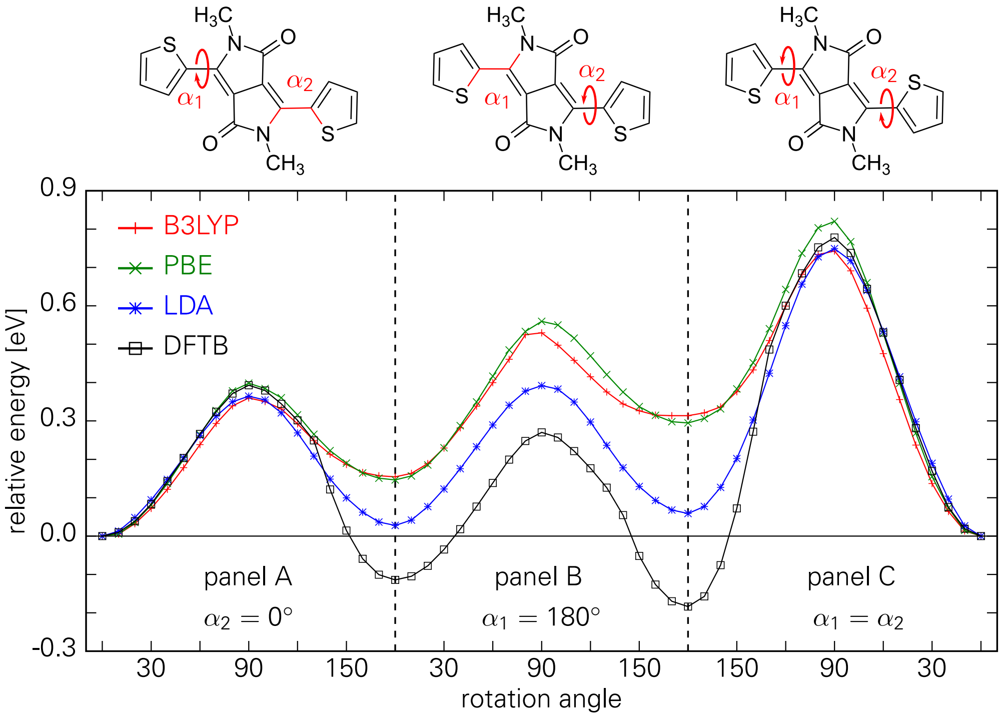

Figure 5.2: Energy landscape for turning the thiophene rings in TDPP monomers. In the first panel only one thiophene is rotated by α_1 from *cis* to *trans* configuration, whereas $\alpha_2 = 0°$ is fixed. Second, the other thiophene unit is turned by α_2 and $\alpha_1 = 180°$ is constant. Finally, both units are rotated simultaneously from *trans* to *cis*.

For a long range conjugation within a polymer, the dihedral angles of successive units are responsible for the planarity of the backbone. As such, the consideration of twisted structures is of particular importance to predict the stability of π-π stacks. Hence, this property was studied in more detail. To do so, the energy which is needed to rotate the thiophene rings was calculated. The obtained results are shown in Fig. 5.2 which contains three panels: Starting from the configuration where both thiophene rings are in *cis* configuration, in panel A the left thiophene is rotated by α_1 around the axis of the corresponding bond to the DPP unit. The orientation of the right thiophene is fixed to $\alpha_2 = 0°$. For each of these configurations, the geometry was optimized keeping α_1 and α_2 constant. After reaching the planar-*trans* configuration, the right thiophene is rotated in the same way while $\alpha_1 = 180°$ is fixed, see panel B. In panel C, both units are simultaneously turned back to the *cis* configuration.

The following conclusions can be drawn from Fig. 5.2: First, the curves of panel A and panel B differ by constant off-sets, which means that the two thiophenes can be rotated independent from each other. Second, all planar configurations occur as local minima separated by barriers of roughly 0.4 eV. This leads to the conclusion that TDPP units are planar and thermal fluctuations are not able to invert the thiophenes. Third, for $\alpha < 120°$, all methods are in good agreement, but for larger angles different behaviors are observed. For $\alpha > 120°$, only the PBE and B3LYP results remain similar. In both cases, the energy of the *trans* configuration is about 0.18 eV higher than the one with $\alpha = 180°$. This preference of the *cis* configuration can be explained by the interaction of thiophene hydrogen atoms and the carbonyl groups of DPP which might form a hydrogen bond. This interaction seems to be underestimated by the LDA approach. The VWN functional yields the *trans* configuration only by about 0.03 eV higher in energy than the *cis* configuration. When DFTB is used, the *trans* configuration is even by about 0.1 eV more stable. It can be assumed that the non-bonded interaction between the sulfur and the oxygen atoms is not descried well enough by the mio-1-1 parameter set.

The energetic sequence of the TDPP configurations obtained with PBE and B3LYP functionals agree with that recently published by Chaudhari *et al.* [141]. In their work, however, planarity was found for the *cis* conformation only. For thiophenes in *trans* configuration, dihedral angles of 22° were reported for the optimized configuration. It should be remarked, however, that the results reported in Ref. 141 are not fully consistent. The authors also show an energy curve for a DPP-T-TT model, in which local minima can be seen for planar orientations only. One can speculate that the deviations from the fully planar configuration represent local minima, because of insufficient convergence criteria in the geometry optimization. Thus, it can be concluded that a systematic consideration of the rotation angles seems to be important to find the optimal orientation.

5.3.2 Thiophene Compounds

The donor units of DA polymers are often based on thiophene derived compounds due to their electron richness. To this end, connections between two thiophene units are typically formed. In this section, the planarity of such a connection is studied by means of different DFT approaches. In order to do so, 2,2'-bithiophene (2T) and 2,2'-bithieno[3,2-b]thiophene (2TT) models are considered, see Fig. 5.3. For both, several geometries were optimized keeping the torsion angle φ constant in order to estimate the

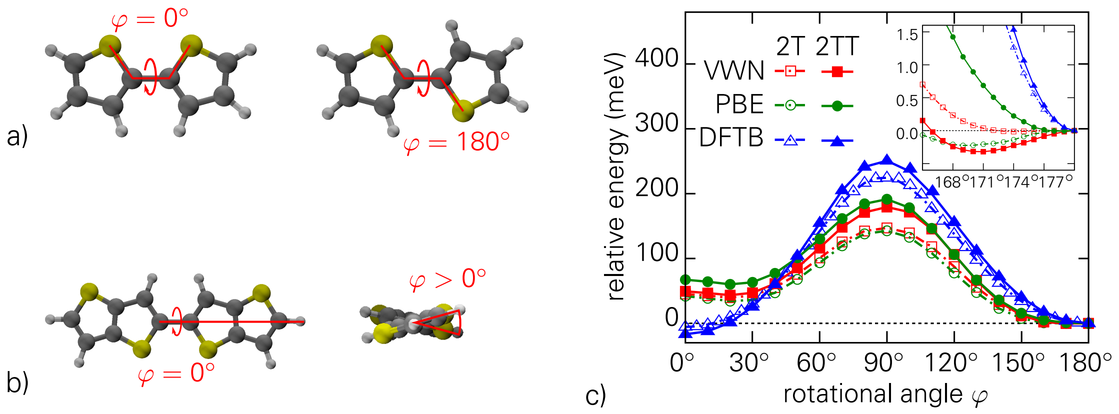

Figure 5.3: a) 2T in *cis* (left) and *trans* (right) configurations and b) Top (left)and side (right) view of 2TT model in *cis* orientation. c) Energy landscape for rotating the units from the *cis* (0°) to the *trans* (180°) configuration obtained using DFT with VWN and PBE functionals and DFTB.

equilibrium geometries and the energy barriers between them.

Here and later on, the following notation is used: Referring to the positioning of the sulfur atoms, orientations with $0° \leq \varphi < 90°$ are referred to as *cis* configuration, whereas for $90° < \varphi \leq 180°$ the corresponding geometries are called *trans* configurations. For both, two special cases are considered. On the one hand, the fully planar structures, $\varphi = 0°$ and $\varphi = 180°$, are called planar-*cis* and planar-*trans* configurations. The corresponding energies are indicated by E_{cis}^{planar} and $E_{trans}^{\text{planar}}$, respectively. On the other hand, the configurations for which local minima are found are referred to as optimal-*cis* and optimal-*trans* with the energies E_{cis}^{opt} and E_{trans}^{opt}. Finally, the orientations with $\varphi = 90°$ and their energies are denoted as perpendicular configuration and E_p.

The dependences of the energy on the interlinkage dihedral angle φ and on the used computational methods are given in Fig. 5.3 c) and Tab. 5.3. For the 2T model, the calculated DFT curves exhibit two local energy minima with non-planar structures, whereas the planar and the perpendicular orientations appear as saddle points. The optimized dihedral angles obtained with the VWN and PBE functionals are 28° and 26° in the *cis* and 174° and 169° in *trans* conformations. For the 2TT model, only the perpendicular and the planar-*cis* structure yield saddle points for both VWN and PBE. The planar-*trans* configuration yields a minimum for calculations with PBE whereas it is a further saddle point for those with VWN. Instead, the graph obtained using the VWN functional suggests an optimum for a rotation of about 171°. The DFTB calculations yield two local minima at 0° and 180° and one saddle point for the perpendicular orientation for both 2T and 2TT.

So far, the energy curves which were found by the different methods were described.

Table 5.3: Stability of the planar and the optimal-*cis* as well as of the optimal-*trans* conformations compared to the planar-*trans* isomers for 2T and 2TT models. Optimized dihedral angles are given in brackets.

	relative energy (meV)			
	planar-*cis*	optimal-*cis*	perpendicular	optimal-*trans*
	$E_{cis}^{\text{planar}} - E_{trans}^{\text{planar}}$	$E_{cis}^{\text{opt}} - E_{trans}^{\text{planar}}$	$E_p - E_{trans}^{\text{planar}}$	$E_{trans}^{\text{opt}} - E_{trans}^{\text{planar}}$
2T				
DFTB	-5.6 (0°)		224.4	0.0 (180°)
VWN	44.5	39.3 (28°)	146.0	> -0.1 (174°)
PBE	41.9	34.2 (26°)	142.7	-0.2 (169°)
B3LYP [150]	38.5	23.8 (30°)	110.7	-0.6 (159°)
MP2 [150]	38.6	-1.1 (43°)	54.5	-22.7 (146°)
2TT				
DFTB	-16.9 (0°)		250.6	0.0 (180°)
VWN	49.0	43.1 (27°)	177.9	-0.3 (171°)
PBE	67.2	60.2 (24°)	191.3	0.0 (180°)

Now, the results for the 2T and the 2TT models are compared and interpreted: First, the saddle point at 0° is considered. The differences between E_{cis}^{planar} and E_{cis}^{opt} are the same for both 2T and 2TT. This can be explained by the repulsion of the hydrogen atoms whose interaction is the same in both cases. Since this saddle point is not found by DFTB using the mio-1-1 parameters, it is assumed that the non-bonded interaction between the hydrogen is underestimated there. Second, the energy of the perpendicular orientation is discussed. Here, all methods suggest a smaller barrier for 2T than for 2TT. This can be explained by the enhanced π-system of 2TT which favors the planar structures. Third, the behaviors of the energy curves are examined for $\varphi \approx 180°$. The local minimum which PBE suggests for 2TT can also be explained by the enhanced π-system. Surprisingly, the results obtained from the VWN calculations show the opposite behavior: Here, a larger equilibrium dihedral angle is observed for the 2TT than the 2T model. Finally, the results of 2T are compared to values found in the literature [151] where higher levels of theory were used, see Tab. 5.3. One can see, that the energy barriers at 0° and 180° are underestimated by all DFT methods, whereas the one of perpendicular orientation is overestimated. This due to the well-known Kohn-Sham delocalization which leads to an overstabilisation of planar orientations.

It should be noted, that the obtained values describe the molecules in gas phase at 0 K. Indeed, comparing to electron diffraction experiments of 2T in gas phase shows that non-planar structures can be observed experimentally [150]. In molecular crystals, however, weak interactions with neighboring molecules such as π-π interactions compensate the hydrogen repulsion such that planar structures are observed [152]. Moreover, the barriers found for 0° and 180° are small compared to room-temperature. Hence, thermal fluctuations might allow a flipping between the non-planar conformations such that planar models are sufficient to describe the structure.

5.3.3 Oligomer Models of Thieno[3,2-b]thiophene

As molecular models, 2T and 2TT favor non-planar conformations. To answer the question to what extent this remains true for polymers and polymer films with 2T or 2TT units, extended oligomer models are considered. Varying a single interlinkage dihedral angle of a oligothiophene model leads to long-range changes in the backbone. Since for TT models the carbon atoms which connect adjacent units are on one axis, see Fig. 5.3 b), a single unit can be turned without affecting long-range arrangements. For this reason, oligomer models of TT (oTT) up to nine repeat units are considered in this section. In particular, the focus is on the optimal-*cis* configuration and the hight of the barrier at $\varphi = 0°$.

At first, the geometries were optimized by means of DFT using the PBE functional, where all dihedral angles between successive were fixed to the same value of φ. In order to analyze, to what extent successive dihedral angles affect each other, three versions of non-planar configurations were considered: In version A, only the central unit is rotated by φ while all others are fixed to planar-*trans* configuration. In version B and C, all units are rotated by φ relative to the adjacent ones. While in B all rotations are performed in the

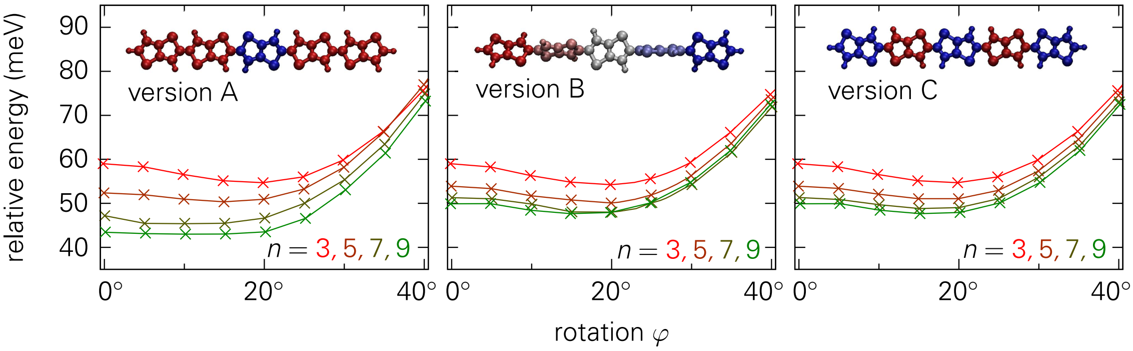

Figure 5.4: Energy per twisted bond relative to the planar-*trans* configuration for different oligomer lengths n when rotating the central unit only (version A, left), twisting the chain (version B, center) or performing rotation in alternating directions (version C, right).

same direction such that a twisted chain is described, in version C the case of alternating torsions is considered.

As already found for 2TT, the configurations with $\varphi = 180°$ yield the lowest energies for all oTT models and hence define the global minima. The relative energies for the *cis* configurations with $\varphi < 40°$ are depicted in Fig. 5.4. It can be seen, that for version A the barrier at 0° vanishes for larger chains. In particular, the model with nine repeat units shows an almost constant energy for $\varphi < 20°$. For the versions B and C, however, the barrier at $\varphi = 0°$ remains, but it decreases with increasing model size. Moreover, B and C show same behaviors for all chain lengths so that one can conclude that the orientations of successive dihedral angles do not affect each other.

When the oTT models are optimized without fixing the dihedral angle, the mutual alignment of successive units change slightly with approaching the terminating units. Table 5.4 summarizes values of φ_i for different oligomer lengths; for the labeling see Fig. 5.5. Moreover, the energies for the planar-*cis* and the optimal-*cis* configurations are given relative to $E_{trans}^{\text{planar}}$. Using this values the barrier height at per twisted bond $\varphi = 0°$ can be deduced using the following expression:

$$\Delta E_{\text{barrier}} = \frac{E_{cis}^{\text{planar}} - E_{cis}^{\text{opt}}}{n - 1} \,. \tag{5.1}$$

One can see that with increasing oligomer length n, the inner angles, φ_0 and φ_1, tend to a more planar configuration. However, this trend seems to converge at about 16.5°. The outmost angles, on the other hand, decrease only slightly compared to the 2TT model and saturate at about 20.5°. The barrier at 0° decreases with increasing oligomer length but saturates at about 2.4 meV. From these results, the following conclusions can be drawn: The extension of the π-system may favor a planar configuration, but this does not compensate the repulsion between the hydrogen atoms. It should be remarked, however, that the obtained barriers are small compared to room temperature so that packing effects can be assumed to stabilize a planar configurations in a film. Under that assumption, a

Table 5.4: Optimal dihedral angles φ_i, energy difference with respect to the planar-*trans* structure and energy barrier $\Delta E_{\mathrm{barrier}}$ per dihedral angle of oTT chains of length n as obtained using the PBE functional. For the numbering of the dihedral angles, see Fig. 5.5. Due to the symmetry of the chains each value, except φ_0, describes two dihedral angles of the oligomer model.

	rotation angle					relative energy (meV)		
n	φ_0	φ_1	φ_2	φ_3	φ_4	$E_{cis}^{\mathrm{planar}} - E_{trans}^{\mathrm{planar}}$	$E_{cis}^{\mathrm{opt}} - E_{trans}^{\mathrm{planar}}$	$\Delta E_{\mathrm{barrier}}$
2	24.2°					67.360.1		7.3
3		21.5°				122.2	112.9	0.45
4	17.9°	21.1°				173.0	161.6	4.7
5		17.7°	20.4°			223.8	210.3	3.9
6	17.0°	17.7°	21.0°			270.4	255.9	3.2
7		16.9°	18.1°	20.2°		319.1	302.5	2.7
8	16.8°	17.4°	17.7°	20.5°		364.7	347.1	2.5
9		16.8°	17.0°	17.6°	20.7°	414.4	394.7	2.4

planar polymer model is sufficient to describe large systems, as shown in the following.

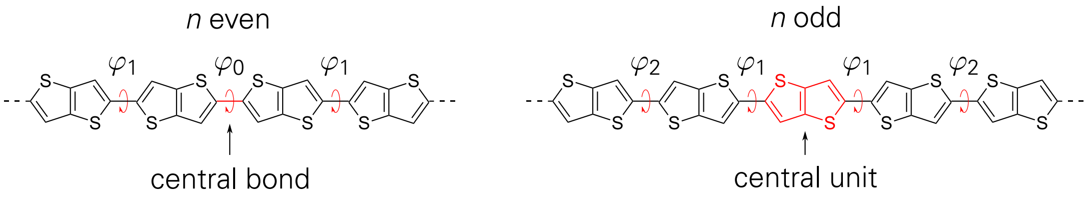

Figure 5.5: Labeling of the dihedral angle for oTT models. In case of an even number of repeat units the central angle is referred to as φ_0 (left), whereas for an odd number, the inner angles are indicated by φ_1 (right).

5.3.4 Interactions in 2,2′:5′,2″-terthieno[3,2-b]thiophene Dimers

Within polymer films, the molecules align to each other. In this case, the interaction of parallel chains can also influence the dihedral angles within the individual chains. To estimate the importance of stacking effects, the impact of the π-π interaction on the planarity was studied in more detail. For this, the stability of the rotational barrier at $\varphi = 0°$ is considered for a dimer of 3TT. Here, only single point PBE calculations were performed using the optimized structures of the isolated 3TT model.

Figure 5.6 depicts the model and the degrees of freedom which were considered to describe the stacking configuration. As before, the dihedral angle φ describes the rotation angle between the subunits. Moreover, the stacking distance z and the shift along the molecule direction x were considered. Note, that the orientation was chosen in such a way that the stacking direction is perpendicular to x and to the bisectrix of φ. In this way, the position of the one molecule on top of the other is assumed to be balanced.

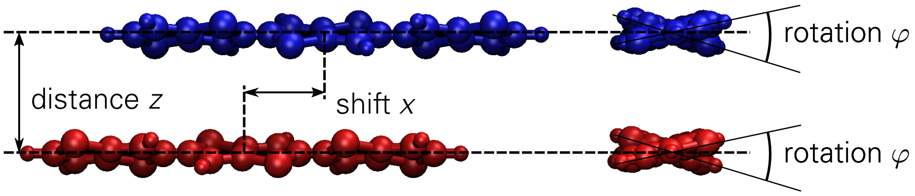

Figure 5.6: Model of π-π stacked 3TT chains. The relative arrangement of the two chains is characterized by the stacking distance z, the shift along the backbone direction x and the dihedral angle φ.

First, the impact of the shift along the oligomer axis for a stacking distance of 3.5 Å is considered for the fully planar-*cis* configurations. Here, two cases are possible: a parallel one, where for $x = 0.0$ Å the sulfur atoms are on top of each other, and an antiparallel one, where they point in opposite directions. The obtained interaction energies are depicted in Fig. 5.7. For both models, the direct stacking ($x = 0.0$ Å) yields a maximum whereas shifts of 1.1 Å and 1.4 Å are found as minima. Note, that for shifts of one unit length (≈6 Å) the stacking orientation changes. Thus, the behavior for $x > 3$ Å for initial parallel stacking equals the antiparallel stacking for $x < 3$ Å. Due to the finite size of the model, however, the total energy increases, since the π-π interaction is reduced for shifted chains; compare full and dashed arrows in Fig. 5.7. Among all minima, the antiparallel stacking with a shift of 1.1 Å is most stable.

Second, the optimal stacking distance for different dihedral angles and different shifts along the backbone is considered. For this, the focus is on the following orientations: (a) the parallel and (b) the antiparallel with x=0.0 Å, (c) the parallel with x =1.1 Å, and (d) antiparallel with a x=1.4 Å. Figure 5.8 illustrates the obtained results. For all cases but (a), the equilibrium distance decreases for small φ. In case (a), however, the $z_{min} = 4.0$ Åstays

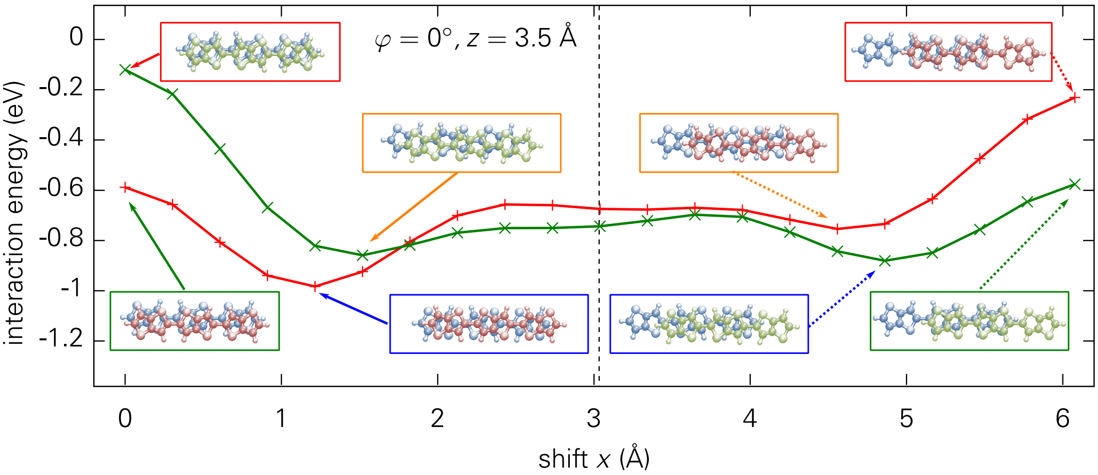

Figure 5.7: Energy landscape when one chain is shifted on top of the other for parallel (green) and antiparallel (red). Both chains are in *cis* configuration and the distance is fixed to $z = 3.5$ Å. The dashed line indicates the shift of half unit length.

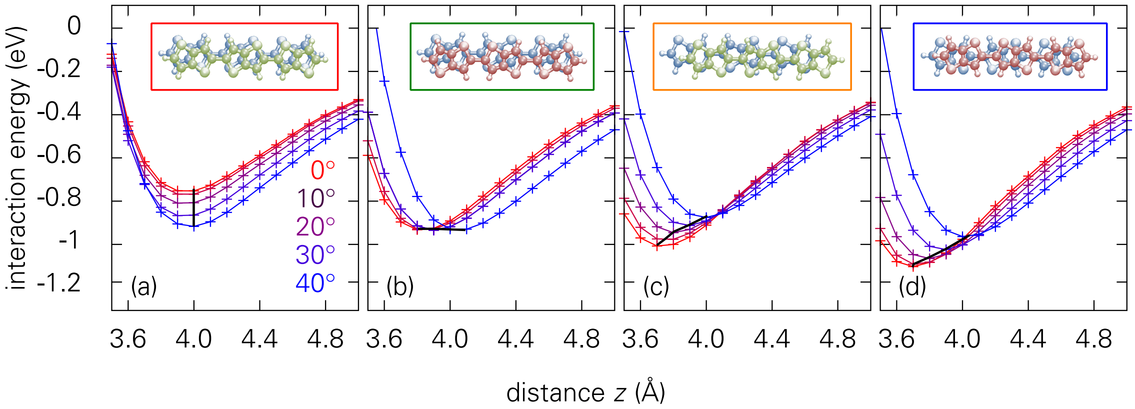

Figure 5.8: Interaction energy of two stacked 3TT chains for different dihedral angles φ in dependence of the stacking distance z for the orientations (a), (b), (c), and (d) as described in the text.

constant, but the energy increases with decreasing φ which is driven by the repulsions of nearest sulfur atoms. Considering case (b), the interaction energy is constant whereas the (c) and (d) clearly show a preference for the planar configuration. Note, that (d) yields the most stable orientation among all considered ones. This indicates, that in such a stack, the π-π interaction of the two chains compensate the repulsion of the hydrogen atoms.

Altogether, the following conclusions can be drawn. Comparing the energy of the rotational barriers, up to 10 meV, to those in π-π stacks, about 200 meV, it can be concluded that the non-planarity of isolated chains can be neglected when semi-crystalline film are modeled. Inter-molecular interactions play a more important role than deviations from the planar configuration.

5.3.5 Analysis of STM Images

As a result from Section 5.3.1, the geometries obtained for the TDPP monomer agreed between the different computational methods used. In all cases, the planar-*cis* and planar-*trans* configurations were found to be local minima. The energy difference between these two conformations, however, varied from -100 meV to 200 meV. Similar observations were made for connected thiophenes, but here the difference between *cis* and *trans* varied from -5 meV to 50 meV only, see Section 5.3.2. In order to get a more profound insight which configurations matter in real systems, scanning tunnel microscopy (STM) images are analyzed in this subsection. The corresponding data was provided by D. Skidin, PhD student under the supervision of F. Moresco and G. Cuniberti. He performed on-surface polymerization[153] of TDPP monomers under ultra-high vacuum at Au(111) surface. The obtained DA polymer strands form monolayers which were recored by STM.[1]

In the obtain images, a limited number of patterns can be found. In particular,

---

[1] For details on the experimental treatment, see related studies such as Refs. 154,155, and 156

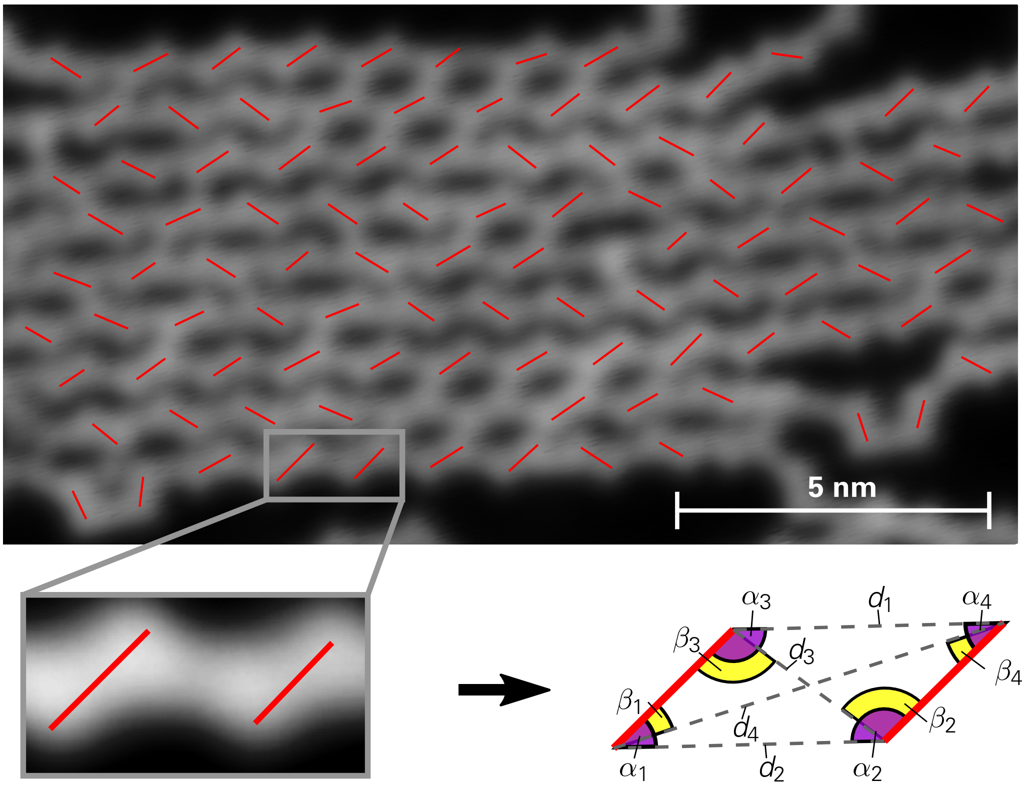

Figure 5.9: Top: STM image of P(DPP-2T) fabricated via on surface polymerization. Brightness, contrast and color schema has been modified. The red lines have been added by hand based to connect the brightest spots of the image. It is assumed that they indicate the DPP positions. Bottom: Schematic plot how the positioning of two adjacent lines are translated into four distances d_i (dashed lines), four wide angles α_i (purple) and for small angles β_i (yellow).

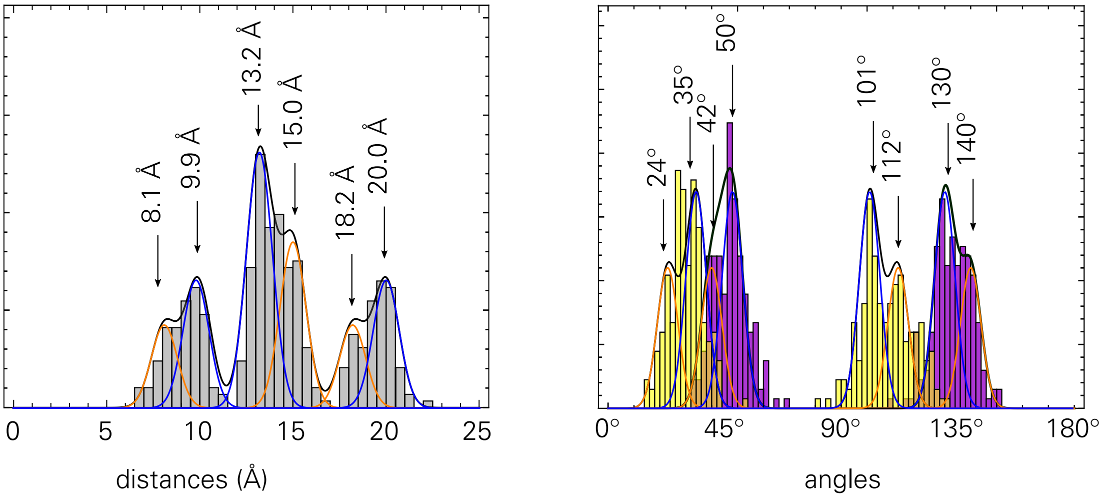

Figure 5.10: Histograms of the distances (left) and angles α (right, purple) and β (right, yellow) obtained from Fig. 5.9. For determining the peak positions, Gauss curves were fitted the histograms.

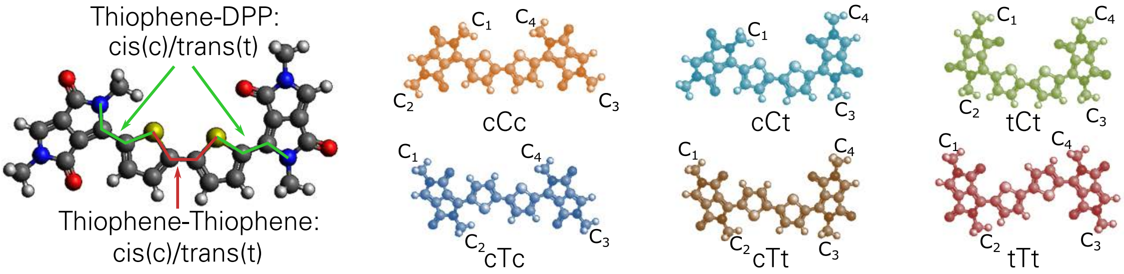

Figure 5.11: Possible configurations for DPP-2T-DPP defining the relative positioning of neighboring DPP units: cCc, cCt, tCt, cTc, cTt and tTt.

Fig. 5.9 shows parallel aligned chains with alternating bright and dark regions. A specific correlation between the bright spots of neighboring chains, however, is not found. By superimposing these bright spots with lines as demonstrated in Fig. 5.9, the patterns can be quantified: Each pair of adjacent lines which belong to the same polymer forms a quadrangle, for which the edge lengths and the interior angles can be determined. In doing so, the relative distances between the bright regions and their orientations can be analyzed statistically.

Figure 5.10 depicts histograms of the distances and angles found in this way. The histogram of the distances, see Fig. 5.10 a), shows three peaks with a 1:2:1 ratio of their areas. Assuming a parallelogram formed by two neighboring lines, this ratio corresponds to that of the short diagonal, the two edges and the long diagonal. On the other hand, the ratio can be explained by a trapezoid; here the short edge, the two diagonals and

Table 5.5: Distances and angles of the optimized structures as obtained from DFTB calculations. For this, the positions of the carbon atoms of the methyl groups were considered. For the numbering of the atoms, see Fig. 5.11.

	cCc	cCt	tCt	cTc	cTt	tTt
$d(C_1, C_4)$	**7.7** Å	8.8 Å	8.4 Å	**12.5** Å	13.9 Å	11.8 Å
$d(C_2, C_3)$	**17.3** Å	14.7 Å	12.2 Å		10.4 Å	
$d(C_1, C_3)$	**13.6** Å	10.9 Å	12.4 Å	**17.5** Å	14.9 Å	15.2 Å
$d(C_2, C_4)$		15.4 Å		**10.8** Å	13.1 Å	12.3 Å
$\alpha(C_1, C_2, C_3)$	**47**°	45°	74°	**120**°	115°	103°
$\alpha(C_4, C_3, C_2)$		82°		**60**°	94°	76°
$\alpha(C_2, C_1, C_4)$	**132**°	148°	105°		94°	
$\alpha(C_3, C_4, C_1)$		85°		**120**°	83°	103°
$\beta(C_1, C_2, C_4)$	**24**°	18°	40°	**85**°	81°	70°
$\beta(C_4, C_3, C_1)$		53°		**40**°	68°	48°
$\beta(C_2, C_1, C_3)$	**108**°	106°	72°		39°	
$\beta(C_3, C_4, C_2)$		71°		**85**°	53°	70°

the long edge yield this behavior. Similarly, the histogram over the angles, Fig. 5.10 b), can be analyses. Here, one can distinguish the angles between two edges (α) and the angles between one edge and one diagonal (β). By fitting Gauss curves to these data, the pattern of the STM image can be translated into numbers. These values can be compared to geometrical properties found by simulation.

By assuming that the lines with which the STM image is superimposed can be refer to the DPP units, the mutual alignment of two neighboring lines is mainly determined by the *cis*-*trans* character of all units in between. Hence, a DPP-2T-DPP model was considered which can adopt six different planar configurations: cCc, cCt, tCt, cTc, cTt and tTt , see Fig. 5.11. In this notation the *cis*-*trans* conformations between DPP and thiophene is indicated by small "c" or "t" and that between two thiophene rings by capital "C" and "T". After optimizing the geometries by means of DFTB, the distances and angles between the carbon centers of the methyl groups were calculated. The obtained results are listed in Tab. 5.5.

Comparing the values obtained from simulation to those detected in the STM images leads to the following conclusions: The cCt and cTt models can be excluded since the straight alignment of the chains cannot be reproduced by these models. Moreover, tTt and tCt would cause much narrower distributions for both distances and angles. The cTc and cCc configurations agree best, since they both suggest a clear partitioning into three peaks for the distribution of the distances. Moreover, they imply large angles with $\alpha > 120°$.

One should also remark, however, that the experimental distributions are not fully reproduced by the optimized geometries. The deviations may arise from the use of the positions of the carbons of the methyl groups to derive the distances and angles from the optimized geometries. Furthermore, interactions between the molecules and the gold may slightly change the geometries. For instance, it has been shown that sulfur atoms exhibit a higher affinity to the gold surface than C or O atoms [157–159]. Therefore, the sulfur atoms atoms may turn towards the substrate and cause slight changed geometries

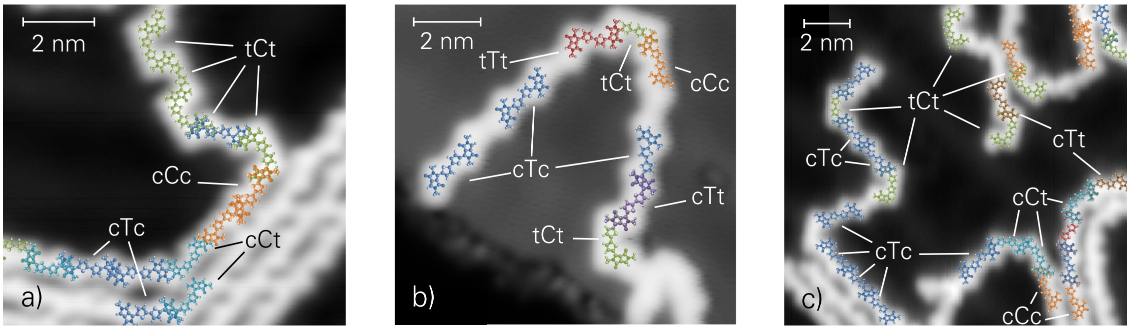

Figure 5.12: STM images of P(DPP-2T) superimposed by DPP-2T-DPP models. Note, that all six configurations were found. Straight aligned polymers are formed by cCc (orange) and cTc (dark blue). The tCt arrangement (green) causes the characteristic zig-zag shape with a minimum periodicity of approximately 2 nm, (a) and (c). The remaining shapes only occur in transition regions which require curved structures.

compared to the planar models obtained with DFTB.

In both cases, cTc and cCc, the DPP and thiophene units arrange in *cis* configuration. This supports the results obtained in Section 5.3.1 by DFT using PBE and B3LYP functionals, for which the *trans* orientation is by 150 meV less stable. It should furthermore be noted, that the remaining orientations cCt, tCt, cTt and tTt can be found in STM images as well. Figure 5.12, shows the relaxed structures of these models superimposed on STM images. It should be emphasized that utilizing the six models considered above the individual shapes of the STM images can be reproduced with high accuracy. Hence, it can be concluded that all configurations with respect to the *cis*-*trans* orientations of successive units occur in experiment.

5.4 ELECTRONIC STRUCTURE OF TDPP-TT MODELS

5.4.1 The Monomer Model

In the previous section, the geometrical aspects obtained by different DFT based methods were considered. The current section is devoted to the properties of the electronic structure. For this, the focus is on models motivated by the P(TDPP-TT) the monomer unit of which is depicted in Fig. 5.13 a).

First, the molecular orbital (MO) energies for the conformation where both DPP-thiophene and thiophene-TT bonds are in *trans* configuration as obtained from DFT calculations using B3LYP, PBE and VWN functionals as well as from DFTB are compared, see 5.14. The PBE and LDA functionals as well as the DFTB approach reveal smaller HOMO-LUMO gaps than the calculations with the B3LYP functional. The latter one yields HOMO and LUMO energies of -5.75 eV and -3.52 eV whereas the others give higher values for the HOMO and lower values for the LUMO. With -5.22 eV and -5.36 eV for HOMO and -4.01 eV and -4.12 eV for LUMO, the results obtained with PBE and VWN are similar but the energy levels of VWN are slightly lower than those of PBE. The frontier orbital energies obtained from DFTB calculations exhibit energies of about 0.5 eV higher compared to VWN so that the LUMO energy is in better agreement with the B3LYP result.

Furthermore, 5.14 illustrates the MO energies for the *cis*/*trans*, *trans*/*cis* and *cis*/*cis*

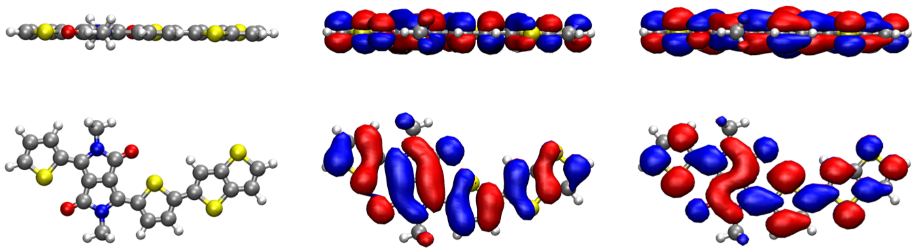
a) structure b) HOMO c) LUMO

Figure 5.13: Top and side view of the structure (a), the HOMO (b) and the LUMO (c) of the TDPP-TT monomer in *trans*/*trans* configuration

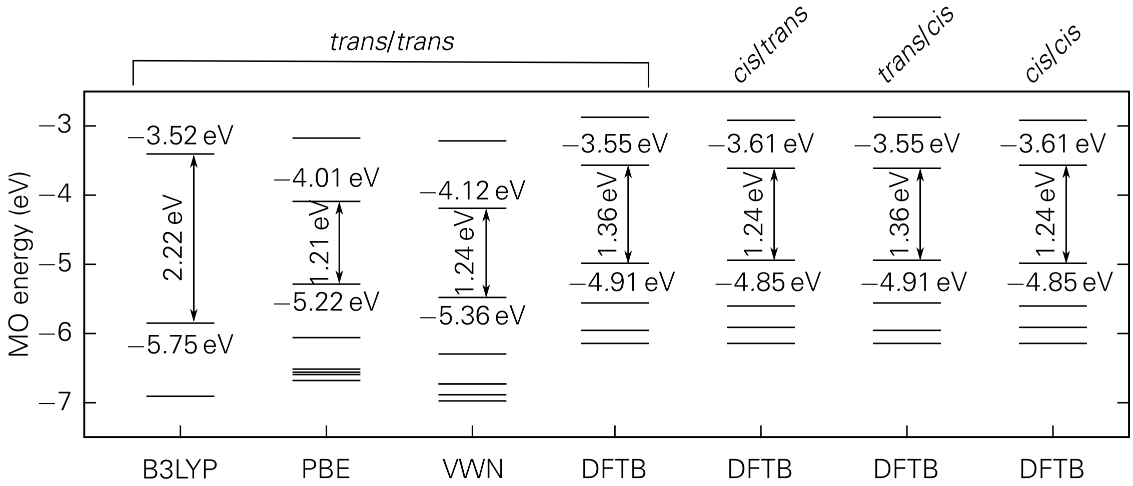

Figure 5.14: Comparison of the HOMO and the LUMO energies obtained by different DFT functionals and DFTB for different configuration of TDPP-TT monomer.

configurations of the TDPP-TT monomer obtained from DFTB. In this notation the first word describes the configuration between DPP and thiophene within the TDPP and the second the the one between the TT unit with respect to the thiophene. One can see, that the different conformations results in only small shifts of the energy levels. In particular, the HOMO-LUMO gap decreases merely by 0.12 eV when the TDPP compound is in *cis* configuration. Due to this minor dependency, the *trans*/*trans* model will be discussed in more detail in the following.

Figure 5.13 b) and c) depict top and side views of the HOMO and the LUMO as obtained from DFTB calculations. It should be noted that the spatial shapes, especially the positioning of the nodal surfaces, are in a good agreement between all considered methods so that a distinction by eye is impossible. Both HOMO and LUMO are formed by all atoms except the saturating hydrogens and show a nodal plane which coincides with the molecular plane. These delocalised π orbitals are fundamental for semiconducting properties in the polymer case.

By analyzing the gross orbital populations (GOPs) of the atoms belonging to the DPP, to the thiophenes, or to the TT units, the contributions of each subunit to the frontier orbitals can be considered, see Tab. 5.6. As outlined in section 1.3, the DA concept assumes that the HOMO is predominantly located at the donor unit and the LUMO on the acceptor unit [41]. For fluorene-benzothiadiazole (F8BT) DA copolymers for instance, a strong localization of LUMO on the acceptor was reported [160]. For other cases such as poly(phenylene ethynylene)s (PPE) based DA polymers, a HOMO localized on the donor was found [161]. The respectively other frontier orbitals, HOMO of F8BT and LUMO of PPE polymers, were delocalized but with higher contributions from the donor or acceptor unit, respectively. In other DA polymer systems both frontier orbital tend to localization whereas the HOMO resembles that of donor and the LUMO rather features the acceptor [162–164]. For the here investigated TDPP-TT model the DA concept assumes DPP to be the acceptor and the thiophene compounds to be the donor units. However, according to the GOP another behavior is observed: Both HOMO and LUMO are delocalized over the whole model, whereas the HOMO is mainly determined by the DPP unit and its neighboring thiophenes and only by 12±1.5% by the TT unit. In turn, the LUMO is with 16±1%, 25±1% and 16±1% predominantly located at the thiophene and the TT units but only by 46±5% at the DPP unit. Thus, the DA concept as discussed in standard the literature does not fully remain valid for the TDPP-TT monomer model as both components participate almost equally.

Comparing the results obtained by the different computational methods yields a surprisingly good agreement even though the used basis sets were different in the DFTB than for the DFT calculations. Thus, it can be concluded that the electronic structure is described equally well by all methods. This justifies using the computationally more efficient DFTB approach for larger systems in the following.

5.4.2 Oligomer and Polymer Models

In order to investigate the electronic structure of more polymer-like models, oligomer chains up to nine repeat units are considered in the following. Moreover, an infinite polymer chain is modeled by using periodic boundary conditions. For this only the DFTB method is used, since the large models require high computational efficiency and the reliability of DFTB has been shown above.

At first, the evolution of the MO energies is analyzed in order to study the effect of the model size on the electronic structure. Figure 5.15 shows the energy level diagrams for different oligomer lengths and the band structure of the infinite polymer. With increasing chain length, each state of the monomer model splits into several levels. Note that an oligomer with five successive units already exhibits a dense eigenvalue spectrum which

Table 5.6: Contributions of the left thiophene (T_1), the DPP, the central thiophene (T_2) and the TT units to HOMO and LUMO wave functions according to the GOP obtained from DFT using VWN, PBE, B3LYP functionals with DZP basis sets as well as from DFTB using the mio-1.1 parameter sets.

		T_1	DPP	T_2	TT
HOMO	VWN	12%	61%	14%	13%
	PBE	12%	61%	14%	13%
	B3LYP	12%	59%	16%	13%
	DFTB	12%	62%	15%	11%
LUMO	VWN	17%	48%	21%	14%
	PBE	17%	47%	22%	16%
	B3LYP	16%	48%	23%	13%
	DFTB	16%	43%	26%	15%

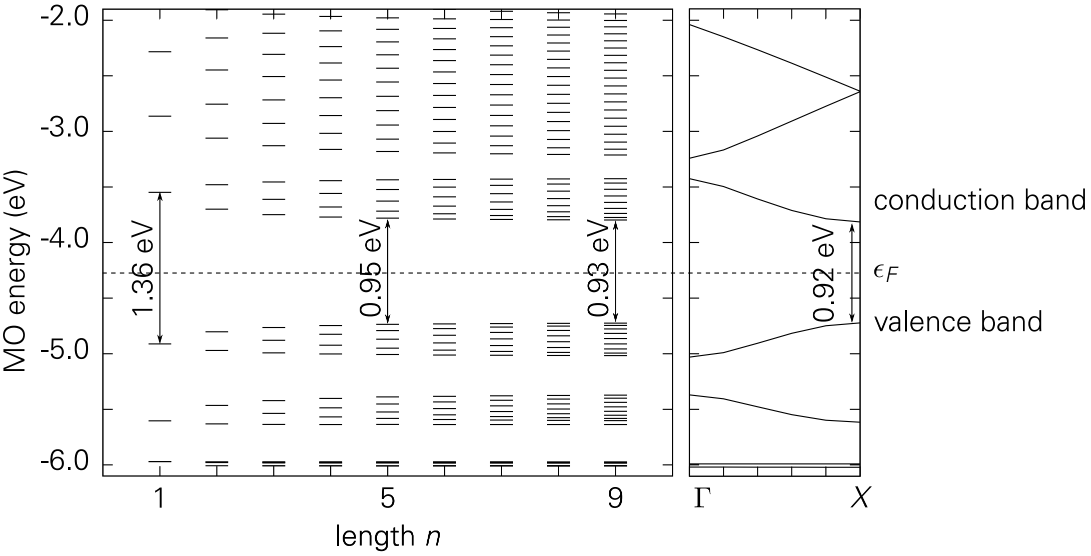

Figure 5.15: MO diagram for TDPP-TT oligomers of different lengths and band structure of the infinite polymer.

is in good agreement with the band structure of the periodic model. In particular, the level splitting spans the same energy windows as the bands of the infinite model do. Thus, the HOMO-LUMO gap becomes smaller with increasing chain length *n* and converges to the band gap of the infinite model. It shrinks from 1.36 eV for the monomer to 0.93 eV for the oligomer consisting of nine units. The band gap of the infinite polymer chain is found to be 0.92 eV.

In order to study to what extent the DPP, the thiophene and the TT units contribute to the individual MOs, the density of states (DOS) of the polymer and the projected density of states (pDOS) of each unit are illustrated in Fig. 5.16. Moreover, Tab. 5.7 summarizes the contributions for the oligomer models. To enable a comparison to the monomer and the polymer models, the GOPs were integrated over the energy range given in the first column and the contributions of the different DPP, the thiophene and the TT units were summed up. The two thiophene rings are distinguished according to the position with respect to the DPP unit: the ones on the left-hand side of the DPP units are referred to as T_1 and the ones to the right as T_2.

For all models, both valence and conduction band are spread over the whole chain. As already found for the monomer model, the DPP units contribute most to the corresponding orbitals. Longer chains yield a higher degree of delocalization such that the contribution of the DPP units decreases from 62 % to 54% for HOMO and from 43% to 37% for LUMO. Note that for the infinite polymer both thiophene units yield the same contributions since the polymer exhibits a higher symmetry and belongs to a Frieze group, which exhibits both inversion centers, whereas oligomer models belong to point groups that lack at least one inversion center. The model consisting of five repeat units shows good agreement with the infinite polymer chain.

To answer the question how the orbitals are spatially distributed over the chain, the

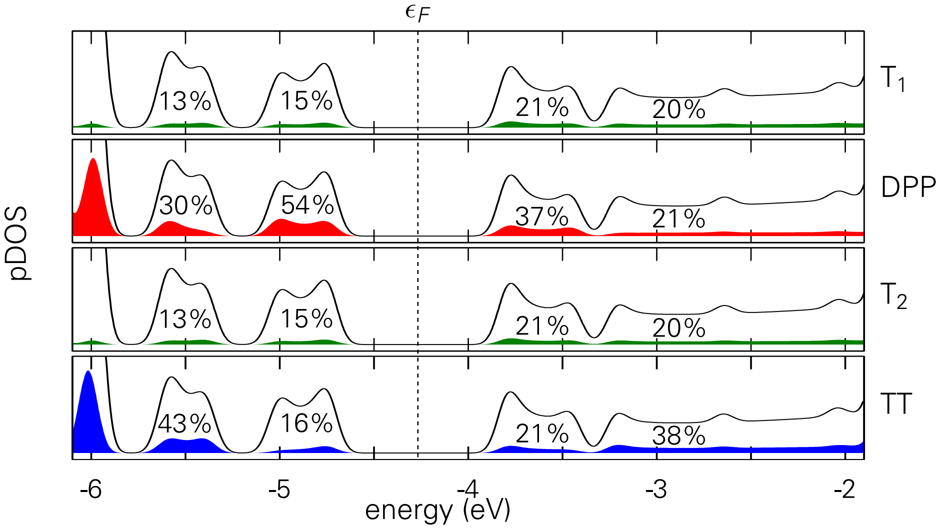

Figure 5.16: Total DOS (black line) and pDOS the thiophenes T_1 and T_2 (green), the DPP (red) and the TT (blue) for P(TDPP-TT).

individual subunits are grouped according to the repeat units instead of their chemical nature. Figure 5.17 shows the pDOS for the 1st, 2nd, 5th, 8th and 9th unit of the oligomer as well as the complete DOS of the 9-mer and the polymer models. The pDOS of the 5th unit as well as the DOS of the whole model agree with that of the polymer. Comparing the pDOS of the first and of the ninth unit to the DOS of the polymer, however, reveals significant differences. Both show lower contributions at the upper edge of the valence band (-4.6 eV) and at the lower edge of the conduction band (-3.8 eV). Moreover, a peak at -5.7 eV occurs in the DOS of the 9-mer. In this energy region, the DOS of the polymer is zero. As the pDOS of the ninth unit and the isosurface plot in Fig. 5.17 show, the corresponding electronic state is localized at the outmost unit of the model.

This leads to the following conclusions: The central units of an oligomer model are

Table 5.7: Contribution of T_1, DPP, T_2 and TT to the wave functions with energies in the given ranges as obtained from summing up the GOPs of the atoms constituting the units.

		1	2	3	4	5	6	7	8	9	∞
$-5.2 \ldots -4.5$ eV	T_1	12%	13%	14%	14%	14%	14%	14%	14%	14%	15%
	DPP	62%	59%	57%	56%	56%	56%	55%	55%	55%	54%
	T_2	15%	15%	15%	15%	15%	15%	15%	15%	15%	15%
	TT	11%	13%	14%	15%	15%	15%	16%	16%	16%	16%
$-4.0 \ldots -3.3$ eV	T_1	16%	18%	19%	19%	20%	20%	20%	20%	20%	21%
	DPP	43%	40%	39%	39%	38%	38%	38%	38%	38%	37%
	T_2	26%	24%	23%	22%	22%	22%	21%	21%	21%	21%
	TT	15%	18%	19%	20%	20%	20%	21%	21%	21%	21%

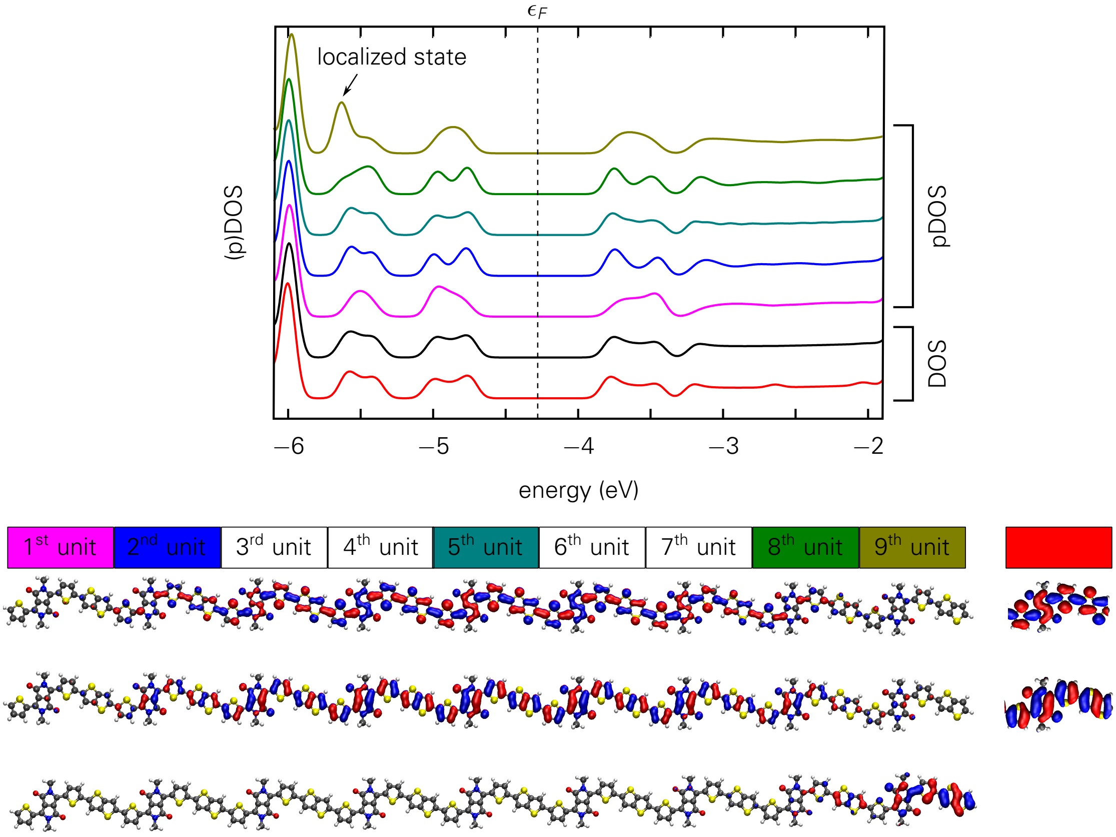

Figure 5.17: Top: pDOS of individual units of the TDPP-TT 9-mer model in comparison with the DOS of the 9-mer (black) and the DOS of an infinite chain (red). Bottom: Isosurface plot of HOMO and LUMO wave function as well as the localized in-gab state.

well described by using periodic boundary conditions and the termination effects are confined to the outmost two units. Thus, studying the polymer properties by using short chains instead of long oligomer models is sufficient. The terminating units of such model, however, behave differently than the central ones. For instance localized wave functions can be found. In the here presented case, this effects occurs in low energy regions only such that it is concluded that they do not affect the frontier orbitals. Thus, the termination effects can be neglected and the infinite models using periodic boundary conditions are sufficient to long range conjugated polymers. It is noted, however, that in experiment termination effects might have an impact, especially if specific endgroups are chosen. Such as surface states for bulk systems, or edge states for 2D materials, the existence of localized states at the termination unit of 1D systems may be concluded. The behavior of localization due to the termination of the chain cannot only be found for molecular models as reported in this study. Considering a very simple model of successive quantum wells of different depth and width yields comparable results in both the DOS and shape of wave functions, see Appendix B. Thus, it is stated that designing semiconducting polymers with well-defined termination groups might allow a tailoring of localized states; possibly even within the HOMO-LUMO gap.

5.5 SUMMARY AND CONCLUSIONS

In this chapter the geometry and the electronic structure of small models motivated by the building blocks of DPP-based DA polymers were studied. For this the results of different levels of theory were compared. The following observations were deduced from analyzing the structural aspects: First, the TDPP monomer exhibits planar structures as local minima of the energy landscape of possible orientations. The employed DFT methods, however, yield different energetic sequence for them. Second, adjacent thiophene units do not adopt planar structures when considered as isolated chains. Even for long oligomer chains the planar-*cis* conformation remains a transition state. When π-π stacks are considered, however, the models tend to planar configurations. The energy gain from the weak interaction of aligned chains compensates the loss related to an rotational barrier when it is lower than 100 meV. It is therefore concluded that non-planarity of isolated systems can be neglected when the molecular system is modeled according to a crystalline phase.

To quantify, which configurations exist in the experimental set-up, STM images of DPP-2T polymers were superimposed with DPP-2T-DPP models. It was found that DPP-thiophene connections show a strong preference for the *cis* configuration whereas adjacent thiophenes exhibit both *cis* and *trans* configurations frequently. It is therefore concluded that it is necessary to carefully study whether or not a property is sensitive with respect to this isomeric degrees of freedom before drawing conclusions from only one representative.

Comparing the electronic structures as obtained by the different simulation methods led to the following observations. Although calculations with LDA and PBE functionals yield smaller HOMO-LUMO gaps than those with the B3LYP functional, the respective MOs agree remarkably well. In particular, DFT with different functionals and DFTB using the mio-1-1 parameters yield consistent results regarding to the positioning of nodal surfaces and the contributions of the individual subunits to the frontier orbitals. Hence, it is concluded that for investigations on a quantum theory level all methods are equal in accuracy. Due to its computational efficiency DFTB is therefore the best choice for this systems.

Investigating the frontier orbitals of P(TDPP-TT) models revealed differences compared to other DA compounds reported in literature. Instead of partial localizations, where the HOMO and the LUMO are mostly determined by the donor and the acceptor units, respectively, both wave functions are delocalized over the whole polymer models. Remarkably, the DPP unit showed a stronger contribution to the HOMO than to the LUMO although it is considered the acceptor moiety of the DA polymer.

6 INTER-MOLECULAR CHARGE TRANSFER BETWEEN DONOR-ACCEPTOR POLYMERS

6.1 INTRODUCTION

Within a thin film, conjugated donor-acceptor (DA) polymers tend to align parallel and form π-π stacks [165]. In such systems, both transport mechanisms discussed in chapter 4 may occur. For ideal infinite chains, delocalized π-systems and electronic bands are formed as exemplarily shown in Section 5.4.2. In such a system, the electronic transport is fast compared to the movement of the nuclei and can therefore be modeled as adiabatic transport. In real systems, however, the periodicity of polymers is usually interrupted. On the one hand, various defects occur, e.g. due to the synthesis or the fabrication

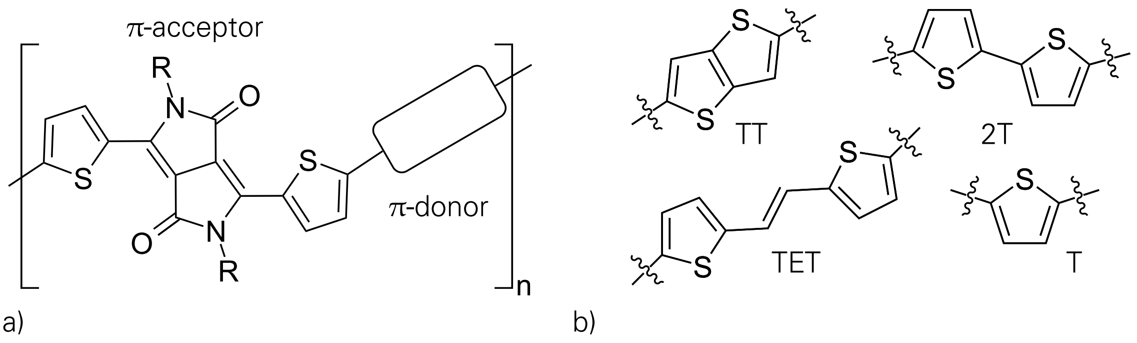

Figure 6.1: a) General structure of considered DA polymer models: DPP with two thiophene rings (TDPP) form the acceptor unit. b) Systems considered for the donor unit: thieno[3,2-b]thiophene (TT), 2,2'-bithiophene (2T), 1,2-di(2-thienyl)ethylene (TET) and single thiophene (T).

process of electronic devices. For instance, the alternating DA copolymer sequence can be broken due to donor-donor or acceptor-acceptor homocoupling or due to the incorporation of compounds which originate from the solvent or the catalyst [166–168]. Moreover, the polymer backbone can exhibit conformational changes like torsion or point defects [169, 170]. On the other hand, fluctuations may also cause localizations of the wave functions even for ideal, infinite systems. Consequently, the conjugated π-system is typically confined to a few repeat units. For PT, conjugation lengths of 6 up to 25 thiophene units meaning 2. . . 10 nm are reported [171–173]. Thus, charge transfer (CT) processes between adjacent chains have to take place in order to obtain conductance through the whole film. Such an inter-molecular transfer is of hopping nature and can be modeled by the Marcus theory as described in chapter 4.3. According to Eq. (4.12), the transfer rate is determined by the reorganization energy λ, the electronic coupling T_{AB} and the driving force ΔE.

In this chapter, these Marcus rates are calculated for DA polymer models. The TDPP model studied in section 5.3.1 is therefore considered as acceptor moiety and different thiophene compounds as donor units, see Fig. 6.1. One task of this research is to investigate the dependency of the quantities on the chemical structure. Another on is to search for correlations between the orientations with highest transfer rates to those with the highest stability.

6.2 COMPUTATIONAL DETAILS

6.2.1 Molecular Models

Most studies reported in the literature mainly consider small models—typically monomers or dimers of the repeat unit—to calculate the inter-molecular CT. These simple models, however, are only sufficient for direct stacks [174–176]. Shifting the two molecules relative to each other reduces the interaction region and results in a poorly described energy and in small transfer rates. Thus, this approach is limited to cases where the direct stacking or small displacements from it are the most favored orientations. Contrary to that, in this work TDPP based DA polymers were studied using periodic boundary conditions. This enables the calculation of the interaction energy and the electronic coupling for any shift of two chains.

According to the results from the previous chapter, each of the polymers can adopt several isomeric structures. To describe the polymers by means of periodic models, a translational symmetry is required. Due to the pentagonal structure of thiophene, this can only be fulfilled for an even number of pentagons in the repeat unit. More specifically, the models have to contain an equal number of up and down-pointing sulfur atoms. To limit the system size, the focus is on those models for which the translation demand is fulfilled for a single repeat unit.[1] The resulting four models are referred to as *trans/trans*, *trans/cis*,

---

[1] In the present study, only when a single thiophene is considered as the donor unit, this demand can not

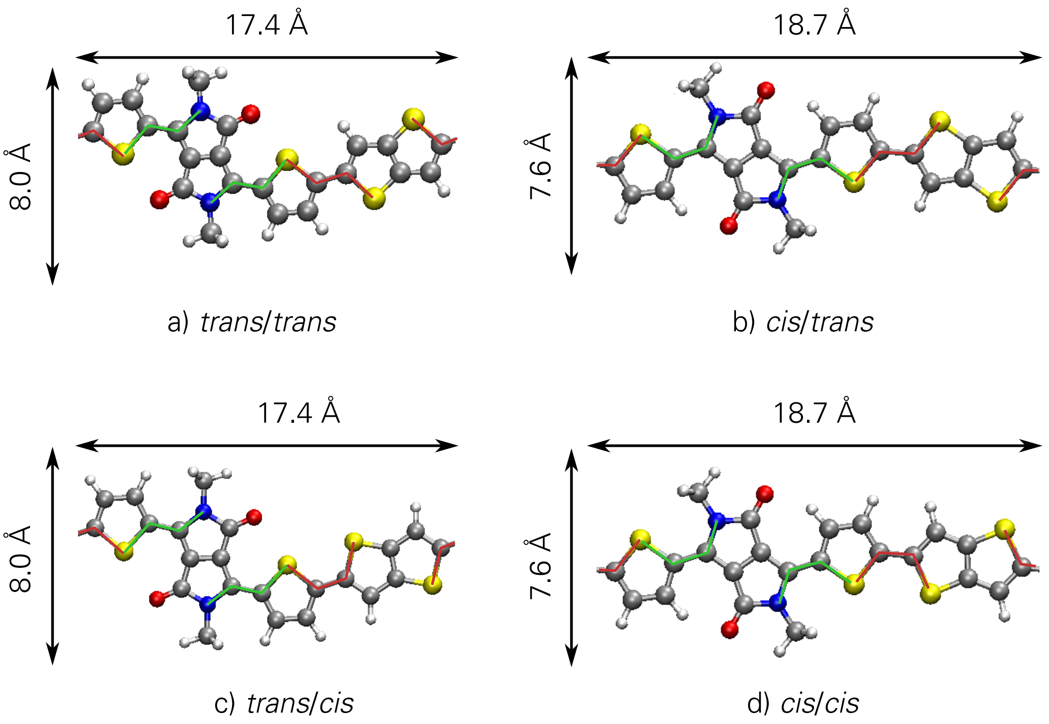

a) *trans*/*trans* b) *cis*/*trans* c) *trans*/*cis* d) *cis*/*cis*

Figure 6.2: The TDPP-TT model in *trans*/*trans* (a), *cis*/*trans* (b), *trans*/*cis* (c) and *cis*/*cis* (d) configurations. The highlighted bonds denote the *cis*-*trans* isomerism between DPP and thiophene (green) and thiophene and the TT unit (red)

cis/*trans* and *cis*/*cis* isomers. In this notation the first word describes the configuration between DPP and thiophene within the TDPP and the second the conformation of the donor unit with respect to the thiophene. The respective structures are exemplarily depicted in Fig. 6.2 for the TDPP-TT model. Note, that the alignment of the units affect the length of the repeat units and the expansion perpendicular to the backbone.

6.2.2 Methods and Parameters

SCC-DFTB simulations [86, 87] were performed using the program package DFTB+ [147]. It is computationally most efficient and reproduces geometries and the electronic structures in good agreement with standard DFT approaches, as it is shown in chapter 5, Appendix C and many publications [87, 126, 127, 148, 149, 177]. The mio-1-1 parameter set [87, 177] was used for calculations of the fragment orbitals (FOs) and optimization purposes. Since they were generated using a contraction potential, however, they do not reflect the extended nature which is needed to derive the coupling Hamiltonian matrix $\hat{H}'_{AB}$. Hence, a different parameter set was used for this purpose which was derived from non-contracted atomic orbitals. For this, Eq. (3.36) was solved without the $(r/r_0)^2$ term. In this way, the long range part of the wave function is better described and ensures that the interaction of the two neighboring fragments is fully covered. To account for dispersion

---

be fulfilled. Thus, in this case two repeat units are needed.

interaction in π-π-stacks, the empirical correction from universal force field [103, 107] was used.

The use of DFTB for the calculation of the coupling elements according to Eqns. (4.27) and (4.26) was justified by Kubas *et al.* who benchmarked different DFT based methods against high-level *ab inito* calculations [126, 127]. In the present work, own subroutines were implemented based on the output formats of DFTB+. To test this implementation, small molecular models were considered and compared to standard DFT approaches as implemented in the SCM ADF program package [123, 144]. For more details, see Appendix C.

6.2.3 Working Strategy

The individual geometries of the polymers were obtained starting from monomeric systems saturated by hydrogen atoms. These models were then optimized for the neutral and charged states followed by single point calculations for each charged state in the geometry of the other one. In this way, the reorganization energy λ was obtained. The monomeric system was used instead of the infinite polymer for the following reasons: Firstly, λ is a local quantity such that the influence of adjacent units is small. Secondly, the delocalization effect which arises as an artifact of Kohn-Sham approaches is partially suppressed when the finite system is considered. Lastly, calculations of charged systems with periodic boundary conditions are in principle impossible without the corresponding counter charge which contradicts to the definition of λ in the Marcus theory. Thus, the monomer model is the best choice for the calculation of the reorganization energy.

As outlined in section 4.3.5, the coupling element depends on the orientation of two molecules between which the CT takes place. In order to consider chains which are shifted relative to each other the finiteness of monomer or oligomer models is inappropriate. Because of this, periodic boundary conditions were introduced to describe infinite polymers. As shown in Fig. 5.15, the band edges of the conduction and the valence band are obtained at the X point. Considering an even number of repeat units per periodic cell guaranties that the parity of the highest occupied molecular orbital (HOMO) and the lowest unoccupied molecular orbital (LUMO) are the same at the boundaries of the unit cell for all systems. It is therefore sufficient to sample the Brillouin zone at the Γ point when two repeat units per unit cell are taken into account.

In prder to estimate the interaction energy of stacked polymers ΔE^{stack}, two chains per unit cell were considered. Keeping the geometry of the individual chains constant, three degrees of freedom remain for parallel π-π stacked chains, see Fig. 6.3: The shift along the backbone which is referred to as x direction, the shift perpendicular to x but with constant π-π stacking distance (y direction), and last, the direction of the stacking (z direction).

In order to describe the polymer in a regular stacking, periodic boundary conditions were also introduced in z direction. In this way, a more correct stacking distance for stable configurations is ensured since the interaction to both neighboring chains is included. To

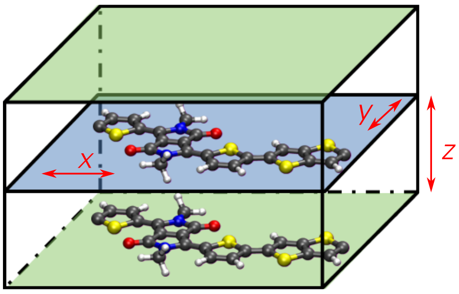

Figure 6.3: Schematic sketch of considered π-π stacks. Shifts along (x) and perpendicular to the polymer backbone (y) as well as the stacking distance (z) represent the considered degrees of freedom.

derive the coupling Hamilton matrix $\hat{H}'_{AB}$, however, the chain pair was considered as an isolated stack in order to exclude next-nearest neighbor interactions. For this purpose, the periodicity in z direction was switched off.

For the three parameters, which define the stacking geometry $\vec{R}^{stack}$, a regular grid was generated. Since the absolute unit length does not only depend on the chemical structure of the donor, but also on the orientation of the units, the shifts along the polymer are referred to in fractions of the individual unit length. Due to the symmetry of the considered systems, a relative shift in x direction up to the half length of the repeat unit needs to be studied. In total 51 equidistant points in x direction in the range of 0% to 50% of the unit length were used. In y direction, 41 equidistant points within a total range of ±5 Å were considered. The distance of the two chains was chosen in the range of 3.2 Å and 3.6 Å in steps of 0.01 Å. These values turned out to reproduce a smooth landscape of the interaction energy between the two chains. The boundaries were chosen to ensure that all local minima are covered.

Note, that for each model two possible π-π stacking scenarios exist. One, in which the units of the upper chain point in the same direction as the corresponding units of the lower one and another one, for which they point in opposite directions. The first scenario is referred to as parallel stacking while the second is called antiparallel stacking.

6.3 THE REORGANIZATION ENERGY

As shown in Fig. 6.4 a), seven energy values need to be calculated to derive the individual contributions λ^{0}_{+1}, λ^{+1}_{0}, λ^{-1}_{0} and λ^{0}_{-1}. In this notation, the lower index indicates the neutral, the anionic or the cationic state of the system, while the upper index gives the considered equilibrium geometry.

The obtained results of the reorganization energies depend on both the choice of the donor part and the *cis*-*trans* configuration of successive units. Since features result in different monomer lengths, Fig. 6.4 shows λ^{+1}_{0}, λ^{0}_{+1} , λ^{0}_{-1} and λ^{-1}_{0} in dependence of the end-to-end distance of the different models. Three major conclusions can be drawn

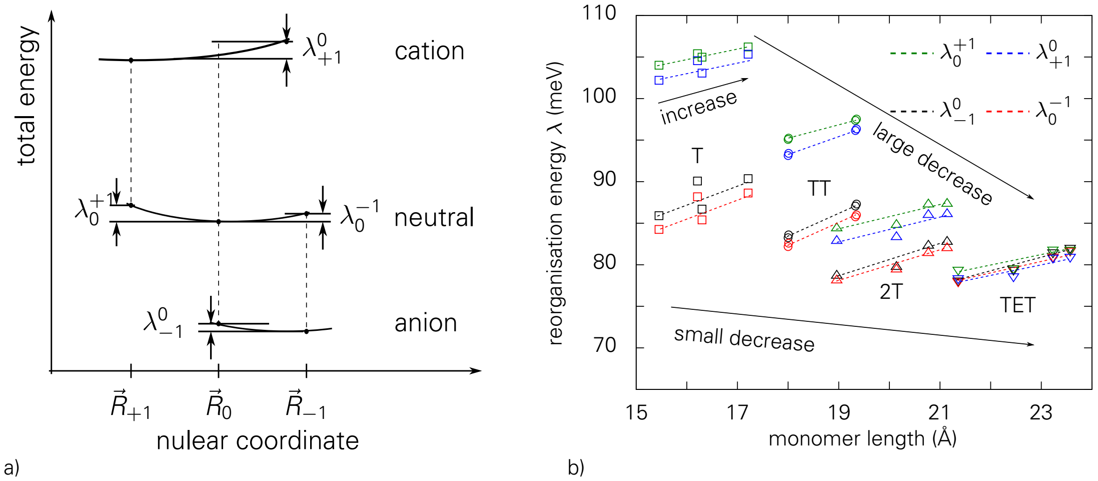

Figure 6.4: Left: Schematic sketch of the total energy for neutral, anionic and cationic state with the respective equilibrium geometries $\vec{R}_0$, $\vec{R}_{+1}$ and $\vec{R}_{-1}$. Right: Reorganization energies λ_0^{+1} (green), λ_{+1}^{0} (blue) , λ_{-1}^{0} (black), and λ_0^{-1} (red) for TDPP-T (□), TDPP-TT (○), TDPP-2T (△) and TDPP-TET (▽) in dependence of monomer length.

from it. First, for all models and all configurations it holds $\lambda_{+1}^{0} \approx \lambda_0^{+1}$ and $\lambda_{-1}^{0} \approx \lambda_0^{-1}$. Since λ indicates the curvature of the energy landscape, these agreements justify using the same vibrational frequencies ω_ξ for both $E^\mu(\vec{R})$ and $E^\nu(\vec{R})$ in Eq. (4.10). It can therefore be concluded that this approximation of the Marcus theory is fulfilled for these systems. Second, λ is correlated with the *cis*-*trans* configuration of successive units and the different end-to-end distances originating from it. In all cases, the reorganization energies of the *trans*/*cis* configuration (smallest end-to-end distance) are of about 5 meV smaller than those of *cis*/*trans* (largest end-to-end distance). Third, comparing the values of the different donor units, decreasing trends are observed for all reorganization energies when the length of the donor unit is increased. In particular, substituting TET for a single thiophene ring as the donor unit reduces λ_0^{+1} and λ_0^{+1} by about 25 meV. The reorganization energies λ_0^{-1} and λ_{-1}^{0} decrease only by 7 meV and therefore much less. On the one hand, the decreasing trend may partially arise from the fact that Kohn-Sham DFT tends to delocalize the charge density so that local changes are smaller when the system is larger. On the other hand, the larger decrease of λ_0^{+1} and λ_{+1}^{0} describing the transfer of a positive charge is in line with the fact that the donor unit was varied. It shows that the transport properties of holes have a higher dependence on the choice of the donor moiety than those of the electron transport.

6.4 THE COUPLING ELEMENT

6.4.1 Dependence on the Stacking Geometry

As mentioned before, the values of the coupling depend on the isomeric structure of each model but also on the orientation $\vec{R}_{stack}$. For each donor unit depicted in Fig. 6.1,

a) parallel stacking

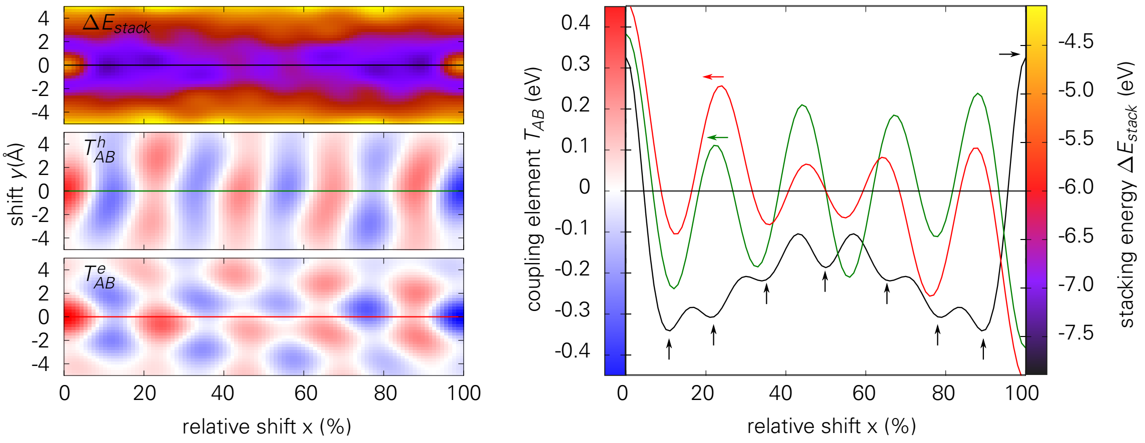

b) antiparallel stacking

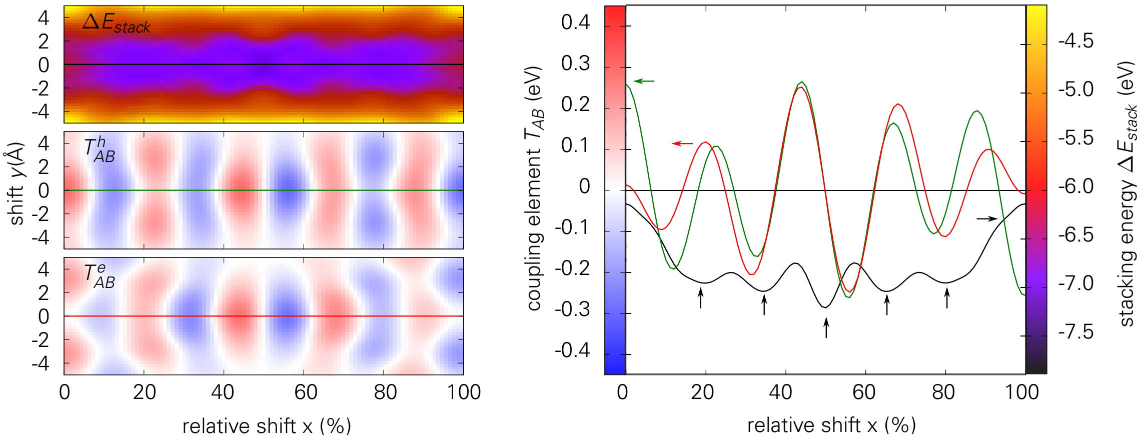

c) frontier orbitals

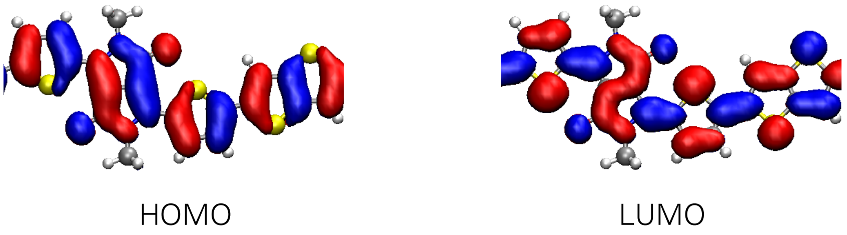

Figure 6.5: Interaction energies ΔE_{stack} and the coupling elements for hole and electron transfer ,T^h_{AB} and T^e_{AB}, for parallel (a) and antiparallel (b) stacked chains in *trans*/*trans* configuration and isosurface plots of HOMO and LUMO (c). The color plots on the left give the dependencies on x and y for $z = 3.5$ Å. The corresponding scales are given in the right graphs which shows the dependencies of ΔE_{stack} (black, right scale), T^h_{AB} (green, left scale) and T^e_{AB} (red, left scale) on x for $y = 0.0$ Å.

the same qualitative dependencies on the stacking geometry were observed. Here the focus is restricted to the TDPP-TT model.

The figures 6.5, 6.6, 6.7 and 6.8 show the coupling elements for the holes T^h_{AB} and

a) parallel stacking

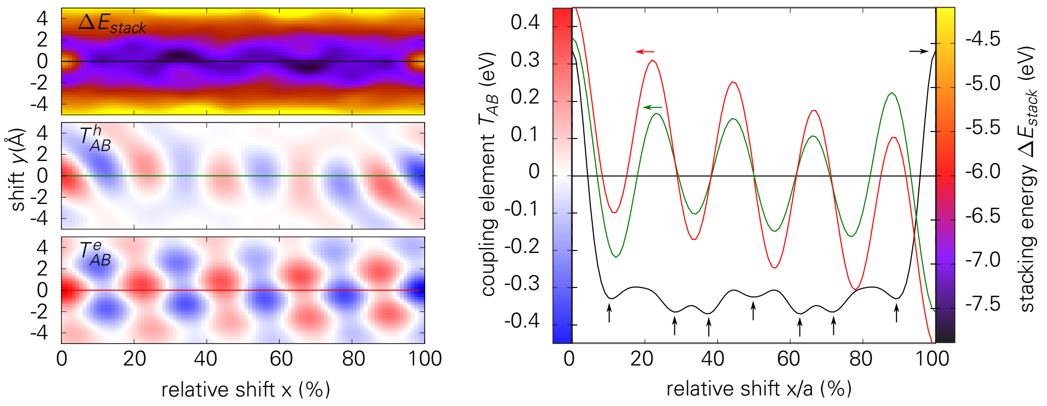

b) antiparallel stacking

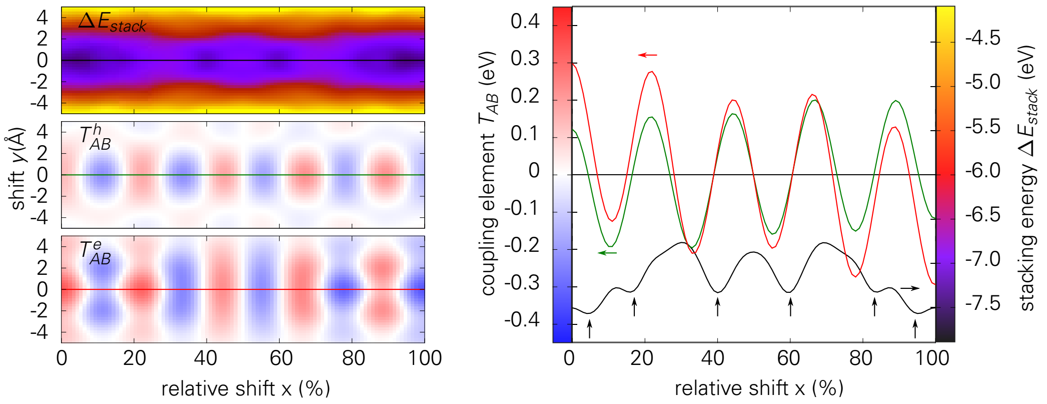

c) frontier orbitals

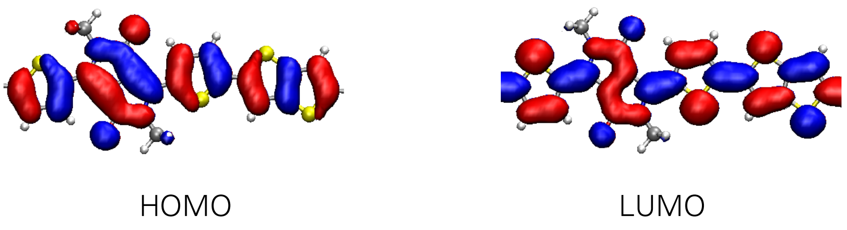

Figure 6.6: Same as Figure 6.5 for *cis*/*trans* configuration.

electrons T^e_{AB}, as well as the interaction energies ΔE_{stack} for a stacking distance of $z = 3.5$ Å. The latter were obtained by subtracting the energies of the isolated chains from those of the stacks. In each of them, the upper plots show the results for the parallel stacking, where the results for antiparallel orientations are given in the central one. For each isomeric structure, the dependencies of ΔE_{stack} and $T^{h/e}_{AB}$ on x and y are shown in the color plots on the left. The graphs on the right show the dependencies on the shift in x direction for $y = 0.0$ Å in more detail. Below, the frontier orbitals HOMO and LUMO are depicted, the spatial shape of which partially explains the dependency of the coupling

a) parallel stacking

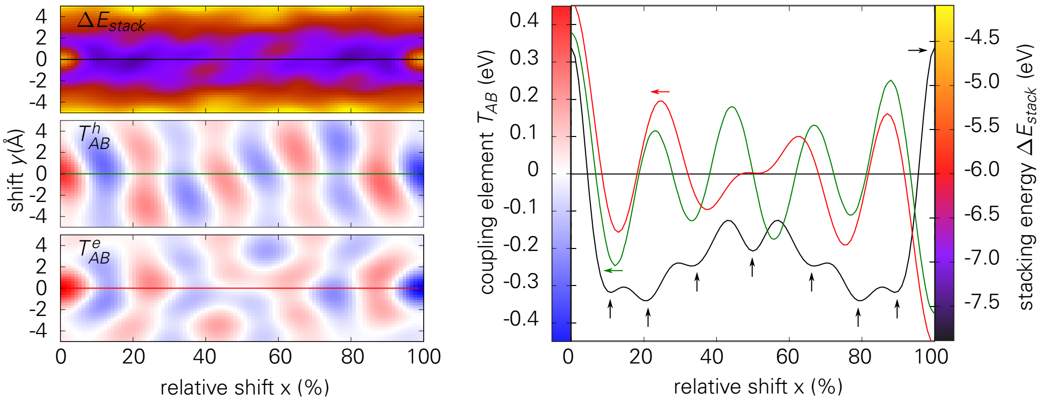

b) antiparallel stacking

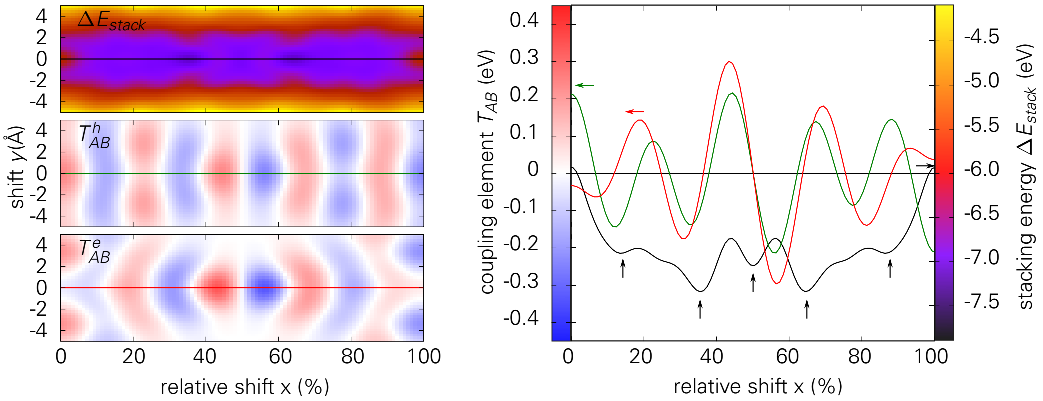

c) frontier orbitals

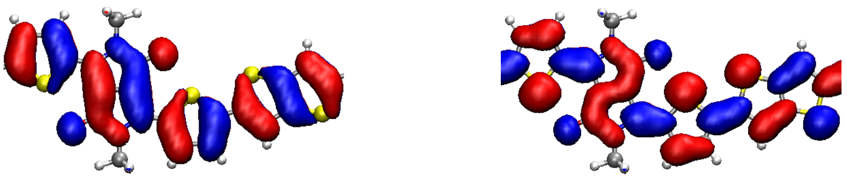

HOMO LUMO

Figure 6.7: Same as Figure 6.5 for *trans*/*cis* configuration.

elements on the stacking arrangement $\vec{R}^{stack}$.

For the energies ΔE_{stack} the following observation were made. For all models, the direct stacking with $x = y = 0$ Å in parallel orientation yields a maximum in energy. This is due to the methyl units attached to the DPP, possessing hydrogen atoms which are above and below the molecular plane. For the direct stacking, the distance between these atoms is smaller than 2.0 Å so that their repulsion renders this orientation unfavored. Except for these cases, configurations with $|y| \leq 2$ Å form a valley-like energy landscape. Displacements with $|y| \geq 3$ Å yield strong increases of the energy which is related to

a) parallel stacking

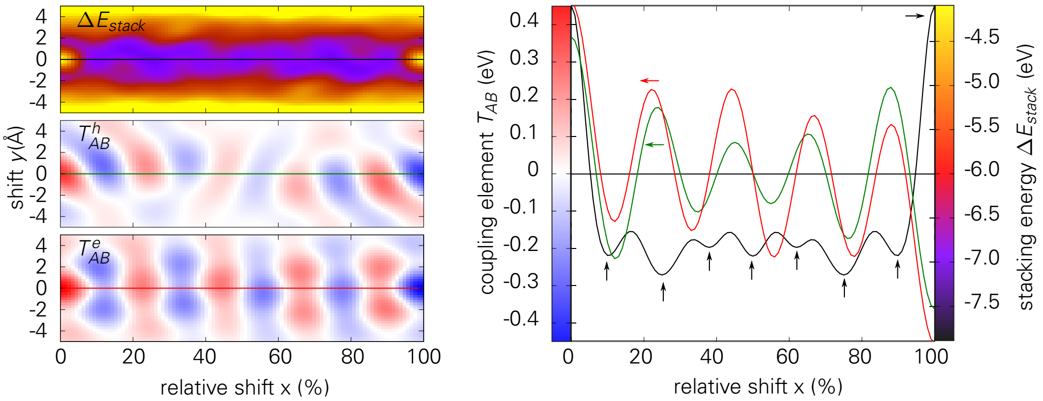

b) antiparallel stacking

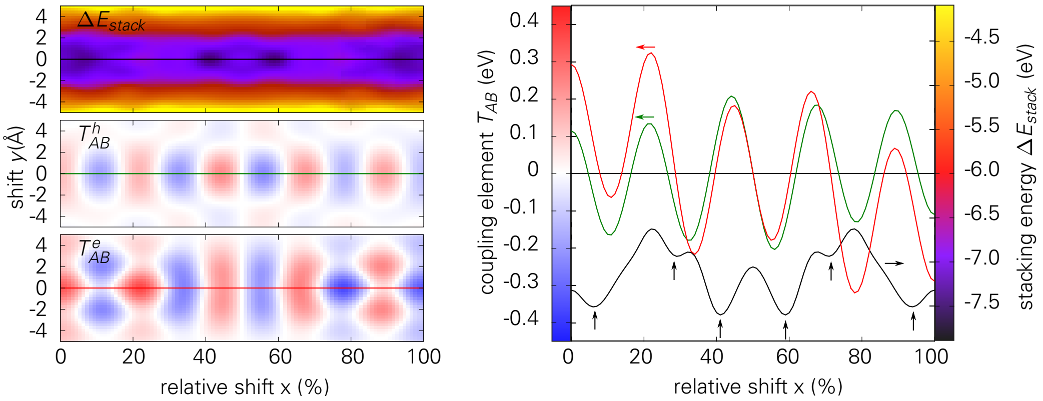

c) frontier orbitals

HOMO LUMO

Figure 6.8: Same as Figure 6.5 for *cis*/*cis* configuration.

the the vanishing π-π interaction. Note, that for *trans*/*trans* and *trans*/*cis* configurations, see Fig. 6.5 and Fig. 6.7, these valleys are broader than those of the *cis*/*trans* and *cis*/*cis* isomers, see Fig. 6.6 and Fig. 6.8. This originates from differently large extension in y direction. The shifts along the polymer direction yield several local minima as indicated by the vertical arrows in each graph. One should note, however, that the actual stable configurations typically occur for small shifts in y direction.

For the parallel stacks, the most stable shifts are typically in the range of 20-30% of the unit length. In these cases, the DPP unit of the upper chain is positioned above one thiophene of the lower chain. The absolute shift of half of the unit length, which refers to the orientation where the acceptor is on top of the donor, occurs as a local minimum for all parallel stacks. The corresponding energy, however, is high compared to those of other minima. For the antiparallel stacks, the most stable configurations occur for shifts of 40% up to 50% of the unit length. In those geometries, the DPP unit of the upper chain is more close to the TT than toDPP unit of the lower polymer. This means, that for the antiparallel stacking scenario the acceptor favors the positioning on top of the donor. This difference of stable orientations between the parallel and the antiparallel stacking scenario may arise from local dipole interactions between the chains. Since DPP possesses polar groups, the interaction to adjacent chains strongly depends on their relative orientation. Hence, the simple picture of pairwise interaction between partially positive donor on one chain and partially negative acceptor on the other one, the electrostatic interaction of which stabilizes the donor-next-to-acceptor orientation, does not represent a sufficient description. The interaction is much more complex and requires a careful consideration case by case.

Considering the couplings T_{AB}^{h} and T_{AB}^{e} leads to the following. Since the overlap of the FOs of the two chains is maximal for direct stacking geometries, both T_{AB}^{h} and T_{AB}^{e} show maxima. When the chains are displaced, the overlap becomes smaller and thus T_{AB} decreases. For stacks where the overlap vanishes, the coupling becomes zero. Further displacements increase the coupling again but with opposite sign. This leads to and oscillating behavior of T_{AB}^{h} and T_{AB}^{e}. Due to the different positioning of the subunits compared to the polymer backbone, the individual shapes of the plots in the figures 6.5, 6.6, 6.7 and 6.8 are unique for each configuration of the polymer. The number of oscillations of T_{AB} for shifts along the polymer backbone is the same for all models, but the intensities vary in different manners. For instance, the nodal surfaces of the HOMO of the *trans*/*trans* model are almost perpendicular to the polymer backbone while those of the LUMO are rather diagonal, see Fig. 6.5c). Thus, the oscillations of T_{AB}^{h} have a higher amplitude for shifts between 30% to 70% compared to T_{AB}^{e}. Turning the DPP unit into *cis* configuration, see Fig. 6.6 a), the amplitudes of T_{AB}^{h} decrease, because now the nodal surface at the DPP unit is diagonal to the backbone. Similarly, the plots of the other configurations can be correlated with the shapes of the frontier orbitals.

6.4.2 Average Value Approaches

So far, the dependency of the coupling element on various stacking orientation were discussed. The variations of T_{AB}^{h} and T_{AB}^{e}, which arise from the dependency of the spatial shape of the frontier orbitals, cause a crucial impact of the stacking orientation on the coupling elements. Uncertainties of about 1 Å causes changes of the coupling element of 200 meV and more. In order to study to what extent the chemical structure is affecting the transfer properties and to compare different systems, characteristic quantities are needed rather than the complex dependencies on the stacking orientations.

For this purpose, different approaches are possible to obtain a single quantity that represents each system. Considering the most stable stacking configuration $\vec{R}_{optim}$ is the simplest choice. As the plots in Figs. 6.5, 6.6, 6.7 and 6.8 suggest, however, several local minima with somewhat similar energies are present. Thus, it is likely that different configurations occur in real systems. It is furthermore to be expected, that due to thermal vibrations the areas which surround the local minima might be of importance as well. Hence, averaging over all considered stacking formations using a Boltzmann factor as statistical weight can be performed. Since the coupling enters the Marcus formula in squared form, the average value of T^2_{AB} has to be evaluated:

$$\langle T^2_{AB} \rangle_B = \frac{\int T^2_{AB}(\vec{R}) \exp\left(-\frac{E(\vec{R}) - E_{\text{global}}}{\mathrm{k_B} T} \right) \mathrm{d}\vec{R}}{\int \exp\left(-\frac{E(\vec{R}) - E_{\text{global}}(\vec{R})}{\mathrm{k_B} T} \right) \mathrm{d}\vec{R}}, \tag{6.1}$$

As a third version, a quasi-Boltzmann statistical approach can be introduced, where the energy of the "nearest local minimum", $E_{\text{loc}}(\vec{R})$, is substituted for E_{global}:

$$\langle T^2_{AB} \rangle_{QB} = \frac{\int T^2_{AB}(\vec{R}) \exp\left(-\frac{E(\vec{R}) - E_{\text{loc}}(\vec{R})}{\mathrm{k_B} T} \right) \mathrm{d}\vec{R}}{\int \exp\left(-\frac{E(\vec{R}) - E_{\text{loc}}(\vec{R})}{\mathrm{k_B} T} \right) \mathrm{d}\vec{R}}, \tag{6.2}$$

In this context, the "nearest local minimum" is referred to as that one where a steepest descent optimization ends which started from $\vec{R}$. This ansatz can be justified for the following reasons: The local minima of the interaction energy of stacked chains are separated by barriers > 0.3 eV per interacting unit. While fabricating organic devices, it is rather unlikely, that all polymers will align in the most stable conformation. Equilibration to the global minimum because of thermal diffusion is improbable since a reorientation on a large scale would be needed. Furthermore, the long alkyl side-chains may affect this diffusion as well. It is therefore assumed that the individual chains will equilibrate to the "nearest local" rather than to the global minimum. Thus, the approach reflects a poorly annealed polymer film composed of subregions that are locally in thermodynamic equilibrium.

Table 6.1 summaries $T_{AB}(\vec{R}_{opt})$, $\sqrt{\langle T^2_{AB} \rangle_B}$ and $\sqrt{\langle T^2_{AB} \rangle_{QB}}$ for all the different models of two stacked TDPP-TT chains. The values range from 12 meV up to 171 meV for holes and 9 meV up to 161 meV for electrons. When the most stable configuration is considered only, the obtained values are typically smaller than the averaged values. Only for the *trans*/*trans* isomer in parallel and the *cis*/*cis* isomer in antiparallel stacking, $T^h_{AB}(\vec{R}_{opt})$ yields a larger value than $\sqrt{\langle T^2_{AB} \rangle_B}$ and $\sqrt{\langle T^2_{AB} \rangle_{QB}}$. These cases can be related to the minima at about x =16% in Fig. 6.5 a) and at roughly x =41% and Fig. 6.8 b), respectively. For the latter case, however, for $x = 5\%$ another minimum of similar energy exists, but with much smaller T^h_{AB}.

In the remaining cases, the situation is vice versa. Typically the most stable orientation yields small couplings. Thus, averaging over the configurations increases the mean value.

Table 6.1: Coupling elements as obtained from the most stable configuration $\vec{R}_{opt}$ and the average value approaches explained in the text. The maximum and minimum value of each approach is highlighted in bold. Values are given in meV.

configuration			holes			electrons		
	DPP-T	T-donor	$T^h_{AB}(\vec{R}_{opt})$	$\sqrt{\langle T^2_{AB}\rangle_B}$	$\sqrt{\langle T^2_{AB}\rangle_{QB}}$	$T^e_{AB}(\vec{R}_{opt})$	$\sqrt{\langle T^2_{AB}\rangle_B}$	$\sqrt{\langle T^2_{AB}\rangle_{QB}}$
P	*trans*	*trans*	158	144.2	**119**	29.1	62.1	**55.1**
P	*cis*	*trans*	76.3	70.1	97.8	81.9	72.8	92.3
P	*trans*	*cis*	17.9	**43.7**	99.1	22.9	82.8	89.5
P	*cis*	*cis*	22.7	77.4	80.6	111	152	**116**
A	*trans*	*trans*	**12.4**	45.9	97.3	**9.1**	**35.3**	75.5
A	*cis*	*trans*	13.8	54.3	**74.6**	**154**	**161**	113
A	*trans*	*cis*	115	119	95.5	47.3	67.9	114
A	*cis*	*cis*	**171**	**163**	101	96.7	90.9	98.4
RMS			96.3	99.5	96.4	83.3	99.8	96.3

The two statistical averages lead to different values in most cases but no correlation can be noticed. Taking the averages over all considered configurations, however, yield similar values for both holes and electrons. Note, that due to the squared nature of T_{AB} in the Marcus formula, the root mean square (RMS) has to be considered rather than the mean value. Thus, both methods, $\sqrt{\langle T^2_{AB}\rangle_B}$ and $\sqrt{\langle T^2_{AB}\rangle_{QB}}$, might be applicable to compare the results for different chains. The quasi-Boltzmann approach is more physical because local minima have a stronger impact than other configurations with the same total energy.

The systems using thiophene, 2T, or TET as donor were analyses in the same manner as the one reported so far for TT. For each, all eight stacking orientations were considered. As already seen for the TT unit, the values differ very much between the eight different stacking possibilities and the statistical evaluation methods. Thus, only the minimal, maximal and averaged values for each system are summarized here , see Tab. 6.2. The remaining values can be found in Appendix D.

6.5 TRANSFER RATES AND MOBILITIES

So far, the results for the coupling elements and the reorganization energies were discussed separately. Based on these values the transfer rate k can be calculated using the Marcus formula, Eq. (4.12). In the models considered in this work, both sites A and B are the same such that the driving force ΔE vanishes. In Table 6.2, the results for all

Table 6.2: Mean reorganization energy λ, minimal, maximal and RMS of $\sqrt{\langle T_{AB}^2 \rangle_{QB}}$ as obtained for the DPP based DA polymers considering thiophene, TT, 2T and TET as the donor unit. CT rate k and charge carrier mobility μ as obtained from Marcus formula and Einstein relation using $T = 300$K and $d = 3.5$ Å.

donor unit		T		TT		2T		TET	
charge type		hole	electron	hole	electron	hole	electron	hole	electron
λ (meV)		208	179	191	172	176	165	162	163
$\sqrt{\langle T_{AB}^2 \rangle_{QB}}$	min	41.2	51.8	74.6	55.1	63.2	68.6	78.5	59.7
(meV)	RMS	88.0	66.6	96.4	96.3	115	88.7	103	96.3
	max	132	90.3	119	116	135	107	120	123
k	min	0.8	1.9	3.4	2.3	2.9	3.9	5.4	3.1
(10^{13} s^{-1})	average	3.8	3.1	5.6	7.1	9.6	6.6	9.3	8.0
	max	8.6	5.7	8.6	10.3	13.3	9.6	12.4	12.9
μ	min	0.4	0.9	1.6	1.1	1.4	1.9	2.5	1.4
(cm^{2}V^{-1}s^{-1})	average	1.8	1.5	2.7	3.4	4.6	3.1	4.4	3.8
	max	4.1	2.7	4.1	4.9	6.3	4.5	5.9	6.1

considered systems are listed. First, the reorganization energies for hole and electron transfer are given, which were obtained according to Eq. (4.14) by $\lambda_h = \lambda_0^{+1} + \lambda_{+1}^0$ and $\lambda_e = \lambda_{-1}^0 + \lambda_0^{-1}$, respectively. Moreover, the averages over all isomeric structures were taken. In the following rows, the minimal and maximal values as well as the RMS over all eights configurations of $\langle T_{AB}^2 \rangle_{QB}$ are given. Furthermore, the hopping rates and mobilities are given as obtained from the Marcus formula, Eq. (4.12), and the Einstein relation, Eq. (4.8), respectively. For both, a temperature of $T = 300$ K as well as the medium hopping distance $d = 3.5$ Å were used.

The obtained results for the mobility μ are of the same order of magnitude for all systems. The absolute values vary from 0.4 to 6.3 cm^{2}V^{-1}s^{-1} and 0.9 to 6.1 cm^{2}V^{-1}s^{-1}. The highest hole and electron mobilities are obtained for TDPP-2T and TDPP-TET, respectively. Except for TDPP-TT, the average mobilities for holes yields slightly larger values than for electrons.

It shall be noted that these values are about one order of magnitude lower than the ones already observed in experiments. Since the model considers ideal stacks of chains, the values are expected to be larger than the experimental ones. This deviation between calculated and measured values arises from the use of the Einstein model, where an isotropic diffusion is assumed. Since the CT along the chain is of adiabatic nature within the conjugated region, the charge carrier mobility of the anisotropic system obtains larger values. Thus, the presented results provide a lower boundary for ideal stacks rather than an upper one.

Moreover, it should be noted, that the here derived quantities were calculated without explicit consideration of an electric field. Within a transistor device, however, the electric field of the source-drain voltage is the driving force for the electronic current. Typically, these field strengths are small so that they can be neglected. A detailed study of the behavior of the reorganization energy and the coupling element for different field direction was performed in collaboration with A. Förster, see Ref. 178.

Finally, it is noted that for the largest obtained coupling elements, the ratio of λ and T_{AB} exceeds the critical value for the applicability of the Marcus theory. For these cases, a delocalized transport mechanism might be applied, see Refs. 179, 180 and 181.

6.6 SUMMARY AND CONCLUSIONS

In this chapter, the inter-molecular CT between polymers, which consist of TDPP as acceptor unit and different thiophene based compounds as donor units, was investigated. For this, Marcus theory was applied to calculate the hopping rates. The two required quantities, λ and T_{AB}, were calculated using the SCC-DFTB method.

Two kinds of structural properties were discussed in detail: On the one hand, different isomeric conformations of the backbone were considered: *cis* and *trans* configurations of the thiophene units with respect to the DPP unit and to the donor unit. Moreover, two stacking orientations, parallel and antiparallel, were considered. In total eight different stacking variants were studied for each molecular model.

At first, the reorganization energy λ was studied. For this, the monomer models were considered, where the *cis-trans* isomerism remained as the only degree of freedom. It was found that the elongation of the repeat unit, which arises from the variation of the donor part, leads to a decrease of the reorganization energy. This change was much larger for holes than for electrons which matches the fact that the donor unit affects the transport of positive charge carriers more strongly than that of negative ones. Due to the fact, that the acceptor unit was unmodified, λ stayed rather constant when electron transfer is considered.

Second, the coupling T_{AB} was calculated with special focus on the displacement of two π-π stacked chains. Mainly the shift along the polymer backbone was studied. Here, a correlation between the number and position of nodal surfaces of the frontier orbitals and the corresponding values of T_{AB} was observed. These results match the fact that T_{AB} depends on the orientation of the two chains like the overlap between the wave functions of the individual fragments. Furthermore, it was found that several local minima of the interaction energy of two π-π stacked chains exist which are separated by barriers of more than 0.3 eV per interacting unit.

To estimate a single quantity that can enter the Marcus formula, a Boltzmann-type statistical approach to calculate a value $\sqrt{\langle T_{AB}^2 \rangle_{QB}}$ averaging over a large number of stacking alignments was introduced. This approach enabled an investigation of the transport properties for each of the eight groups of orientations separately. The values obtained in this way varied over a broad range. Among all studied systems, the highest hole mobility arose from the TDPP-2T system while the highest electron mobility was found for TDPP-TET. Other orientations of the same system, however, result in much smaller values so that the mean value of all orientations did not produce clear trends.

This leads to the following conclusions. The electronic transport properties are not pronouncedly influenced by the molecular structure, but also by the isomeric conformation and the stacking orientation. Based on this, it is suggested either to target specific molecular configurations—rather than to work with a set of random orientations—or functionalize the donor unit according to other features, but not the transfer rates theoretically derived from a molecular scale. Improved techniques to form long range crystalline structures, chemical and mechanical stability, or effective synthesis routes are of more importance than the designs design of the donor unit.

On the one hand, it might be useful for future investigations to take the solubilizing side-chains into account, since they affect the interaction of adjacent chains to the most extent. As recent investigations show, they cause shifts in y direction [141] resulting in smaller couplings. Thus, it is suggested to design alkyl chains which favor smaller displacements of the polymers perpendicular to the backbone direction. On the other hand, non-parallel orientations should be studied in future. That way, the transfer between chains at boundaries of crystalline areas would be modeled. Studying the properties of this regions might help to explore the importance of gain boundaries for the semiconducting properties of macroscopic films.

7 MOLECULAR P-DOPING OF DONOR-ACCEPTOR POLYMERS

7.1 INTRODUCTION

In order to improve the conductivity of semiconducting materials, it is a well-known approach to increase the available charge carrier density. For this, electron-donating or electron-withdrawing compounds are introduced into the system so that the total number of charge carriers—electrons or holes—is increased [182]. Due to their structural differences, the applied concept to do so varies for conventional bulk semiconductors and semiconducting polymers (SCPs). While in the former case, atoms of the third or of the fifth main group are incorporated in the crystalline structure, electron-rich or electron-deficient molecules are admixed with organic films in latter. Hence, the mechanism of charge transfer (CT) is of different natures [52]. Despite the growth of organic electronics in the past years, there is still a lack of comprehensive understanding of the fundamental processes of molecular doping [56]. Nevertheless, it is a widely used approach in both academia and industry [183].

Due to its recent development, the doping of third generation SCPs is to date poorly investigated. Compared to the first and second generations of SCPs, new challenges have to be faced, e.g. the position of the dopant with respect to the different units. Moreover, donor-acceptor (DA) polymers typically possess low-lying highest occupied molecular orbitals (HOMOs) so that stronger dopant materials are required for high doping efficiencies [184].

Tetrafluoro-tetracyano-quinodimethane (F4-TCNQ), see Fig. 7.1 a), was found to be a good p-dopant and has been studied intensively in the past years. It was demonstrated for example that the conductivity of P3HT can be drastically increased from 10^{-6} Scm^{-1} to 1 Scm^{-1} [185]. Since the lowest unoccupied molecular orbital (LUMO) of F4-TCNQ has a lower energy than the HOMO of polythiophene (PT), the polymer HOMO is depleted

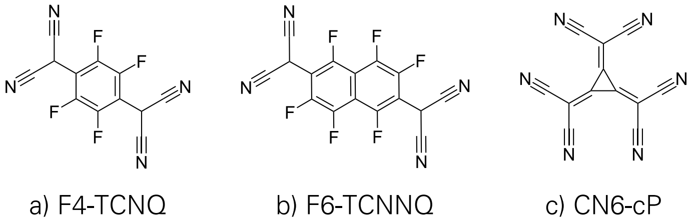
a) F4-TCNQ b) F6-TCNNQ c) CN6-cP

Figure 7.1: Molecular structures of the considered p-dopants.

into the LUMO of the dopant and a hole is created in the SCP [54]. Another commonly used p-dopant is 2,2-(perfluoronaphthalene-2,6-diylidene)dimalononitrile (F6-TCNNQ), see Fig. 7.1 b), which has a larger electron affinity than F4-TCNQ and offers therefore better p-doping properties [186, 187]. F6-TCNNQ was successfully applied for the doping of vacuum-processed hole-conductive materials in OLEDs [188, 189], but the use for the doping of π-conjugated polymers—especially DA copolymers—was not reported so far. An even more powerful dopant is hexacyano-trimethylene-cyclopropane (CN6-cP), see Fig. 7.1 c), the synthesis and electrochemical properties of which were first described in 1976 by Fukunaga [190, 191]. However, its use as a dopant has not been reported in open literature.

One of the first studies on p-doping of DA copolymers was published by D.D. Nuzzo *et al.*, who considered cyclopenta-dithiophene (CPDT) as donor and benzothiadiazole (BT) as acceptor moieties [52]. Indeed, they found that doping with F4-TCNQ leads to conductivities up to 10^{-2} S cm^{-1} being by two orders of magnitude lower than that of conventional F4-TCNQ:P3HT systems. Furthermore, the CT predicted by simulation differed when the dopant was placed next to the donor compared to positioning it above the acceptor. In the former case, a integer CT of 1 e$^-$ was observed, whereas both molecules remained neutral in the latter. In another study [56], an DA polymer was considered which was formed by oligothiophene as donor and tetra-fluorobenzene (TFB) as acceptor. The authors reported similar trends: The CT decreased when the F4-TCNQ was placed close to TFB.

These and other studies, in which the doping efficiency is theoretically investigated, focus on the following properties [52, 192–194]. Mainly, the difference between the polymer HOMO and the dopant LUMO is considered as the driving force for the CT. Furthermore, CT complexes are studied where the HOMO and the LUMO are considered in terms of hybridization of the dopant and the polymer orbitals. The total CT is typically derived from population analyses. These studies, however, do not to report on a systematic basis to what extent the orientation and the position of the dopant with respect to the polymer affects the doping characteristics. Moreover, the energies of different orientations and the interactions, which govern the formation of CT complexes, are only poorly discussed.

In the presented work, the p-doping of P(TDPP-TT) was investigated theoretically. In particular, the properties of F6-TCNNQ and CN6-cP are considered and compared to those of F4-TCNQ. In contrast to previous works, the spatial orientation of the dopant with respect to the polymer and its impact on the doping properties was studied in a systematic way.

7.2 OBSERVATIONS FROM EXPERIMENT

The present work was done in strong collaboration with T. Erdmann and Y. Karpov, who investigated these systems experimentally. Figure 7.2 shows conductivities which they measured when P(TDPP-TT) was mixed with F4-TCNQ, F6-TCNNQ and CN6-cP in different molecular doping ratioss (MDRs) of dopant and repeat unit of the DA polymer. For CN6-cP doped P(TDPP-TT), the obtained films showed conductivities up to 70 Scm^{-1} which is one of the highest conductivities for molecularly doped SCPs soluble in organic solvents [184].

The high conductivity of doped P(TDPP-TT) films implies the generation of charge carriers due to the transfer of electrons from the polymer to the dopant. For monitoring the formation of CT complexes in doped polymers, UV-vis spectroscopy was used [188, 198, 199]. As seen from Fig. 7.3, the addition of CN6-cP to P(TDPP-TT) leads to a bleaching of the absorption bands of the neutral polymer with λ_{max} =350, 750, and 840 nm and to the formation of new broad absorptions in the region of 900-1800 nm and above 2000 nm. Similar transformations in the absorption spectra were reported for P3HT doped by F4-TCNQ [188, 198, 199] and were assigned to the absorption of the charge-transfer complex.

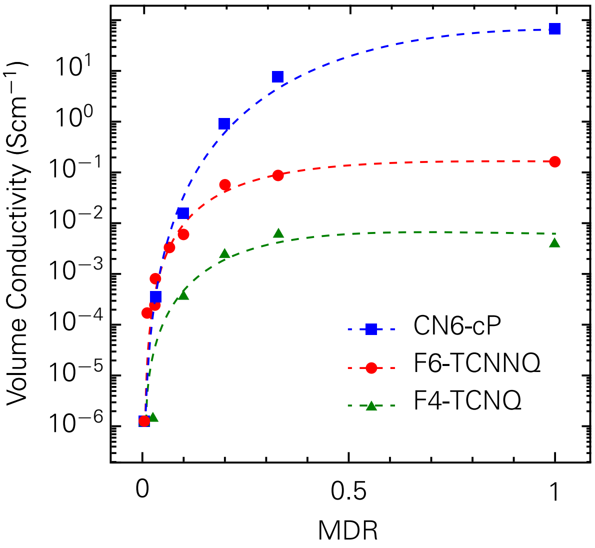

Figure 7.2: Experimentally measured conductivities for P(TDPP-TT) when doped with F4-TCNQ, F6-TCNNQ or CN6-cP in different MDRs of dopant and repeat unit of the DA polymer. Dashed lines are given to guide the eye. For details, see Refs. 184, 195–197.

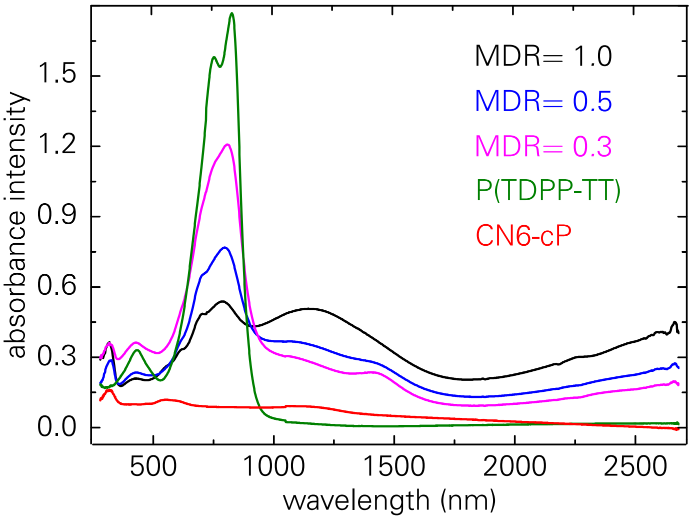

Figure 7.3: UV-vis spectra for P(TDPP-TT) films doped by CN6-cP at different MDRs as well as of the neat P(TDPP-TT) and CN6-cP; redrawn from Ref. 184.

7.3 COMPUTATIONAL DETAILS

To compute these systems by means of quantum chemistry methods, the following simplifications were employed to model P(TDPP-TT): First, as in the previous chapters, methyl groups were substituted for the alkyl side-chains, since they do not contribute to the electronic properties of interest. Second, only finite fragments of TDPP-TT were studied, see Fig. 7.4, rather than a full polymer model using periodic boundary conditions. To ensure a correct modeling of the influence of the adjacent units, the following models were considered: a DPP unit surrounded by two TT units (TT-DPP-TT), a TT unit surrounded by two DPP units (DPP-TT-DPP), and a TDPP-TT dimer. The first and the second were used to study CT complexes where the dopant is positioned above the acceptor or the dopant, respectively. In order to study shifts along the polymer backbone, dimer model was considered for ensuring a continuous transition approaching the boundary of the model.

Density functional theory (DFT) calculations were performed using the SCM ADF 1.3 software package [123, 143, 144]. First, the molecular models were optimized using the PBE functional [78] and a DZ basis. In order to determine the HOMO and LUMO energies of the individual systems, the B3LYP functional was used [77, 142], since it is well accepted for giving HOMO-LUMO gaps with better agreement to experimental data than standard GGA functionals. To study the formation energy and the CT from polymer to dopant, π-π stacks of the DA models and each of the dopants were considered. Here, the PBE functional was employed only since it is still efficient to derive the energy and the charge distribution, but requires less computational resources. For a better control of the structural degrees of freedom, single point calculations were performed for various configurations instead of considering only the optimized cases. To derive the energy of

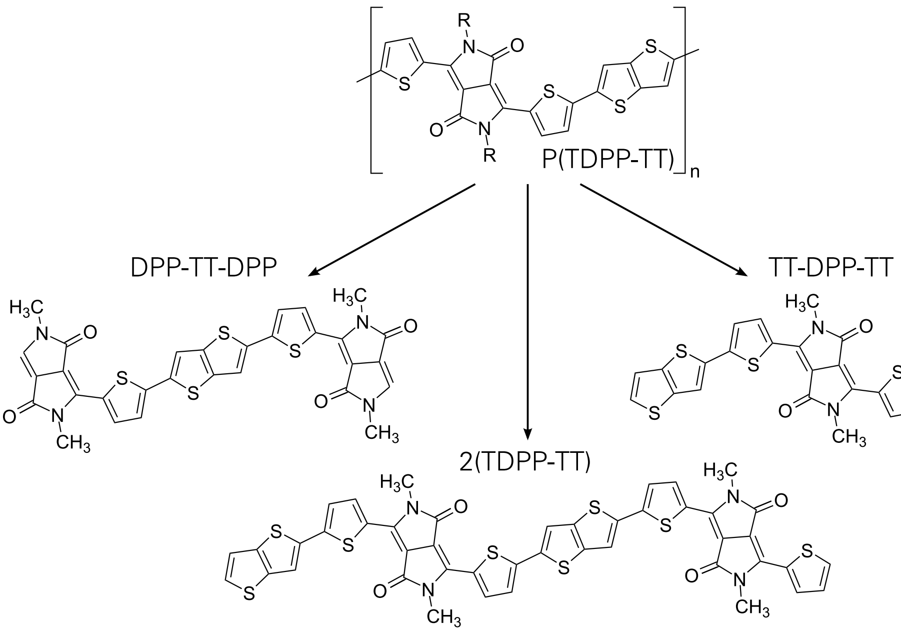

Figure 7.4: Molecular structures of the considered P(TDPP-TT) models.

CT complexes the Grimme dispersion correction was used to include weak interactions such as van-der-Waals interaction [104, 105]. The total CT from the DA polymer to the dopant was calculated based on the atomic charges of each compound as obtained using the Mulliken [80], the Hirshfeld [200], and the Voronoi [82] population analyses. In order to be comparable with available literature, the used software and the working strategy was tested for F4-TCNQ:4T complexes and compared with studies reported in the literature. The obtained results are in reasonable good agreement; for details see Appendix E.

7.4 ISOLATED MODELS

The simplest approach to estimate the doping strength is to compare the energy of the dopant LUMO and the HOMO energy of the semiconducting system obtained by separate calculations. Figure 7.5 shows the molecular orbital (MO) energies of all considered models. Moreover, the HOMO and the LUMO of quatrothiophene (4T) and the TDPP-TT monomer are given for comparison. The considered dopant models F4-TCNQ, F6-TCNNQ and CN6-cP, yield LUMO energies of -6.03 eV, -6.66 eV and -6.76 eV, respectively. Due to the different number of donor and acceptor units in the different P(TDPP-TT) models, the HOMO and LUMO energies vary in the range of -5.96 eV to -5.41 eV and -3.84 eV to -3.50 eV, respectively. As it was already discussed before, see section 5.4.2, the extension of a molecular system results in smaller HOMO-LUMO gaps. Thus, for the polymer case, the position of HOMO can be estimated slightly above the values reported here. Surprisingly, the HOMO found for the 4T model is in the same range as those of the P(TDPP-TT) models. Due to the more electron rich nature of thiophene, the HOMO of PT

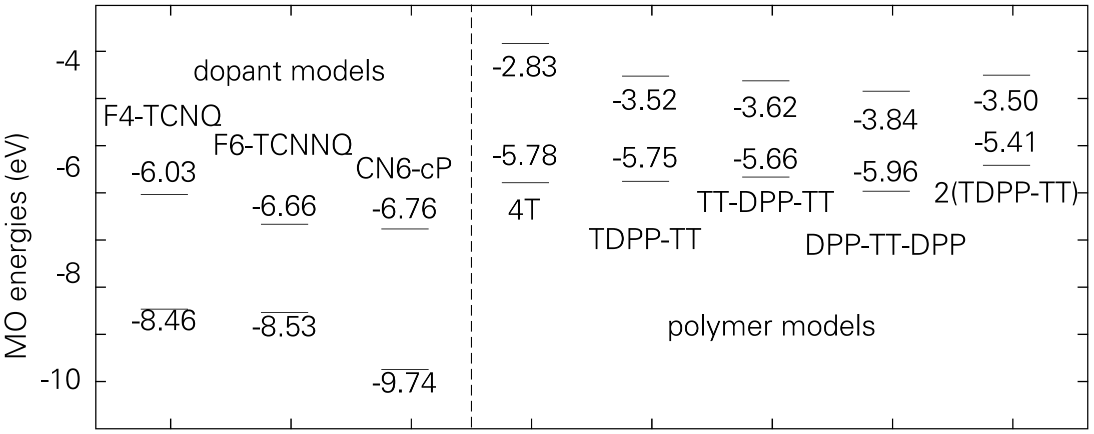

Figure 7.5: Energy level diagram for different p-dopants (left) and polymer models (right) as obtained from B3LYP calculations with DZP basis.

is expected to be higher in energy than that of P(TDPP-TT). It is noted, however, that the end-to-end distance of the 4T model is by 3 Å smaller than that of the TDPP-TT monomer model. Hence, the HOMO of polythiophene will be even higher when increasing the model size. Thus, in this sense, the consideration of 4T as model for P3HT is a much stronger simplification than the TDPP-TT monomer as model for P(TDPP-TT).

Comparing the LUMOs of the dopants to the HOMOs of the P(TDPP-TT) models, the following results were found. In all cases, the dopant LUMOs are lower in energy than the polymer HOMOs. Hence, a CT is expected for all cases. Moreover, the energetic sequence of the dopant LUMOs are in line with the experimentally observed doping strengths derived from Fig. 7.2.

It should also noted, however, that the theoretically obtained HOMO and LUMO values do not fully match experimental measurements. Cyclovoltametry (CV) experiments suggest the LUMOs of F4-TCNQ and F6-TCNNQ to be of -5.24 eV and -5.37 eV, respectively, whereas the HOMO of P(TDPP-TT) is measured as -5.49 eV [184, 195]. Only for CN6-cP, the LUMO with -5.87 eV is found below the HOMO of the DA polymer [184]. Thus, in the picture of the integer CT model, successful p-doping would be expected for CN6-cP only. As depicted in Fig. 7.2, however, conductivity measurements clearly show an increase in σ for all dopant molecules. To what extent solvent induced shifts in the CV measurements cause this mismatch is unclear in the present status.

7.5 CHARGE TRANSFER AND FORMATION ENERGIES

In the following, the CT complexes are discussed where the dopant was placed on top of the TT or the DPP unit. For this, the TT-DPP-TT and DPP-TT-DPP models were considered. First, the stacking distances were varied, which leads to optimal distances in the range of 2.9 Å up to 3.5 Å. When located above DPP-TT-DPP, slightly smaller equilibrium distances were obtained than on top of TT-DPP-TT. The CN6-cP model yielded distances of 2.9 Å up to 3.1 Å, whereas F4-TCNQ and F6-TCNNQ varied between 3.4 Å and 3.5 Å and 3.0 Å and 3.2 Å, respectively.

Second, the dependence on the rotational orientation was considered. The obtained CT and the complex formation energies for the the F6-TCNNQ:DPP-TT-DPP and the F6-TCNNQ:TT-DPP-TT systems are shown in Fig. 7.6 for a stacking distance of 3.0 Å. Focusing on the energy aspects of the F6-TCNNQ:DPP-TT-DPP complex yields the following observations. When the dopant is aligned parallel to the underlying TT unit, $\phi = 0^\circ$, an energy minimum is obtained (complex 1a) whereas for the perpendicular case (complex 1b) the energy graph exhibit a maximum which is of 80 kJmol^{-1} higher, see Fig. 7.6 a). This change in energy is related to the π-π interaction the area of which decreases by rotation from 0° to 90°. For the F6-TCNNQ:TT-DPP-TT complex, Fig. 7.6 b), a similar trend can be seen. Here, however, the maximum is reached when F6-TCNNQ and the DPP unit are in a parallel orientation (complex 2b). Since both F6-TCNNQ and DPP are electron deficient, their parallel alignment is unfavored. Comparing the two energies of complexes 1a and 2a shows that positioning the dopant on to of DPP is by about 20 kJmol^{-1} less stable than on top of TT. Similar results are reported in the literature for F4-TCNQ:P(CPDT-BT) complexes [52]. It is stressed that although this difference is above thermal energy at room temperature such a constellation is likely in reality, since the fabrication of films is typically an out-of-equilibrium process. Moreover, additional

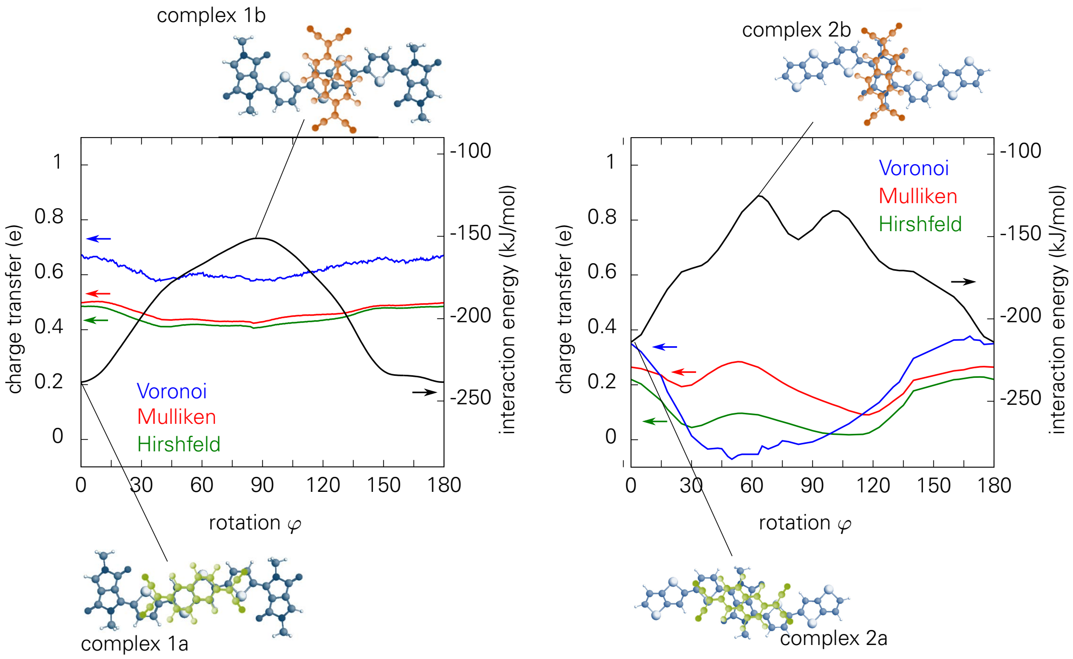

Figure 7.6: charge transfer (left scale) as obtained using Mulliken (red), Hirshfeld (green), Voronoi (blue) population analyses and complex formation energies (black, right scale) when F6-TCNQ is placed on TT (a) or DPP (b) moieties. The molecular planes are parallel and fixed to a distance of 3 Å.

Table 7.1: charge transfer averaged over different rotational orientations when the dopant is positioned above the DPP or the TT moiety.

dopant	position	Mulliken	Hirshfeld	Voronoi
F6-TCNNQ	DPP	0.20 e^-	0.10 e^-	0.11 e^-
CN6-cP		0.35 e^-	0.31 e^-	0.20 e^-
F6-TCNNQ	TT	0.49 e^-	0.48 e^-	0.65 e^-
CN6-cP		0.61 e^-	0.62 e^-	0.70 e^-

polymer chains in the proximity could stabilize the orientation with dopant on top of DPP.

Taking the CT into account as obtained from the Mulliken, the Hirshfeld and the Voronoi population analyses results in the following. For the F6-TCNNQ:DPP-TT-DPP complex, all three approaches show the same trend: The CT decreases slightly for rotations of 45° up to 135° whereas the Voronoi population is by about 0.15 e^- higher than that obtained from the Mulliken and the Hirshfeld analyses. For the F6-TCNNQ:TT-DPP-TT complex, slightly different behaviors are obtained: the Voronoi population vanishes completely for rotations of 30° up to 120°, whereas the Mulliken and the Hirshfeld analyses yield further maxima in the CT for rotations between 45° and 75°. In the corresponding configurations, the cyano groups of dopant model are on top of the methyl groups of DPP. The distance between the out-of-plane hydrogen atoms and the nearest atom of F6-TCNNQ is roughly 2 Å. so that a CT from the methyl group to the cyano group is obtained when considering the Mulliken and the Hirshfeld analyses . It is assumed, that this is rather an artifact of the chosen population analyses than a reliable result.

Table 7.1 summarizes the CT for F6-TCNNQ and CN6-cP dopants when placed on top of TT or DPP, averaged over the rotational orientations with a stacking distance of 3 Å. In both cases, the CT is higher when the dopant models are placed on top of the donor unit. This is in line with the intuitive expectation and former results reported in the literature [52, 56]. In contrast to the studies of F4-TCNQ:P(CPDT-BT) complexes [52], however, a smaller, but yet a non-zero CT was found when the dopant was positioned above the acceptor unit of the polymer. This observation can be related to the spatial extent of the dopant molecule. When the dopant exceeds the DPP unit, an interaction with the thiophenes and consequently a CT might occur. A similar observation was reported for F4-TCNQ:3HT-TFB complexes [56]. Comparing the total CT obtain for the different dopant models reveals larger values for the CN6-cP than for the F6-TCNNQ complexes. This is again in line with the stronger doping properties observed in experiment.

In order to study the CT, when the dopant is shifted along the polymer backbone, the CT complexes were constructed by placing the dopant molecules on top of 2(TDPP-TT) model. That way, the dopant does not approach the terminating units. Figure 7.7 depicts the obtained results for the CN6-cP dopant. The colored curves give the obtained

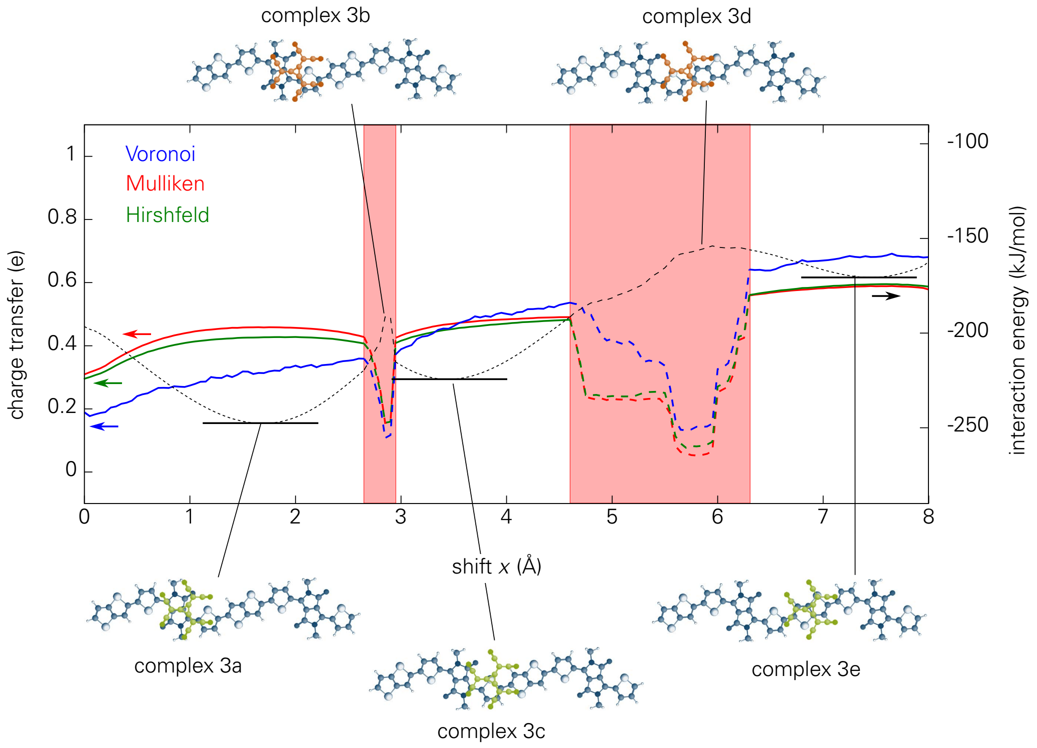

Figure 7.7: Calculated CT and energy for the CT complex CN6-cP:2(TDPP-TT) for a stacking distance of 3 Å. The shift x indicates the relative distance of the centers of masses for two molecules in backbone direction. The colored curves specify the CT obtained by the different population analyses (left scale) while the black one gives the formation energy (right scale). The red shaded areas indicate configurations where convergence issues within the SCF cycles occurred.

CT and the black line the formation energy of the complex. The red marked areas indicate configurations where convergence issues within the SCF cycles occurred. Due to a non-converging density, the SCM ADF software automatically applies a occupation schema which violates the *aufbau* principle [123, 144]. Instead, the electrons are assigned to MOs that are spatially similar to the occupied MOs of the previous cycle. Even though this lead to convergence of the SCF cycles, the LUMO is lower in energy than the HOMO. Thus, these results are not in line with the Hohenberg-Kohn theorems. The orientations for which these problems occur correspond to those where the center of CN6-cP is

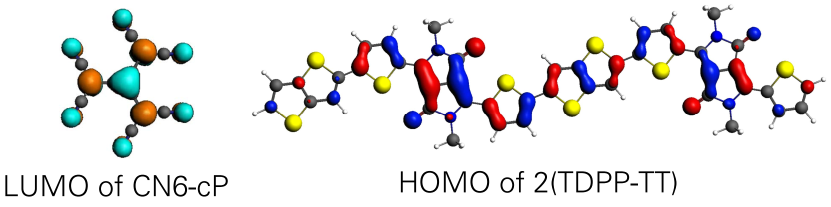

Figure 7.8: Isosurface plot of the LUMO of CN6-cP dopant and the HOMO of 2(TDPP-TT).

located between the units of the polymer model, but not on top of the covalent bond, see complex 3b and 3d. It can be assumed, that the electronic coupling between the two compounds vanishes and the two molecules behave like isolated fragments. Taking the spatial shape of the frontier orbitals into account supports this hypothesis, see Fig. 7.8.

As discussed above, the CT is smaller when the dopant is positioned above the acceptor unit ($x = 0.0$ Å) than on top of the donor unit ($x = 8.0$ Å). The obtained trends are slightly different for the individual population analyses. While Mulliken and Hirshfeld analyses increase already for small shifts and yield almost constant values for $x = 2.0$ Å and for $x = 8.0$ Å, the Voronoi population increases constantly. The calculations result in formation energy gains in range of 150-250 kJmol^{-1} for the different positions of the dopant relative to the polymer. When a simple point charge model is considered, the energy gain originating from electrostatic attractions between the dopant and the polymer model can be estimated. For positioning the dopant above the DPP unit, the CT of 0.2. . . 0.4 e$^-$ yields an electrostatic energy of -40. . . -18 kJ mol^{-1} where on top of the TT unit -226. . . -166 kJ mol^{-1} are obtained for a CT of 0.6. . . 0.7 e$^-$. Hence, the complex with CN6-cP close to the donor unit of the polymer is expected to be more stable. Quite surprisingly, however, the most stable complex is that one with CN6-cP close to the DPP unit, see complex 3a. It is assumed that this stability of the CT complex arises from favorable local interactions between the highly polar groups of DPP and CN6-cP. Such interactions are not present for the complexes 3c and 3e when the donor is positioned on top of the thiophene compounds.

7.6 ELECTRONIC STRUCTURE OF CT COMPLEXES

So far, only the energy and the CT in complexes were considered. In this subsection, the electronic structure of the CT complexes will be discussed in more detail. For this, the focus is on the MO energies and the hybridization character of the frontier orbitals.

Figure 7.9 illustrates the HOMOs and LUMOs for the CN6-cP complexes compared to those of the isolated models. First, the MO energy eigenvalues obtained from B3LYP calculations will be discussed. Comparing the energies of HOMO and LUMO+1, similar differences in energy were obtained as for the HOMO and LUMO of the isolated TT-DPP-TT and DPP-TT-DPP models. Having in mind, that these two P(TDPP-TT) models differ in the number of donor and acceptor units, the different positions of these two levels can be explained. The position of the LUMO level and consequently the HOMO-LUMO gaps, however, differ by more then 0.2 eV. Whereas CN6-cP on top of the acceptor moiety yields a gap of 1.13 eV, the complex with CN6-cP on top of the donor unit shows a much smaller gap of 0.54 eV. Translating this into wave length as a first approximation for HOMO-LUMO transition gives 1400 nm and 2300 nm, respectively. These calculations indicate that one may attribute the experimentally observed absorptions in the UV-vis spectra at 900-1500 nm and above 2000 nm, see Fig. 7.3.

The isosurface plots shown as insets in Fig. 7.9 give a first insight to what extent

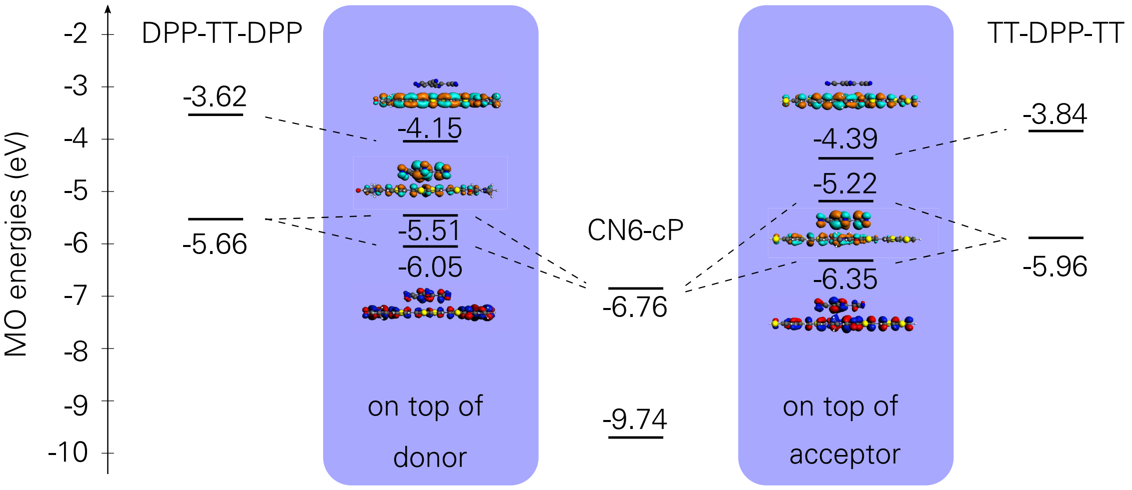

Figure 7.9: MO energy level diagram of the frontier orbitals for CN6-cP and TDPP-TT before and after formation of the CT complex.

the two molecules contribute to the CT complex wave functions. They suggest that for both CT complexes, the HOMO and the LUMO are formed by hybridization of the dopant LUMO and the DA polymer HOMO. This is in line with the simple model, that the HOMO of the polymer is partially depleted and the dopant LUMO is filled. On the contrary, the LUMO+1 is only derived from the polymer LUMO. For a deeper insight, Tab. 7.2 lists the total population for HOMO, LUMO and LUMO+1. It gives the contribution of the individual units of the polymer and the dopant models as obtain from summing up the gross orbital population (GOP) of the constituting atoms. Moreover, the orbital energies and the HOMO-LUMO gap are given. In all cases, the contribution of the dopant models to the LUMO+1 wave function is below 4% and thus negligible. This observation is in line with those found for the F4-TCNQ:4T complexes [56, 185, 192, 193].

For all complexes, the LUMO is mainly formed by the dopant, but the contribution ranges from 68% to 89%. In detail, CN6-cP yields the smallest value for both complexes and hence the largest hybridization with the polymer HOMO. F4-TCNQ and F6-TCNNQ give 87% and 78% when located next to the donor and 76% and 89% on top of the acceptor. This means that the hybridization for F4-TCNQ is slightly larger when located on the acceptor than on top of the donor, whereas the situation is vice versa for F6-TCNNQ. The remaining part of the LUMO is distributed over the polymer model. The relative contributions of the polymer units, however, differ for the different dopant models. For the CN6-cP, the largest contribution is found at the central units—TT or DPP. For F4-TCNQ, the DPP units contribute most in both cases whereas for the F6-TCNNQ complexes the TT units always contribute strongest.

The constitution of the complex HOMOs follows a similar trend as that of the LUMOs: The hybridization is largest for the CN6-cP complexes, whereas F4-TCNQ and F6-TCNNQ behave vice versa. On top of the DPP-TT-DPP model, F4-TCNQ, F6-TCNNQ and CN6-cP yield 1% , 11% and 21% whereas on top of the TT-DPP-TT model the populations are

Table 7.2: Orbital resolved gross orbital population (GOP) and MO energies of LUMO+1, LUMO and HOMO for CT complexes with F4-TCNQ, F6-TCNNQ, or CN6-cP on top of DPP-TT-DPP or TT-DPP-TT fragments.

		dopant:DPP-TT-DPP				dopant:TT-DPP-TT		
		F4-TCNQ	F6-TCNNQ	CN6-cP		F4-TCNQ	F6-TCNNQ	CN6-cP
LUMO+1	ϵ (eV)	**-4.11**	**-4.30**	**-4.15**		**-4.10**	**-3.95**	**-4.39**
	DPP	20%	18%	20%/20%		36%	40%	42%
	T	16%	17%	12%/18%		14%	18%	19%/ 16%
	TT	24%	28%	29%		17%	10%	12%/ 10%
	dopant	4%	2%	1%		2%	4%	1%
LUMO	ϵ (eV)	**-4.88**	**-5.07**	**-5.51**		**-5.56**	**-5.27**	**-5.22**
	DPP	4%	4%	6% /5%		10%	1%	14%
	T	3%	4%	5% /4%		5%	2%	6%/3%
	TT	1%	6%	12%		2%	3%	6%/2%
	dopant	87%	78%	68%		76%	89%	69%
HOMO	ϵ (eV)	**-6.08**	**-6.22**	**-6.05**		**-6.00**	**-5.89**	**-6.35**
	DPP	29%	34%	24%/36%		30%	40%	28%
	T	11%	7%	5%/ 8%		12%	15%	8% /15%
	TT	19%	7%	6%		14%	14%	7%/ 15%
	dopant	1%	11%	21%		18%	2%	27%
gap (eV)		**1.2**	**1.15**	**0.54**		**0.46**	**0.72**	**1.13**

18%, 2% and 27%, respectively.

Considering the symmetry aspects of the isolated models leads to the following conclusion. Effect of the hybridization and consequently the CT related to the HOMO of the complex is related to the irreducible representations to which the MOs belong, see Fig. 7.10. Both P(TDPP-TT) models as well as F6-TCNNQ have the point group C_{2h}. F4-TCNQ has D_{2h} and is therefore of higher symmetry. The LUMO of F4-TCNQ is of B_{2g} character and thus exhibits a nodal plane through the center of the model. The LUMO of F6-TCNNQ is of A_u type and has consequently a wave function maximum at its center. Placing these dopants on top of the TT-DPP-TT, whose HOMO is of A_g character, the overlap with F6-TCNNQ LUMO vanishes, whereas it yields a non-zero value when F4-TCNQ is chosen as dopant. Thus, the hybridization is forbidden for the one and

LUMO of dopant models:

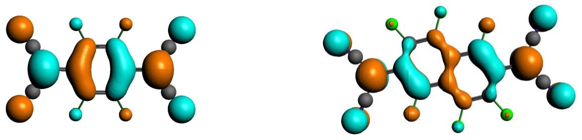

F4-TCNQ: B_{2g} F6-TCNNQ: A_u

HOMO of polymer models:

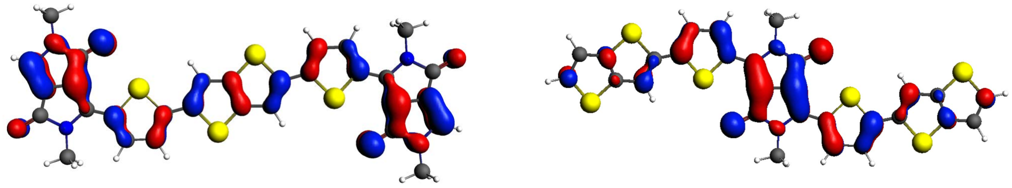

DPP-TT-DPP: A_u TT-DPP-TT: A_g

Figure 7.10: Isosurface plots and irreproducible representation of LUMO of F4-TCNQ and F6-TCNNQ and HOMO of P(TDPP-TT) models.

enabled for the other. Since the HOMO of the DPP-TT-DPP model is of A_u, the situation changes, when the dopant is on top of the donor unit: The overlap with the F4-TCNQ LUMO vanishes and that with F6-TCNNQ LUMO does not. Hence, the hybridization is possible for F6-TCNNQ but not for F4-TCNQ. The partial population of the complex LUMO at the polymer is not due to the hybridization with the polymer HOMO, but with HOMO-1.

The overlap of two MOs is not only depending on individual symmetries but also on the relative orientation of the two molecules. To investigate the hybridization of the complex orbitals for different alignments, the CT complex of F6-TCNNQ on top of DPP or TT was considered when rotating the models around the stacking axis. Figure 7.11 shows, how the MO energies and the population of HOMO, LUMO and LUMO+1 depend on the rotational angle φ. When the F6-TCNNQ is placed on the DPP unit, both the MO energies and the population of the wave functions vary only slightly. The HOMO-LUMO gap exhibits values from 0.5 up to 0.8 eV and the individual contributions of the units to the complex orbitals remain as discussed above. On top of the TT unit, however, the rotational orientation has impact on both hybridization and HOMO-LUMO gap. For 0°, when the dopant and the polymer are aligned, the overlap between dopant LUMO and the polymer HOMO is maximal and hence the hybridization is largest. When the dopant is rotated, this overlap decreases, which leads to reduced hybridization and the CT from polymer HOMO to polymer LUMO vanishes. Since the total CT remains finite, see Fig. 7.6, it can be concluded that it is not only caused by hybridization of the frontier orbitals, but also involves MOs which are deeper in energy. Simultaneously, the HOMO-LUMO gap diminishes from 1.2 eV to 0.5 eV. Having a closer look to the individual units of the polymer model, it is observed that only the populations of the central units—TT and T—increase.

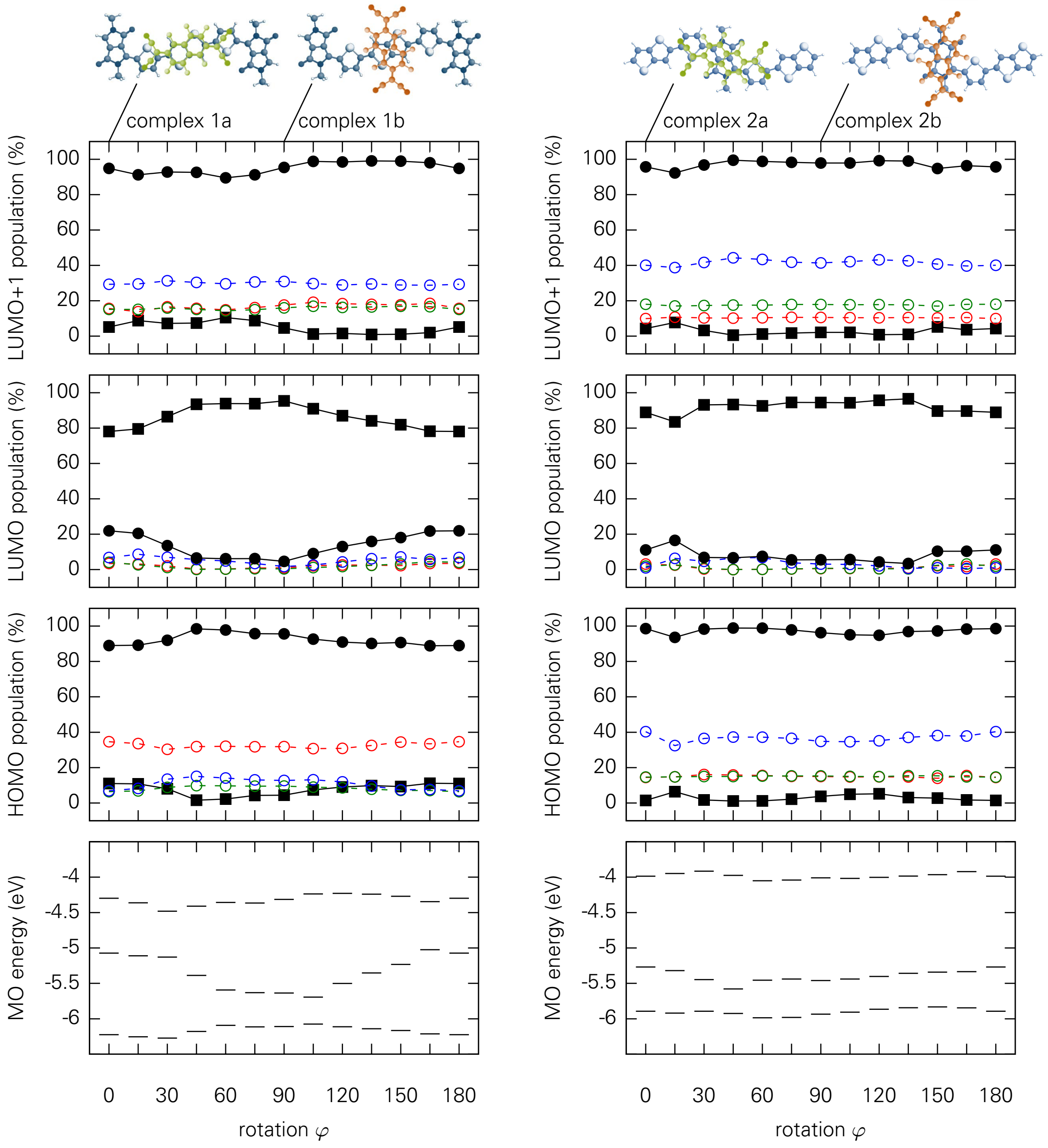

Figure 7.11: Energy level diagram (bottom) and wave function populations for HOMO (lower central), LUMO (upper central) and LUMO+1 (top) of F6-TCNNQ on top of TT (left) and DPP (right) units in dependency on the rotational orientation. For the populations filled squared and filled circles (•) indicate the contribution from dopant and polymer models, respectively. Empty circles relate to the individual contributions of DPP (red), thiophene (green) and TT (blue) units.

This supports the assumption that the CT is a localized effect which is approximately limited to the spatially extent of the dopant. Since the populations at the DPP units remain constant, it is concluded that away from the complex region the wave functions are not influenced by the CT process. In particular, a localization of the orbital due to the presence of the dopant is not found. A similar conclusion was drawn from infra-red (IR) experiments as reported in Ref. 56.

Last, the population of complex LUMO+1 is considered. In both cases, dopant on

DPP or on TT units, the wave functions are distributed over the whole polymer model and the strongest contribution arises from the TT units. Note that this observation is in line with the results reported in section 5.4. The relative contributions of the subunits of the polymer model remain as discussed for the LUMO of the isolated chain.

Finally, it shall be remarked that the Kohn-Sham wave functions, which are discussed when the electronic structure is derived from DFT approaches, belong to an auxiliary system of non-interacting electrons. Thus, the HOMO and LUMO of the complex should not directly be translated into a single particle picture of electrons.

7.7 SUMMARY AND CONCLUSIONS

In this chapter, the doping properties of F4-TCNQ, F6-TCNNQ and CN6-cP with P(TDPP-TT) models were studied by means of DFT simulations. For this, the HOMO and LUMO levels of the isolated models were considered, as well as the CT from the polymer to the dopant for different CT complex orientations. Moreover, the electronic structure was evaluated, where the focus was on the hybridization character of HOMO, LUMO and LUMO+1. Additionally, the impact of the symmetry aspects of the dopant and polymer were investigated.

As a result, evidence for the doping strength as observed in conductance measurements was found. As such, the positioning of the dopant LUMOs above the polymer HOMO gave first indications for the doping effects for all models. When comparing the LUMO of the different dopants, the energy sequence was in line with that of the maximal observed conductance: F6-TCNNQ shows better p-doping properties than F4-TCNQ and CN6-cP being the most efficient p-dopant. Moreover, the CT obtained from charge population analyses yields a higher doping strength for CN6-cP than for F6-TCNNQ. In fact, a CT from F6-TCNNQ to the polymer was only observed when it was overlapping with the donor unit. When it was positioned above the acceptor moiety of the polymer the CT vanished. For CN6-cP, the CT remained even when the dopant was located close to the DPP unit. It is therefore concluded that the electron affinity of CN6-cP is superior to that of the commercially available p-dopants F4-TCNQ and F6-TCNNQ.

Moreover, the effect of the position of the dopant on the HOMO and LUMO wave functions of the complex was studied. It was found, that the hybridization is mainly driven by symmetry rather than by the doping strength of the models. The three-fold axis of CN6-cP is therefore superior to the two-fold F4-TCNQ and F6-TCNNQ, because the CT is less dependent of the rotational orientation. Thus, it is concluded that the symmetry aspect should be taken into account when designing molecular dopant molecules. It was furthermore found that the total transfer in the complexes does not only originate from transfer from the polymer HOMO into the LUMO of the dopant, but also from MOs which are deeper in energy.

It is noted, that at the present status it is unclear, to what extent the here considered CT complex occur within real polymer films. The formations of absorptions band in

UV-vis spectra with wave length higher than those of pristine polymer is interpreted as formation of CT complexes. The effect of dopant molecules entangled within the space of the side-chains, however, was not considered yet. Although an interaction between the electronic structures of polymer and dopant is rather unlikely in such a situation, the CT can take place in solution before fabricating the polymer films. At the present status, it is unknown whether the CT process only occurs after the film is formed or if the doping might already happen in the solvent phase. Thus, it is suggested to consider non-π-π stacked orientations of dopant and polymer in further studies.

Part IV

Summary

8 CONCLUSIONS AND FUTURE PROSPECTIVES

8.1 OVERVIEW

The research presented in this thesis dealt with semiconducting polymers (SCPs) since they are evolving into fundamental components for the next generation of electronic devices [1–6]. In particular, it focused on donor-acceptor (DA) copolymers formed by the electron-deficient diketopyrrolo[3,4-c]pyrrole (DPP) as acceptor moiety and different electron-rich thiophene compounds as donor unit. This novel type of SCPs has received a lot of attention due to experimental reports on their very good electronic properties which enabled record values for field-effect transistor applications [49–51]. In order to get a more profound understanding of the structural and electronic properties, the main objective of this work was to study the electronic structure of these novel materials. For this aim, density functional theory (DFT) methods were used since they are efficient tools to consider molecular systems, even those with partially complex structure.

The investigations reported in this work were divided into three parts. In the first one, a comparative study of the structural and the electronic properties of small models and short oligomer chain was performed at different levels of theory. Here, the focus was on evaluating the applicability of the density functional based tight binding (DFTB) method, which is computationally very efficient, but requires well-tested parameter sets. In the second part, the electron transfer between π-π stacked DA polymer chains was studied by means of the Marcus transfer theory. For this purpose, an efficient strategy was developed and implemented to handle the complex chemical structure and the large configuration space. In course of this, the fragment approach was used which allows a decomposition of the semi-crystalline system into models of isolated chain pairs. Moreover, a Boltzmann-type statistical approach was introduced in order to average over different stacking orientations of two chains. In the third and last part, the p-doping of poly[3,6-(dithiophene-2-yl)-diketopyrrolo[3,4-c]pyrrole-thieno[3,2-b]thiophene] (P(TDPP-TT)) was considered as a case study of DA polymers. Here, the impact of the spatial orientation of the dopant molecules with respect to the polymer was studied and the charge transfer from the polymer to the dopant was evaluated.

8.2 CONCLUSIONS

8.2.1 Geometry and Electronic Structure of Monomer and Oligomer Models

The investigation of structural properties was done for small model systems motived by the compounds of TDPP-based DA polymers. The following observations were made: (i) The interaction of nearest and next-nearest atoms is described equally well by all considered methods. The respective values of the bond lengths and the bond angles were found to be in good agreement with each other and with literature values. (ii) Dihedral angles and the energetic sequence of stable configurations, however, exhibited different trends. DFTB suggested planar orientations for all considered models, whereas DFT with different exchange-correlation functionals yielded partially twisted structures. This non-planarity, however, disappeared when π-π stacked chains are considered. Thus, the use of DFTB with standard parameter values is sufficient to describe polymers within a crystalline phase. (iii) By analyzing scanning tunnel microscopy (STM) images, it was found that different orientations of successive units are present in real systems. Hence, it is suggested to study whether or not a property is sensitive to the internal degrees of freedom before drawing conclusions from only one isomer.

The results obtained when considering the electronic structures were as follows: (i) The molecular orbital (MO) energies obtained by means of different computational approaches differ only slightly. In particular, DFTB and DFT with local density approximation (LDA) or generalized gradient approximation (GGA) functionals yielded gaps between the highest occupied molecular orbital (HOMO) and lowest unoccupied molecular orbital (LUMO) which are of about 1 eV smaller than those obtained from DFT with hybrid functionals. (ii) Considering the atomic contributions to the frontier orbitals, remarkably good agreements between the results of all methods were found. Hence, the use of DFTB is justified for transport model which are based on the electronic structure. (iii) By analyzing to what extent the individual units contribute to the frontier orbitals, it was found that DPP-based polymers behave differently than other DA polymer systems. Instead of partially localized frontier orbitals, where the HOMO and the LUMO are mostly determined by the donor and the acceptor units, respectively, both wave functions are delocalized over the whole polymer models. Remarkably, the DPP unit showed a stronger contribution to the HOMO than to the LUMO although it is considered the acceptor moiety of the DA polymer.

8.2.2 Inter-molecular Charge Transfer between Donor-Acceptor Polymers

Inter-molecular Charge Transfer between Donor-Acceptor Polymers

In order to calculate the rate at which an electron is transferred from a chain to an adjacent one, the Marcus transfer theory can be employed. For this aim, the reorganization energy and the coupling element have to be evaluated.

For the former quantity, monomers of DPP-based DA polymers were modeled considering different thiophene compounds as donor unit. Here, two dependencies related to the end-to-end distance of the molecule were found: One is related to the isomeric degree of freedom and the other originates from the length of the donor part. In particular, the elongation led to a decrease of the reorganization energy. This effect was found to be stronger for positive than for negative charges which matches the fact that the donor unit affects the transport of holes more strongly than of that of electrons.

For the electric coupling, various stacking orientations of two chains were studies. In addition to the isomeric degree of freedom, parallel and antiparallel alignments were considered. For all of these orientations, shifts along and perpendicular to the polymer backbone as well as variations in the π-π stacking distance were studied. In this way, several local minima in the energy landscape of two aligned chains were found. The barriers in between are partially higher than 0.3 eV per interacting unit. In order to enables a qualitative comparison of the different isomers and the different donor units, characteristic value for the coupling element is needed. For this purpose, a Boltzmann-type statistical approach was introduced which averages over all considered orientations of the two chains. Due to the wide range over which the obtained values vary, it is concluded that the electronic transport properties are not pronouncedly influenced by the molecular structure but also by the isomeric conformation and the stacking orientation. Therefore, it is currently suggested to optimize the donor unit with focus on other properties, but not according to theoretically derived transfer rates; Improved techniques to form long-range crystalline structures, chemical and mechanical stability, or effective synthesis routes are of more importance than the molecular design of the donor unit.

8.2.3 Molecular p-Doping of Donor-Acceptor Polymers

In order to investigate the molecular doping of DPP based DA polymers, three molecular dopants were considered: the commercially available F4-TCNQ and F6-TCNNQ as well as CN6-cP; The p-doping properties of the last one were studied theoretically for the first time in this work. The comparison of the LUMO of the dopant models to the HOMO of the DA polymer models explained the experimentally observed doping strength: F4-TCNQ shows worse p-doping properties than F6-TCNNQ while the new CN6-cP is the most efficient. Furthermore, in this work, the charge transfer from polymer to dopant was studied by considering charge transfer (CT) complexes. When the dopants were placed on top of the DPP unit, smaller CT values were obtained compared to positioning it on top of the donor unit. Moreover, the CT was found to be largest for CN6-cP; again in agreement with the experimentally observed doping strength. Because of these results, it is concluded that the electron affinity of CN6-cP is much higher than that of the commercially available p-dopants F4-TCNQ and F6-TCNNQ.

The investigation of the CT complex orbitals in this work showed that the hybridization is mainly driven by symmetry features and not by the doping strength of the dopants. Thus, symmetry aspect may be important for the design of new molecular dopant molecules. Furthermore, it was found that the CT does not only originate from depleting the polymer HOMO into the dopant LUMO—as it is discussed in several publications—but also from MOs which are deeper in energy.

8.3 OUTLOOK

In this thesis, both structural and electronic properties were calculated by means of ground-state *first principles* methods. For soft materials at room-temperature, however, many out-of-equilibrium structures play more important roles than the few optimal orientations. Thus, in future studies it may be interesting to combine empirical force-field methods with calculations of the electronic structure. That way, the arrangement of the atoms can be obtained from molecular dynamic (MD) simulations. Then, by dividing the system into molecular pairs between which CT takes place, one can be calculate the electronic coupling by means of electronic structure methods focusing on these pairs only. Finally, based on the obtained rates, the master equation or kinetic Monte Carlo algorithms should yield a better description of the transport than using the simple Einstein diffusion model.

Using this approach, it should be possible to deduce structures which are more similar to those of real systems than the optimal configurations derived from small models. For example, morphology and environmental conditions can be taken into account. Especially, the impact of the solubilizing side-chains on the orientation of adjacent chains can be included. Moreover, impurities which originate from synthesis or fabrication processes can be incorporated in such simulation. Furthermore, the stability of CT complexes under an applied electrical field can be studied by adding dopant molecules to the system.

Due to the division into many molecular pairs, for which the electronic couplings are calculated, the overall electronic transport is automatically averaged over a large number of CT orientations. In this approach, the MD simulation automatically ensures that the found structures matter compared to the real systems. The consideration of models consisting of many polymer chains also involves long-range interactions in the sampling of the energy landscape. Hence, the finally obtained transfer rates should have a higher reliability than the data determined by only weighting given orientations according to local interactions.

A working scheme as described above is implemented in the software package

VOTCA-CTP [201–203]. It focuses on the analysis of molecular dynamics data, the development of systematic coarse-graining techniques, and efficient methods used for simulating microscopic charge (and exciton) transport in disordered semiconductors. It was originally developed at the Max Planck Institute for Polymer Research and is now maintained also at Los Alamos National Laboratory, Eindhoven University of Technology, and the Beckman Institute for Advanced Science and Technology incorporating contributions from researchers worldwide [203]. So far, the calculation of the coupling element is implemented either using standard DFTcalculations or semi-empirical methods. As it was shown in this thesis and in benchmark studies before [126, 127], DFTB determines the electronic structure and thus the electronic coupling with similar accuracy as DFT with the B3LYP functional. Thus, due to its high computational efficiency it is suggested to use DFTB in this package. It promises a great acceleration of the simulation without significant loss of accuracy.

Part V

Appendix

A DERIVATION OF THE MARCUS FORMULA

A.1 ONE-DIMENSIONAL REACTION COORDINATE

In Section 4.3.2, the Marcus formula was introduced starting from Fermi's Golden rule, see Eq. (4.9). Therein, the canonical partition function $f(q)$, Eq. (4.11), and the harmonic potential, Eq. (4.10), are considered. At first, the case of an one dimensional reaction coordinate $\vec{R} \to q$ is considered. In this case, the δ-distribution fulfills the following equation

$$\delta(g(x)) = \sum \left[\left. \frac{\partial g}{\partial x} \right|_{x_i^*} \right]^{-1} \delta(x - x^*) \tag{A.1}$$

where x_i^* are the roots of $g(x)$. Applying this to Eq. (4.10) one finds

$$\begin{aligned} E^\mu(q) - E^\nu(q) &= E^\mu(q^\mu) - E^\nu(q^\nu) + \frac{\omega^2}{2}((q - q_\mu)^2 - (q - q_\nu)^2) \\ &= \Delta E + \frac{\omega^2}{2}(q^2 - 2qq_\mu + q_\mu^2 - q^2 + 2qq_\nu - q_\nu^2) \\ &= \Delta E - \omega^2 q(q_\mu - q_\nu) - \frac{\omega^2}{2}(q_\mu^2 - q_\nu^2) \\ &\overset{!}{=} 0 \end{aligned} \tag{A.2}$$

and thus

$$q^* = \frac{\frac{\omega^2}{2}(q_\mu^2 - q_\nu^2) - \Delta E}{\omega^2(q_\mu - q_\nu)} \, . \tag{A.3}$$

Inserting this to Eq. (4.9) the transfer rate yields

$$\begin{aligned}
k_{\mu\nu} &= \frac{2\pi}{\hbar}\left[\left.\frac{\partial(E^{\mu}-E^{\nu})}{\partial q}\right|_{q^*}\right]^{-1}\int f(q)\left|\langle\mu|\,\widehat{H}'(q)\,|\nu\rangle\right|^2\delta(q-q^*)\mathrm{d}q \\
&= \frac{2\pi}{\hbar}\frac{1}{\omega^2(q^*-q_\mu)-\omega^2(q^*-q_\nu)}f(q^*)\left|\langle\mu|\,\widehat{H}'(q^*)\,|\nu\rangle\right|^2 \\
&= \frac{2\pi}{\hbar}\frac{1}{\omega^2(q_\nu-q_\mu)}\frac{1}{Z}\exp\left(-\frac{E(q^*)}{k_BT}\right)\left|\langle\mu|\,\widehat{H}'(q^*)\,|\nu\rangle\right|^2 \\
&= \frac{2\pi}{\hbar}\frac{1}{\sqrt{\omega^4(q_\nu-q_\mu)^2}}\frac{\left|\langle\mu|\,\widehat{H}'(q^*)\,|\nu\rangle\right|^2}{K\sqrt{\frac{2\pi k_BT}{\omega^2}}}\underbrace{\exp\left(-\frac{E_\mu^{(0)}}{k_BT}\right)}_{=K}\exp\left(-\frac{\omega^2(q^*-q_\mu)^2}{2k_BT}\right) \\
&= \frac{\left|\langle\mu|\,\widehat{H}'(q^*)\,|\nu\rangle\right|^2}{\hbar}\sqrt{\frac{2\pi}{\omega^2(q_\nu-q_\mu)^2k_BT}}\exp\left(-\frac{\omega^2(q^*-q_\mu)^2}{2k_BT}\right)\ . \qquad \text{(A.4)}
\end{aligned}$$

Substituting Eq. (A.3) for q^* and defining

$$\lambda = \frac{\omega^2}{2}\left(q_\mu - q_\nu\right)^2 = E^{\nu}(q^{\mu}) - E^{\nu}(q^{\nu}) \qquad \text{(A.5)}$$

gives

$$\begin{aligned}
& \frac{\omega^2(q^*-q_\mu)^2}{2k_BT} \\
=\ & \frac{\omega^2\left(\frac{\frac{\omega^2}{2}(q_\mu^2-q_\nu^2)-\Delta E}{\omega^2(q_\mu-q_\nu)}-q_\mu\right)^2}{2k_BT} \\
=\ & \frac{\omega^2\left(\frac{\omega^2}{2}(q_\mu^2-q_\nu^2)-\Delta E-q_\mu\omega^2(q_\mu-q_\nu)\right)^2}{2k_BT\omega^4(q_\mu-q_\nu)^2} \\
=\ & \frac{\left(\frac{\omega^2}{2}(q_\mu-q_\nu)(q_\mu+q_\nu)-q_\mu\omega^2(q_\mu-q_\nu)-\Delta E\right)^2}{4k_BT\lambda} \\
=\ & \frac{\left(\frac{\omega^2}{2}(q_\mu-q_\nu)(q_\mu+q_\nu-2q_\mu)-\Delta E\right)^2}{4k_BT\lambda} \\
=\ & \frac{(-\lambda-\Delta E)^2}{4k_BT\lambda} = \frac{(\Delta E+\lambda)^2}{4k_BT\lambda}\ . \qquad \text{(A.6)}
\end{aligned}$$

Finally, the transfer rate is found,

$$k_{\mu\nu} = \frac{|T_{\mu\nu}|^2}{\hbar}\sqrt{\frac{\pi}{\lambda k_BT}}\exp\left(-\frac{(\Delta E+\lambda)^2}{4\lambda k_BT}\right) \qquad \text{(A.7)}$$

with

$$T_{\mu\nu} = \langle\mu|\,\widehat{H}'(q^*)\,|\nu\rangle\ . \qquad \text{(A.8)}$$

A.2 MULTI-DIMENSIONAL REACTION COORDINATE

For the multi-dimensional case, the coupling element $\langle\mu|\, H'(\vec{R})\,|\nu\rangle$ has to be evaluated for each $\vec{R}^*$ of the hyper-surface that is defined by $E^\mu(\vec{R}^*) = E^\nu(\vec{R}^*)$. Neglecting the dependency of the electronic coupling element on the reaction coordinate (Condon approximation), allows to separate $T_{\mu\nu}$ from the integral.

First, the partition sum Z is considered. Due to the sum of quadratic functions, the exponential function in the integral can be separated into a product of Gaussian functions for which the integral can be solved. One finds

$$\begin{aligned} Z &= \int \exp\left[-\frac{E(\vec{R})}{k_BT}\right] \mathrm{d}^{3N_n}R = \int \underbrace{\exp\left[-\frac{E^\mu(\vec{R}^\mu)}{k_BT}\right]}_{=:K} \exp\left[-\frac{\sum_\xi \frac{\omega_\xi^2}{2}(R_\xi - R_\xi^\mu)^2}{k_BT}\right] \mathrm{d}^{3N_n}R_\xi \\ &= K\left(\prod_\xi \int \exp\left[-\frac{\omega_\xi^2}{2}\frac{(R_\xi - R_\xi^\mu)^2}{k_BT}\right] \mathrm{d}R_\xi\right) = K\left(\prod_\xi \sqrt{\frac{2\pi k_BT}{\omega_\xi^2}}\right). \end{aligned} \tag{A.9}$$

The remaining expression can be solved by tackle the δ-distribution by its respective Fourier integral,

$$\delta(g(\vec{R})) = \frac{1}{2\pi\hbar}\int \exp\left(\frac{\mathrm{i}t}{\hbar}g(\vec{R})\right)\mathrm{d}t\,. \tag{A.10}$$

Hence, Eq. (4.9) can be written as

$$k_{\mu\nu} = \frac{T_{\mu\nu}^2}{\hbar^2}\frac{1}{Z}\iint \exp\left[-\frac{E(\vec{R})}{k_BT}\right]\exp\left[\frac{\mathrm{i}t}{\hbar}\left(E^\mu(\vec{R}) - E^\nu(\vec{R})\right)\right]\mathrm{d}^{3N_n}R\mathrm{d}t\,. \tag{A.11}$$

Inserting the harmonic potential yield the following expression

$$\begin{aligned} k_{\mu\nu} &= \frac{T_{\mu\nu}^2}{\hbar^2}\frac{1}{Z}\iint \underbrace{\exp\left[-\frac{E^\mu(\vec{R}^\mu)}{k_BT}\right]}_{=:K}\exp\left[-\frac{\sum_\xi \frac{\omega_\xi^2}{2}(R_\xi - R_\xi^\mu)^2}{k_BT}\right] \\ &\quad\times\exp\left[\frac{\mathrm{i}t}{\hbar}\left(\underbrace{E^\mu(\vec{R}^\mu) - E^\nu(\vec{R}^\nu)}_{=\Delta E} + \sum_\xi \frac{\omega_\xi^2}{2}\left((R_\xi - R_\xi^\mu)^2 - (R_\xi - R_\xi^\nu)^2\right)\right)\right]\mathrm{d}^{3N_n}R_\xi\mathrm{d}t \end{aligned} \tag{A.12}$$

Note, that in Eq. (A.12), $\vec{R}$ is given in the representation of normal coordinates. Now, the integration over the coordinates R_ξ are performed. Again, the expressions in the multi-dimensional integral can be separated into a product one dimensional integrals and can be solved because of the Gaussian form.

$$\begin{aligned}
&\int \exp\left[-\frac{\omega_\xi^2}{2}\left(\frac{(R_\xi - R_\xi^\mu)^2}{k_B T} - \frac{\mathrm{i}t}{\hbar}\left((R_\xi - R_\xi^\mu)^2 - (R_\xi - R_\xi^\nu)^2\right)\right)\right] \mathrm{d}R_\xi \\
=\ & \int \exp\left[-\frac{\omega_\xi^2}{2}\left(\frac{x^2}{k_B T} - \frac{\mathrm{i}t}{\hbar}\left(2x(R_\xi^\nu - R_\xi^\mu) - (R_\xi^\nu - R_\xi^\mu)^2\right)\right)\right] \mathrm{d}x \quad \text{with} \quad x = R_\xi - R_\xi^\mu \\
=\ & \exp\left[\left(-\frac{t^2 k_B T}{\hbar^2} + \frac{\mathrm{i}t}{\hbar}\right)\frac{\omega_\xi^2}{2}(R_\xi^\nu - R_\xi^\mu)^2\right] \underbrace{\int \exp\left[-\frac{\omega_\xi^2}{2k_B T}\left(x - \frac{\mathrm{i}t k_B T(R_\xi^\nu - R_\xi^\mu)}{\hbar}\right)^2\right] \mathrm{d}x}_{=\sqrt{\frac{2\pi k_B T}{\omega_\xi^2}}}\ .
\end{aligned} \tag{A.13}$$

With this and the definition of the reorganization energy, Eq. (4.14), Equation (A.12) becomes

$$\begin{aligned}
k_{\mu\nu} &= \frac{T_{\mu\nu}^2}{\hbar^2}\frac{1}{Z}\underbrace{K\left(\prod_\xi \sqrt{\frac{2\pi k_B T}{\omega_\xi^2}}\right)}_{=Z} \int \exp\left[-\frac{t^2 k_B T}{\hbar^2}\lambda + \frac{\mathrm{i}t}{\hbar}(\lambda + \Delta E)\right] \mathrm{d}t \\
&= \frac{T_{\mu\nu}^2}{\hbar^2}\int \exp\left[-\frac{k_B T\lambda}{\hbar^2}\left(\underbrace{t^2 + \frac{\mathrm{i}\hbar(\lambda + \Delta E)}{k_B T\lambda}t - \frac{\hbar^2(\lambda + \Delta E)^2}{4k_B^2 T^2\lambda^2}}_{=\left(t - \frac{\mathrm{i}\hbar(\lambda + \Delta E)}{2k_B T\lambda}\right)^2} + \frac{\hbar^2(\lambda + \Delta E)^2}{4k_B^2 T^2\lambda^2}\right)\right] \mathrm{d}t \\
&= \frac{T_{\mu\nu}^2}{\hbar}\sqrt{\frac{\pi}{k_B T\lambda}}\exp\left[-\frac{(\lambda + \Delta E)^2}{4k_B T\lambda}\right]\ .
\end{aligned} \tag{A.14}$$

B SIMPLE ONE-DIMENSIONAL QUANTUM WELL MODEL

In a very simple picture, the electronic structure of aromatic units can be compared to the model of a particle in a box. Many properties, such as the qualitative trend when the model size is increased or when different systems are combined, can be described with this simple picture. For instance, a well ordered conjugated polymer can be considered as a quasi-one-dimensional (1D) system since two directions (y and z) are confined. Hence, the simplest way to study the electronic properties of such a system, is to consider a 1D potential structure which is composed of segments of constant potential energy.

$$V(x) = \begin{cases} V_{left} & x < x_0 \\ V_1 & x_0 \leq x < x_1 \\ V_2 & x_1 \leq x < x_2 \\ \vdots & \\ V_n & x_{n-1} \leq x < x_n \\ V_{right} & x_n \leq x \end{cases} \tag{B.1}$$

For such a model, the corresponding Schrödinger equation can be solved analytically within each region of constant potential ,$x_{i-1} \leq x < x_i$:

$$\psi_i(x) = \begin{cases} \alpha_i \sin(k_i x) + \beta_i \cos(k_i x) & E > V_i \\ \alpha_i \exp(-k_i x) + \beta_i \exp(k_i x) & E < V_i \end{cases} \qquad k = \sqrt{|V - E|} \tag{B.2}$$

Therein, the coefficients α_i and β_i have to be chosen in such a way, that the wave function fulfills the continuity demand at the boundaries of each segment. Moreover, the whole wave function has to be normalized which leads to a quantization of the eigenenergy spectrum. Here, three different termination scenarios can be considered: First, if the potential structure terminates with a wall, which means that the potential energies V_{left}

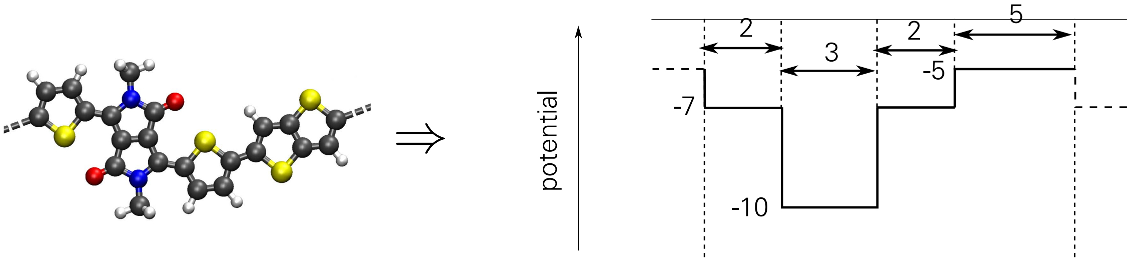

Figure B.1: TDPP-TT polymer chain (left) translated into a simple quantum well structure (right). The latter one was chosen in a way, that the considered polymer is roughly modeled: DPP as the electron acceptor is modeled by the deepest well (-10) while the TT unit as the donor is modeled by highest potential (-5). The thiophene rings were translated to constant potentials of -7.

or V_{right} become infinite, both the wave function and its derivative have to vanish at x_0 or x_n, respectively. Second, if the potential energies V_{left} and V_{right} remain finite, a bounded wave function, $E < \min\left(V_{left}, V_{right}\right)$, has to be described by a decaying exponential functions only. Hence, α_i or β_i are equal to zero according to the considered direction (positive or negative direction). Third, when periodic boundaries are considered, the boundaries have to fulfill the continuity demand according to Bloch's theorem.

Modeling each aromatic units of the TDPP-TT by a constant potential, a 1D structure can be obtained as shown in Fig. B.1. The individual depth and length were chosen in a way to mimic the donor and acceptor properties and the extension of each unit. To this end, DPP as an electron acceptor is modeled by the deepest well of -10, whereas the TT unit as the donor is modeled by the highest potential of -5. The thiophene units in between

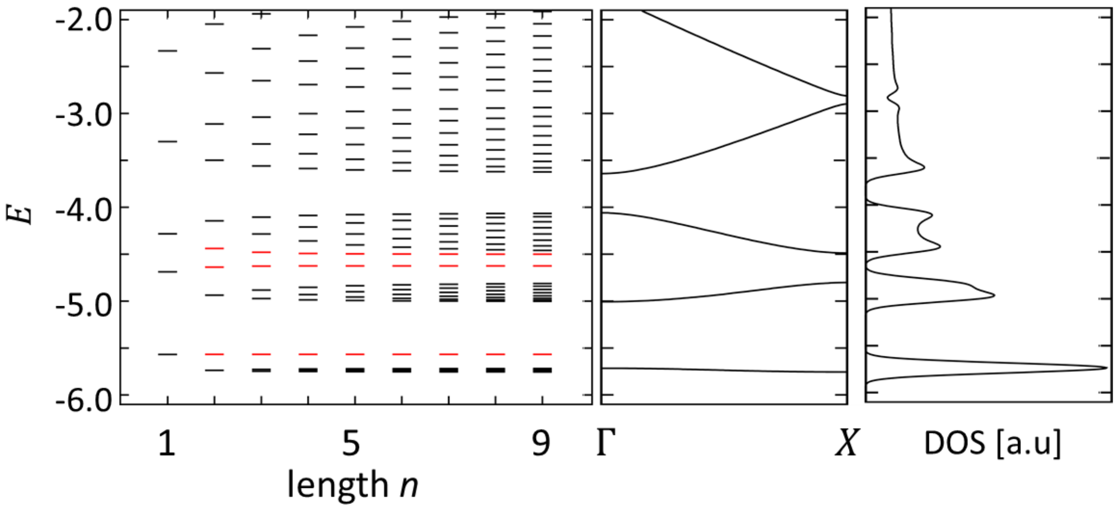

Figure B.2: Electronic levels for finite quantum well structure of different number n of repeat units(left). Slitting of levels due to coupling of successive units. Band structure of infinite system (middle). Comparing the bands to the discrete states of the finite systems, in-gap states can be observed (highlighted in red). Density of states (right).

were translated to constant potentials of −7. The lengths of the wells corresponding to DPP, thiophene and TT were set to 3, 2 and 5, respectively.

By searching for those values E for which the normalization demand is fulfilled, the spectra of the system can be determined. This can be done numerically by means of the shooting method.

The obtained energy spectra for different numbers of repeat units and the band structure of the periodic model are depicted in Fig. B.2. Moreover, the density of states (DOS) is presented. Comparing the eigenvalues of the finite models to the band structure of the infinite one, states with energies outside of the bands are found. These states can be related to the terminations of the model which are not present in the infinite case.

Figure B.3 shows the DOS of the infinite model and the model of nine repeat units in comparison to the projected DOS(pDOS) of the individual repeat units. The pDOS of the central unit is identical to the DOS of the periodic model. The terminating units, however, behave differently. They show peaks where the DOS of the periodic model is zero. Hence, these states are caused by the termination of the models and are hence not present in the infinite case.

Figure B.4 shows the wave functions of the model with nine repeat units with energies −3.6, −4.1 and −4.5. The first two ones can be related to functions of the periodic model. The last one, however, shows a strong restriction to the ninth unit.

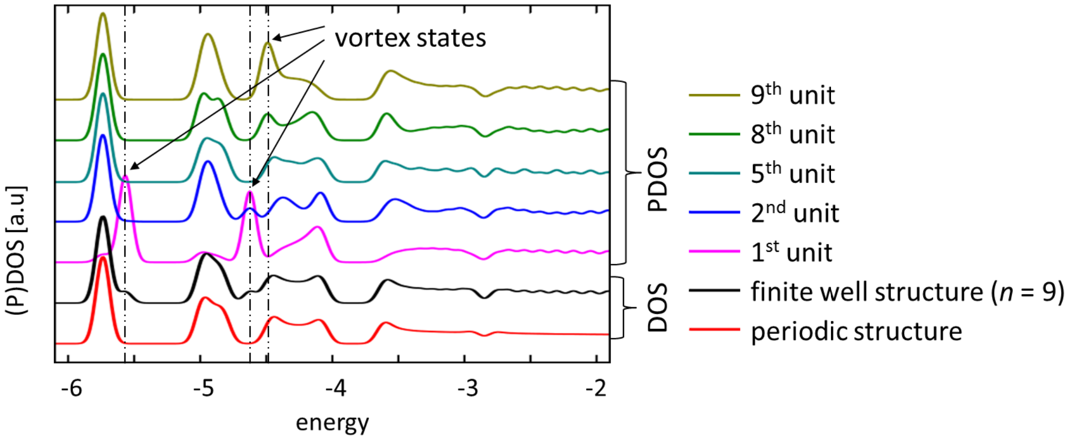

Figure B.3: Comparison of the DOS of the finite system consisting of 9 successive units and the infinite model. Projected density of states to the 1st, 2nd, 5th, 8th and 9th repeat unit of the finite system. PDOS of 5th units reproduce DOS of infinite polymer, but the ones of 1st and 9th unit distinguish. Observation of vortex state for instance at 5.6, 4.6 and 4.5 inside of the band gaps.

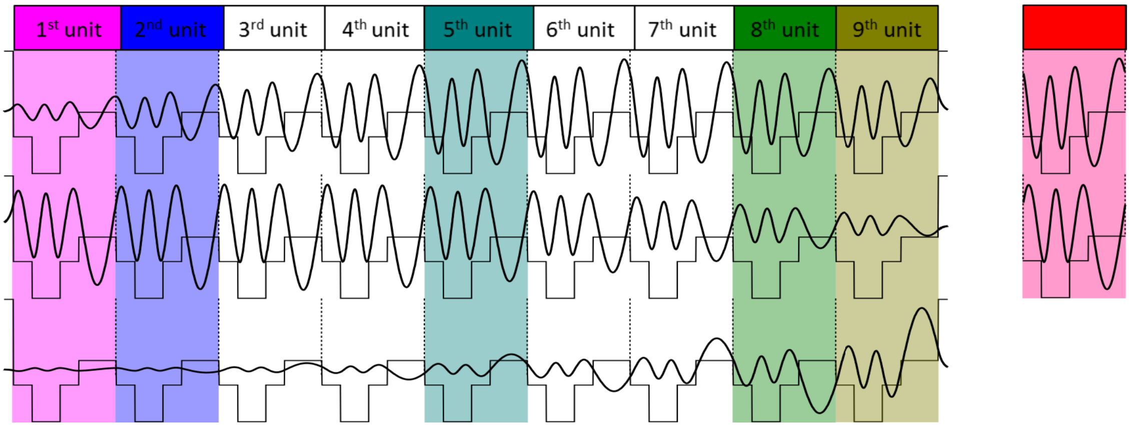

Figure B.4: Selected wave functions of the quantum well structure which consists of nine repeat units: −3.6 (top left), −4.1 (middle left) and −4.5 (bottom left). Comparison to corresponding wave functions to the infinite system. The wave functions in the region of the 5^{th} unit agree with the corresponding infinite version.

C BENCHMARKS FOR THE CALCULATION OF THE COUPLING ELEMENT

For the calculation of the coupling elements T^{h}_{AB}, Eq. (4.27), and T^{e}_{AB}, Eq. (4.26), using the fragment orbital (FO) approach, own subroutines were implemented based on the output formats of DFTB+ [147]. In order to test this implementation, reference systems were considered and compared to FO-DFT as it is implemented in SCM ADF 1.3 software package [123, 144]. For this, the same procedure and parameters were used for FO-DFTB as described in Section 6.2.2: the mio-1-1 parameter were used to calculate the geometry and the MOs of the isolated fragments, whereas the coupling Hamiltonian was derived from parameters generated without confinement potential. For the FO-DFT calculations, the PBE functional and a TZ2P basis was used for both the evaluation of the MOs and

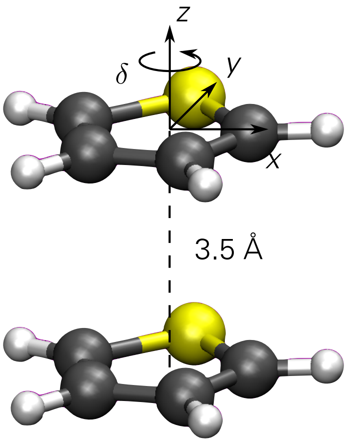

Figure C.1: Representation of the alignment and the considered displacements for evaluate the coupling.

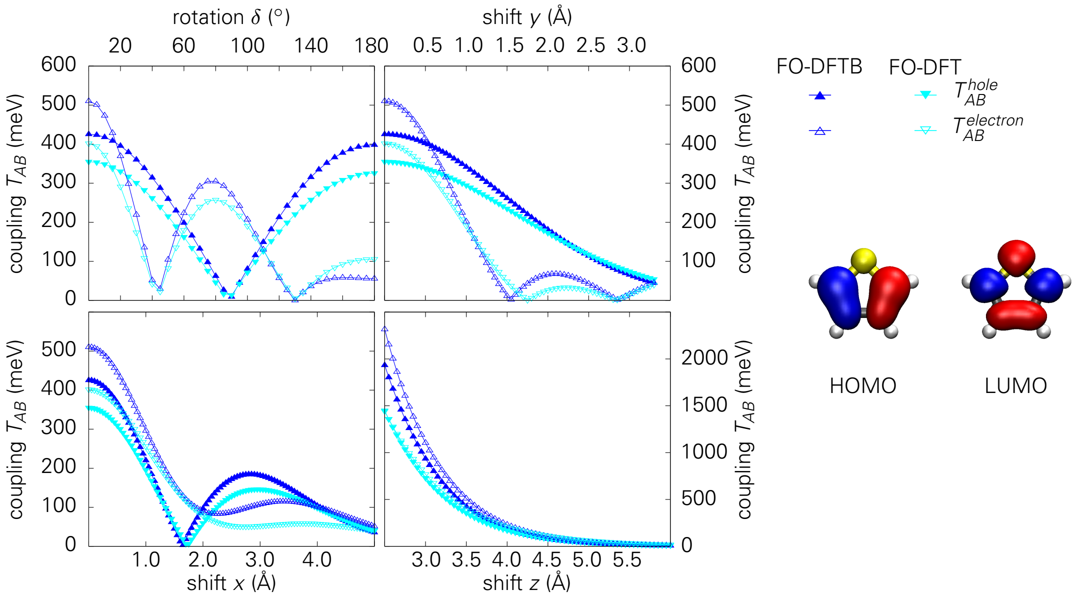

Figure C.2: Dependence of the coupling element between two π-stacked thiophenes on rotation δ as well as shifts in x, y and z direction. On the right hand side, isosurface plots of the HOMO and LUMO wave functions of isolated molecules are given.

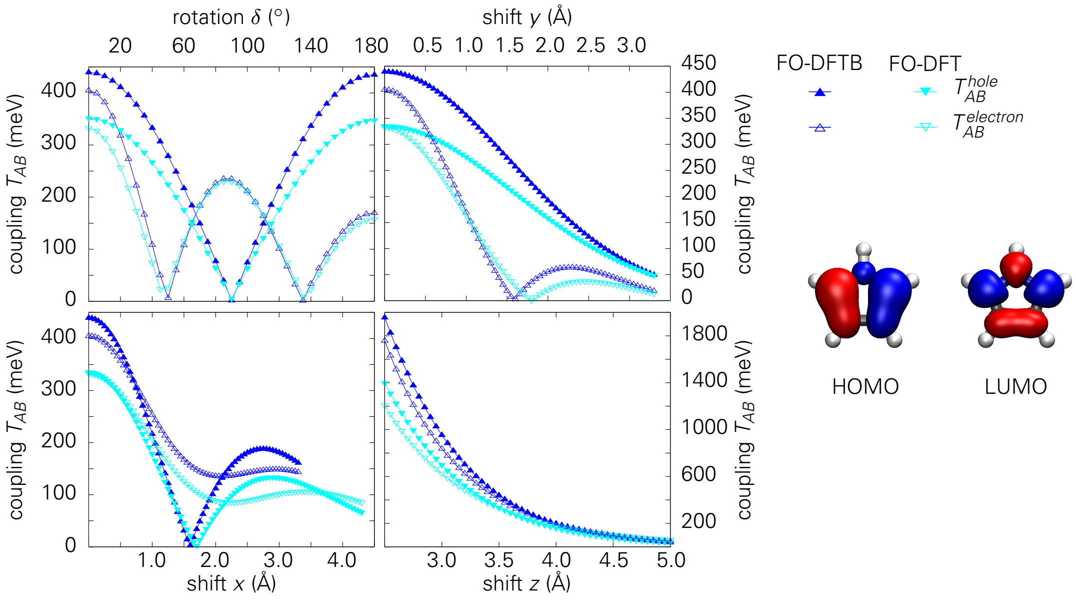

Figure C.3: Same as Fig. C.2 for pyrrol dimer.

the coupling Hamiltonian.

Small molecular models were studied, which were motivated by the precursors of the DA copolymers considered in this thesis. To this end, dimer stacks of thiophene, pyrolle, DPP and 2,5-Dithiophene-2-ylthieno[3,2-B]thiophene (T-TT-T) were considered. In doing so, the coupling elements T_{AB}^{h}, Eq. (4.27), and T_{AB}^{e}, Eq. (4.26), were calculated for various dimer orientations. The dependencies on the stacking distance z, displacements in x and y directions as well as rotations δ around the stacking axis were evaluated, starting from direct stacks in a distance of 3.5 Å, see Fig. C.1. The obtained results are depicted in the figures C.2, C.3, C.4 and C.5. Moreover, these figures depict the isosurface plots of the frontier orbitals, whose spatial shape can be correlated to the curves in the graphs. A comparison for T_{AB}^{h} and T_{AB}^{e} obtained by DFT using SCM ADF 1.3 and DFTB using the own implementations based on DFTB+ is depicted in Fig. C.6. In general, the FO-DFTB values are of a factor of 1.5 larger than the corresponding FO-DFT results. This is in contrast to Kubas *et al.* who observed smaller values compared to FO-DFT and high level *ab inito* calculations and therefore introduced a correction factor for FO-DFTB of 1.5. In their study, however, the Hamiltonian matrix $\hat{H}_{AB}$ was derived from parameter sets which were generated with a reduced confinement of the basis functions. Since herein the parameters were generated without any confinement potential the long range part of

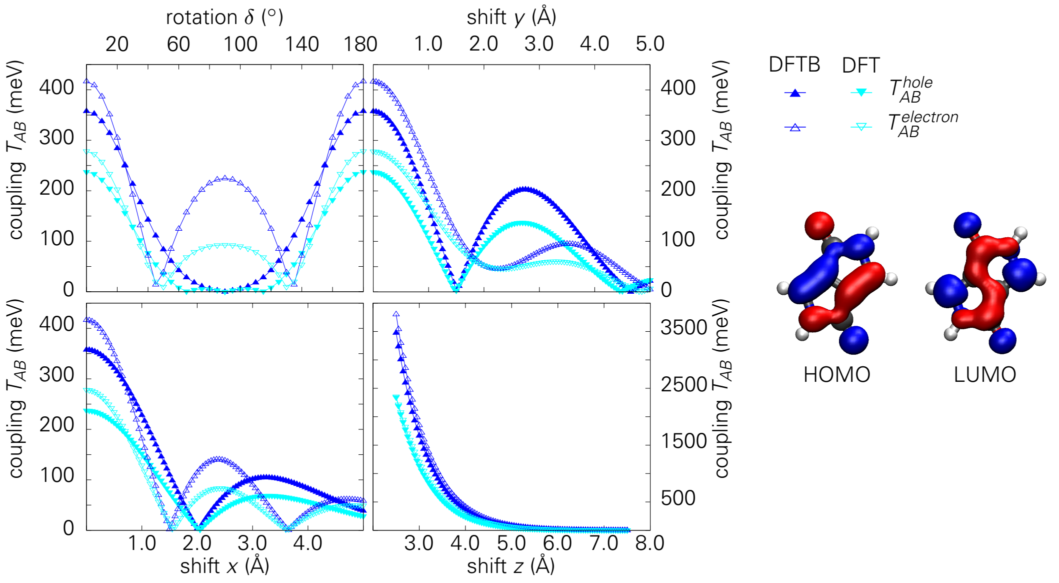

Figure C.4: Same as Fig. C.2 for DPP dimer.

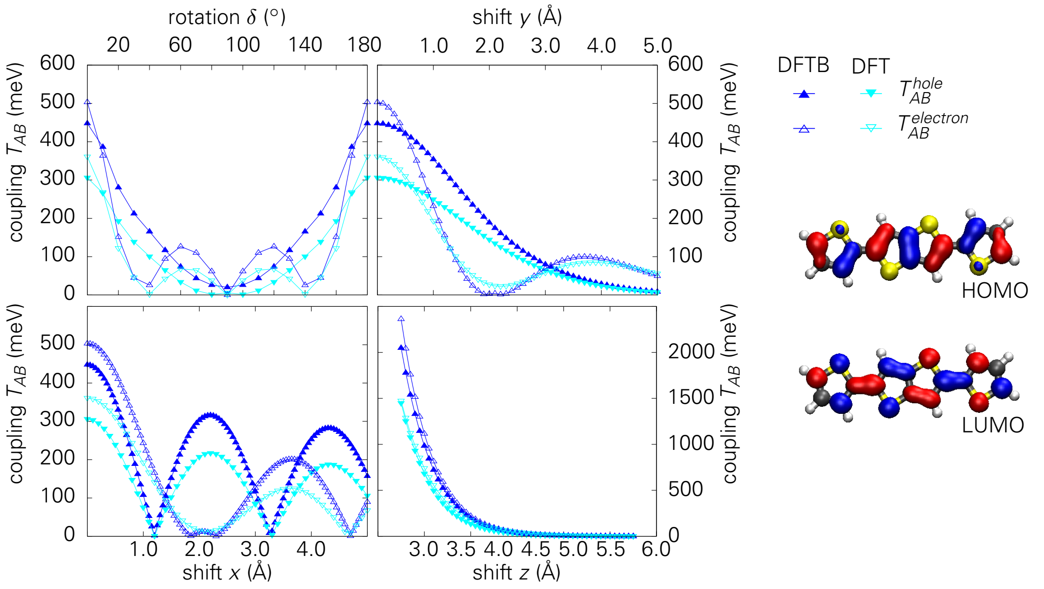

Figure C.5: Same as Fig. C.2 for T-TT-T dimer.

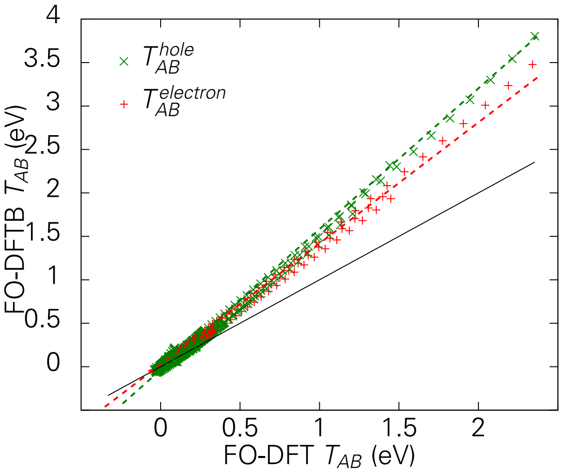

Figure C.6: Comparison of coupling elements of holes (green) and electrons (red) as obtained from FO-DFT using SCM ADF and the own FO-DFTB implementation based on the output of DFTB+ for the molecules discussed above. The lack line indicates the identity whereas the dashed lines give the correlation for T_{AB}^{h} and T_{AB}^{e}.

the wave function is better described and yield therefore larger values. To this end, the correction factor suggested by Kubas and coworkers was not used in this work.

D AVERAGE VALUE APPROACHES OF THE COUPLING ELEMENT

In this thesis diketopyrrolo[3,4-c]pyrrole (DPP) based donor-acceptor copolymer models with different thiophene based compounds as donor unit were studied. In the main text , thieno[3,2-b]thiophene (TT) donor was considered in detail only. The tables D.1, D.2 and D.3 summarize the results when thiophene (T), 2,2'-bithiophene (2T) or 1,2-di(2-thienyl)ethylene (TET) are discussed as donor unit, respectively. Likewise to the main text, the coupling was evaluated for the most stable stacking orientation, $T_{AB}(\vec{R}_{opt})$. Moreover, the Boltzmann-type statistical approaches according to Eq. (6.1) and Eq. (6.2) were employed, to calculate the energy weighted average values $\sqrt{\langle T^2_{AB}\rangle_B}$ and $\sqrt{\langle T^2_{AB}\rangle_{QB}}$.

Table D.1: Same as Tab. 6.1 of P(TDPP-T).

configuration			holes			electrons		
	DPP-T	T-donor	$T^h_{AB}(\vec{R}_{opt})$	$\sqrt{\langle T^2_{AB}\rangle_B}$	$\sqrt{\langle T^2_{AB}\rangle_{QB}}$	$T^e_{AB}(\vec{R}_{opt})$	$\sqrt{\langle T^2_{AB}\rangle_B}$	$\sqrt{\langle T^2_{AB}\rangle_{QB}}$
	trans	*trans*	**167**	**159.7**	**132**	65.4	76.1	64.3
	cis	*trans*	**6.6**	41.8	75.0	**16.9**	**30.4**	**90.3**
	trans	*cis*	15.3	**16.6**	78.9	**110**	**99.8**	52.4
	cis	*cis*	32.0	23.8	**41.2**	47.3	49.2	**51.8**
RMS			85.4	83.8	88.0	68.8	69.1	66.6

For all, the four different isomers *trans*/*trans*, *cis*/*trans*, *trans*/*cis*and *cis*/*cis*were considered in parallel (P) and antiparallel (A) stacking alignments. Since, the TDPP-T model does not fulfill the translational invariance for a single repeat unit, the parallel and antiparallel alignment is considered at once, when two repeat units per unit cell are considered.

As already seen for the TT unit, the values differ very much between the eight different stacking possibilities and the statistical evaluation methods. Taking the averages over all

Table D.2: Same as Tab. 6.1 of P(TDPP-2T).

configuration			holes			electrons		
	DPP-T	T-donor	$T^h_{AB}(\vec{R}_{opt})$	$\sqrt{\langle T^2_{AB}\rangle_B}$	$\sqrt{\langle T^2_{AB}\rangle_{QB}}$	$T^e_{AB}(\vec{R}_{opt})$	$\sqrt{\langle T^2_{AB}\rangle_B}$	$\sqrt{\langle T^2_{AB}\rangle_{QB}}$
P	*trans*	*trans*	**177**	173	133	56.4	101	**107**
P	*cis*	*trans*	108	104	127	33.4	30.9	77.8
P	*trans*	*cis*	128	122	**135**	91.7	86.6	**68.6**
P	*cis*	*cis*	62.4	83.4	123	107	104	104
A	*trans*	*trans*	148	**143**	92.3	110	104	81.5
A	*cis*	*trans*	75.6	120	122	**16.5**	**21.2**	86.8
A	*trans*	*cis*	162	159	**63.2**	82.1	78.9	79.3
A	*cis*	*cis*	**15.2**	**31.7**	107	**155**	**133**	97.3
RMS			121.2	124.1	115.1	91.7	89.9	88.7

Table D.3: Same as Tab. 6.1 of P(TDPP-TET).

configuration			holes			electrons		
	DPP-T	T-donor	$T^h_{AB}(\vec{R}_{opt})$	$\sqrt{\langle T^2_{AB}\rangle_B}$	$\sqrt{\langle T^2_{AB}\rangle_{QB}}$	$T^e_{AB}(\vec{R}_{opt})$	$\sqrt{\langle T^2_{AB}\rangle_B}$	$\sqrt{\langle T^2_{AB}\rangle_{QB}}$
P	*trans*	*trans*	91.3	91.4	108	131	126	**59.7**
P	*cis*	*trans*	78.3	74.7	**78.5**	**151**	**135**	106
P	*trans*	*cis*	56.8	59.0	118	92.7	95.0	88.0
P	*cis*	*cis*	94.5	82.0	**120**	84.7	77.7	116
A	*trans*	*trans*	108	106	102	56.5	**52.4**	72.3
A	*cis*	*trans*	130	123	96.1	85.1	77.7	103
A	*trans*	*cis*	**138**	**142**	113	88.0	92.2	85.0
A	*cis*	*cis*	**36.4**	**42.2**	84.4	**51.8**	52.9	**123**
RMS			97.2	95.1	103.4	97.8	93.2	96.3

considered isomers, however, yield similar values in all cases.

E DOPING PROPERTIES IN F4-TCNQ:4T COMPLEXES

In order to test the work strategy, which was described in section 7.3, charge transfer (CT) complexes of tetrafluoro-tetracyano-quinodimethane (F4-TCNQ) as dopant and quatrothiophene (4T) as polymer models were considered. For this, F4-TCNQ was placed on top of 4T in a distance of 3 Å and shifted along the oligomer direction, see Fig. E.1. For the thus obtained CT complex orientations, single point calculations were performed using PBE functional and a DZP basis set.

Three stable orientations were obtained where in two of them, the dopant is placed on top of a bond between two thiophenes, complex A and C. In complex B, F4-TCNQ is positioned above one thiophene unit. This is in line with the results reported by Pingel *et al.* [56]. For all of these cases, the obtained CT reveals 0.5 up to 0.6 e depending on the used population analysis. Starting from three complexes A, B and C the geometry was optimized using both PBE and B3LYP functionals. In doing so, again a good agreement to literature was found [56]. The obtained CT values are listed in Tab. E.1.

Table E.1: Comparison of CT as obtained from Mulliken, Hirshfeld and Voronoi population analysis.

	Mulliken		Hirshfeld		Voronoi		Literature [56]
	PBE	B3LYP	PBE	B3LYP	PBE	B3LYP	
complex A	0.61	0.59	0.56	0.53	0.67	0.64	0.51
complex B	0.57	0.53	0.48	0.47	0.56	0.60	0.43
complex C	0.60	-	0.53	-	0.59	-	0.46

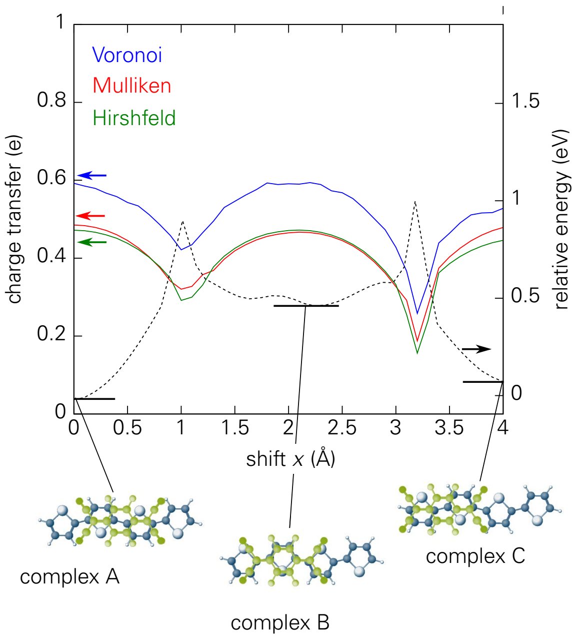

Figure E.1: Calculated charge transfer and energy for the CT complex F4-TCNQ:4T complexes for a stacking distance of 3 Å. The shift *x* indicates the relative distance of the centers of masses for two molecules in backbone direction. The colored curves specify the CT obtained by the different population analyses (left scale) while the black one give the formation energy (right scale).

References

BIBLIOGRAPHY

[1] A. Facchetti, "π-conjugated polymers for organic electronics and photovoltaic cell applications," *Chemistry of Materials*, vol. 23, no. 3, p. 733, 2011.

[2] H. Klauk, "Organic thin-film transistors," *Chemical Society Reviews*, vol. 39, no. 7, p. 2643, 2010.

[3] H. Sirringhaus, "25th anniversary article: Organic field-effect transistors: the path beyond amorphous silicon," *Advanced Materials*, vol. 26, no. 9, p. 1319, 2014.

[4] C. Zhong, C. Duan, F. Huang, H. Wu, and Y. Cao, "Materials and devices toward fully solution processable organic light-emitting diodes," *Chemistry of Materials*, vol. 23, no. 3, p. 326, 2011.

[5] L. Lu, T. Zheng, Q. Wu, A. M. Schneider, D. Zhao, and L. Yu, "Recent advances in bulk heterojunction polymer solar cells," *Chemical Reviews*, vol. 115, no. 23, p. 12666, 2015.

[6] P.-L. T. Boudreault, A. Najari, and M. Leclerc, "Processable low-bandgap polymers for photovoltaic applications," *Chemistry of Materials*, vol. 23, no. 3, p. 456, 2010.

[7] K. Myny, S. Steudel, P. Vicca, M. J. Beenhakkers, N. A. van Aerle, G. H. Gelinck, J. Genoe, W. Dehaene, and P. Heremans, "Organic RFID tags," in *Radio Frequency Identification Fundamentals and Applications Design Methods and Solutions*, InTech, 2010.

[8] P. M. Beaujuge and J. R. Reynolds, "Color control in π-conjugated organic polymers for use in electrochromic devices," *Chemical Reviews*, vol. 110, no. 1, p. 268, 2010.

[9] M. Culebras, C. Gómez, and A. Cantarero, "Review on polymers for thermoelectric applications," *Materials*, vol. 7, no. 9, p. 6701, 2014.

[10] M. He, F. Qiu, and Z. Lin, "Towards high-performance polymer-based thermoelectric materials," *Energy & Environmental Science*, vol. 6, no. 5, p. 1352, 2013.

[11] T. Janoschka, M. D. Hager, and U. S. Schubert, "Powering up the future: Radical polymers for battery applications," *Advanced Materials*, vol. 24, no. 48, p. 6397, 2012.

[12] R. Gracia and D. Mecerreyes, "Polymers with redox properties: materials for batteries, biosensors and more," *Polymer Chemistry*, vol. 4, no. 7, p. 2206, 2013.

[13] L. Torsi, M. Magliulo, K. Manoli, and G. Palazzo, "Organic field-effect transistor sensors: a tutorial review," *Chemical Society Reviews*, vol. 42, no. 22, p. 8612, 2013.

[14] W. Demtröder, *Experimentalphysik2 - Elektrizität und Optik*. Berlin Heidelberg New York: Springer-Verlag, 2013.

[15] W. Demtröder, *Experimentalphysik3 - Atome, Moleküle und Festkörper*. Berlin, Heidelberg: Springer, 2000.

[16] G. Ludwig and R. Watters, "Drift and conductivity mobility in silicon," *Physical Review*, vol. 101, no. 6, p. 1699, 1956.

[17] H. Klauk, *Organic Electronics - Materials, Manufacturing, and Applications*. New York: John Wiley & Sons, 2006.

[18] X. Zhang, P. Bauerle, T. Aida, P. Skabara, and C. Kagan, "Organic electronics for a better tomorrow: Innovation, accessibility, sustainability," in *A White Pap. From Chem. Sci. Soc. Summit San Fr. California, United States*, 2012.

[19] S. Patel, H. Park, P. Bonato, L. Chan, and M. Rodgers, "A review of wearable sensors and systems with application in rehabilitation," *Journal of Neuroengineering and Rehabilitation*, vol. 9, no. 1, p. 21, 2012.

[20] M. Stoppa and A. Chiolerio, "Wearable electronics and smart textiles: a critical review," *Sensors*, vol. 14, no. 7, p. 11957, 2014.

[21] G. H. Gelinck, H. E. A. Huitema, E. van Veenendaal, E. Cantatore, L. Schrijnemakers, J. B. van der Putten, T. C. Geuns, M. Beenhakkers, J. B. Giesbers, B.-H. Huisman, *et al.*, "Flexible active-matrix displays and shift registers based on solution-processed organic transistors," *Nature Materials*, vol. 3, no. 2, p. 106, 2004.

[22] G. S. Ryu, J. S. Kim, S. H. Jeong, and C. K. Song, "A printed otft-backplane for amoled display," *Organic Electronics*, vol. 14, no. 4, p. 1218, 2013.

[23] D. De Leeuw and E. Cantatore, "Organic electronics: Materials, technology and circuit design developments enabling new applications," *Materials Science in Semiconductor Processing*, vol. 11, no. 5, p. 199, 2008.

[24] C. Wang, H. Dong, W. Hu, Y. Liu, and D. Zhu, "Semiconducting π-conjugated systems in field-effect transistors: a material odyssey of organic electronics," *Chemical Reviews*, vol. 112, no. 4, p. 2208, 2011.

[25] W. Kaiser, *Kunststoffchemie für Ingenieure - Von der Synthese bis zur Anwendung*. München: Carl Hanser Verlag GmbH Co KG, 2015.

[26] H. Shirakawa, E. J. Louis, A. G. MacDiarmid, C. K. Chiang, and A. J. Heeger, "Synthesis of electrically conducting organic polymers: halogen derivatives of polyacetylene,(ch) x," *Journal of the Chemical Society, Chemical Communications*, no. 16, p. 578, 1977.

[27] C. Chiang, M. Druy, S. Gau, A. Heeger, E. Louis, A. G. MacDiarmid, Y. Park, and H. Shirakawa, "Synthesis of highly conducting films of derivatives of polyacetylene,(ch) x," *Journal of the American Chemical Society*, vol. 100, no. 3, p. 1013, 1978.

[28] C. K. Chiang, C. Fincher Jr, Y. W. Park, A. J. Heeger, H. Shirakawa, E. J. Louis, S. C. Gau, and A. G. MacDiarmid, "Electrical conductivity in doped polyacetylene," *Physical Review Letters*, vol. 39, no. 17, p. 1098, 1977.

[29] H. Shirakawa, "The discovery of polyacetylene film: the dawning of an era of conducting polymers (nobel lecture)," *Angewandte Chemie International Edition*, vol. 40, no. 14, p. 2574, 2001.

[30] B. Nordén and E. Krutmeijer, "The nobel prize in chemistry, 2000: Conductive polymers," *Kungl. Vetenskapsakademien (The Royal Swedish Academy of Sciences)*, p. 1, 2000.

[31] M. Winokur, P. Wamsley, J. Moulton, P. Smith, and A. Heeger, "Structural evolution in iodine-doped poly(3-alkylthiophenes)," *Macromolecules*, vol. 24, no. 13, p. 3812, 1991.

[32] S. Holliday, J. E. Donaghey, and I. McCulloch, "Advances in charge carrier mobilities of semiconducting polymers used in organic transistors," *Chemistry of Materials*, vol. 26, no. 1, p. 647, 2013.

[33] H. Sirringhaus, N. Tessler, and R. H. Friend, "Integrated optoelectronic devices based on conjugated polymers," *Science*, vol. 280, no. 5370, p. 1741, 1998.

[34] G. Wang, J. Swensen, D. Moses, and A. J. Heeger, "Increased mobility from regioregular poly(3-hexylthiophene) field-effect transistors," *Journal of Applied Physics*, vol. 93, no. 10, p. 6137, 2003.

[35] Z. Bao, A. Dodabalapur, and A. J. Lovinger, "Soluble and processable regioregular poly(3-hexylthiophene) for thin film field-effect transistor applications with high mobility," *Applied Physics Letters*, vol. 69, no. 26, p. 4108, 1996.

[36] E. Meijer, C. Detcheverry, P. Baesjou, E. Van Veenendaal, D. De Leeuw, and T. Klapwijk, "Dopant density determination in disordered organic field-effect transistors," *Journal of Applied Physics*, vol. 93, no. 8, p. 4831, 2003.

[37] M. S. Abdou, F. P. Orfino, Y. Son, and S. Holdcroft, "Interaction of oxygen with conjugated polymers: Charge transfer complex formation with poly(3-alkylthiophenes)," *Journal of the American Chemical Society*, vol. 119, no. 19, p. 4518.

[38] I. McCulloch, M. Heeney, C. Bailey, K. Genevicius, I. MacDonald, M. Shkunov, D. Sparrowe, S. Tierney, R. Wagner, W. Zhang, M. L. Chabinyc, R. J. Kline, M. D. McGehee, and M. F. Toney, "Liquid-crystalline semiconducting polymers with high charge-carrier mobility," *Nature Materials*, vol. 5, no. 4, p. 328, 2006.

[39] B. H. Hamadani, D. J. Gundlach, I. McCulloch, and M. Heeney, "Undoped polythiophene field-effect transistors with mobility of $1\text{cm}^2\text{v}^{-1}\text{s}^{-1}$," *Applied Physics Letters*, vol. 91, no. 24, p. 243512, 2007.

[40] X. Guo, F. S. Kim, S. A. Jenekhe, and M. D. Watson, "Phthalimide-based polymers for high performance organic thin-film transistors," *Journal of the American Chemical Society*, vol. 131, no. 21, p. 7206.

[41] I. McCulloch, R. S. Ashraf, L. Biniek, H. Bronstein, C. Combe, J. E. Donaghey, D. I. James, C. B. Nielsen, B. C. Schroeder, and W. Zhang, "Design of semiconducting indacenodithiophene polymers for high performance transistors and solar cells," *Accounts of Chemical Research*, vol. 45, no. 5, p. 714, 2012.

[42] U. Salzner, "Does the donor-acceptor concept work for designing synthetic metals? 1. theoretical investigation of poly(3-cyano-3-hydroxybithiophene)," *The Journal of Physical Chemistry B*, vol. 106, no. 36, p. 9214, 2002.

[43] H. Luo, Z. Cai, L. Tan, Y. Guo, G. Yang, Z. Liu, G. Zhang, D. Zhang, W. Xu, and Y. Liu, "Solution-processed core-extended naphthalene diimides toward organic n-type and ambipolar semiconductors," *Journal of Materials Chemistry C*, vol. 1, no. 15, p. 2688, 2013.

[44] B. Reeves, D. Shircliff, J. Shott, and B. Boardman, "Synthesis and investigation of cobalt chalcogenide clusters with thienyl phosphine ligands as new acceptor materials for P3HT," *Dalton Transactions*, vol. 44, no. 2, p. 718, 2015.

[45] L. Gao, Z.-G. Zhang, L. Xue, J. Min, J. Zhang, Z. Wei, and Y. Li, "All-polymer solar cells based on absorption-complementary polymer donor and acceptor with high

power conversion efficiency of 8.27%," *Advanced Materials*, vol. 28, no. 9, p. 1884, 2016.

[46] M. M. Durban, P. D. Kazarinoff, and C. K. Luscombe, "Synthesis and characterization of thiophene-containing naphthalene diimide n-type copolymers for ofet applications," *Macromolecules*, vol. 43, no. 15, p. 6348, 2010.

[47] R. Kim, P. S. K. Amegadze, I. Kang, H.-J. Yun, Y.-Y. Noh, S.-K. Kwon, and Y.-H. Kim, "High-mobility air-stable naphthalene diimide-based copolymer containing extended π-conjugation for n-channel organic field effect transistors," *Advanced Functional Materials*, vol. 23, no. 46, p. 5719, 2013.

[48] H. Chen, Y. Guo, Z. Mao, G. Yu, J. Huang, Y. Zhao, and Y. Liu, "Naphthalenediimide-based copolymers incorporating vinyl-linkages for high-performance ambipolar field-effect transistors and complementary-like inverters under air," *Chemistry of Materials*, vol. 25, no. 18, p. 3589, 2013.

[49] J. Li, Y. Zhao, H. S. Tan, Y. Guo, C.-A. Di, G. Yu, Y. Liu, M. Lin, S. H. Lim, Y. Zhou, *et al.*, "A stable solution-processed polymer semiconductor with record high-mobility for printed transistors," *Scientific Reports*, vol. 2, 2012.

[50] I. Kang, H.-J. Yun, D. S. Chung, S.-K. Kwon, and Y.-H. Kim, "Record high hole mobility in polymer semiconductors via side-chain engineering," *Journal of the American Chemical Society*, vol. 135, no. 40, p. 14896, 2013.

[51] B. Sun, W. Hong, Z. Yan, H. Aziz, and Y. Li, "Record high electron mobility of 6.3 $\mathrm{cm}^{-2}\mathrm{v}^{-1}\mathrm{s}^{-1}$achieved for polymer semiconductors using a new building block," *Advanced Materials*, vol. 26, no. 17, p. 2636, 2014.

[52] D. Di Nuzzo, C. Fontanesi, R. Jones, S. Allard, I. Dumsch, U. Scherf, E. Von Hauff, S. Schumacher, and E. Da Como, "How intermolecular geometrical disorder affects the molecular doping of donor–acceptor copolymers," *Nature Communications*, vol. 6, p. 6460, 2015.

[53] I. Salzmann, G. Heimel, M. Oehzelt, S. Winkler, and N. Koch, "Molecular electrical doping of organic semiconductors: fundamental mechanisms and emerging dopant design rules," *Accounts of Chemical Research*, vol. 49, no. 3, p. 370, 2016.

[54] P. Pingel and D. Neher, "Comprehensive picture of p-type doping of P3HT with the molecular acceptor F4TCNQ," *Physical Review B*, vol. 87, no. 11, p. 115209, 2013.

[55] F. Ghani, A. Opitz, P. Pingel, G. Heimel, I. Salzmann, J. Frisch, D. Neher, A. Tsami, U. Scherf, and N. Koch, "Charge transfer in and conductivity of molecularly doped thiophene-based copolymers," *Journal of Polymer Science Part B: Polymer Physics*, vol. 53, no. 1, p. 58, 2015.

[56] P. Pingel, L. Zhu, K. S. Park, J.-O. Vogel, S. Janietz, E.-G. Kim, J. P. Rabe, J.-L. Brédas, and N. Koch, “Charge-transfer localization in molecularly doped thiophene-based donor polymers,” *The Journal of Physical Chemistry Letters*, vol. 1, no. 13, p. 2037, 2010.

[57] M. L. Hammock, A. Chortos, B. C.-K. Tee, J. B.-H. Tok, and Z. Bao, “25th anniversary article: the evolution of electronic skin (e-skin): a brief history, design considerations, and recent progress,” *Advanced Materials*, vol. 25, no. 42, p. 5997, 2013.

[58] J. Reinhold, *Quantentheorie der Moleküle - Eine Einführung*. Berlin Heidelberg New York: Springer-Verlag, 2015.

[59] E. Schrödinger, “Quantisierung als Eigenwertproblem,” *Annalen der Physik*, vol. 385, no. 13, p. 437, 1926.

[60] M. Born and R. Oppenheimer, “Zur Quantentheorie der Moleküle,” *Annalen der Physik*, vol. 389, no. 20, p. 457, 1927.

[61] N. W. Ashcroft and D. N. Mermin, *Festkörperphysik*. München: Oldenbourg Wissenschaftsverlag, 2012.

[62] F. Bloch, “Bemerkung zur elektronentheorie des ferromagnetismus und der elektrischen leitfähigkeit,” *Zeitschrift für Physik A Hadrons and Nuclei*, vol. 57, no. 7, p. 545, 1929.

[63] F. Bloch, “Über die Quantenmechanik der Elektronen in Kristallgittern,” *Zeitschrift für Physik A Hadrons and Nuclei*, vol. 52, no. 7, p. 555, 1929.

[64] C. Kittel, *Einführung in die Festkörperphysik*. München: Oldenbourg Wissenschaftsverlag, 2013.

[65] W. Koch and M. C. Holthausen, *A Chemist’s Guide to Density Functional Theory*. New York: John Wiley & Sons, 2015.

[66] R. G. Parr and Y. Weitao, *Density-Functional Theory of Atoms and Molecules*. New York: Oxford University Press, 1994.

[67] P. Hohenberg and W. Kohn, “Inhomogeneous electron gas,” *Physical Review*, vol. 136, no. 3B, p. B864, 1964.

[68] W. Kohn and L. J. Sham, “Self-consistent equations including exchange and correlation effects,” *Physical Review*, vol. 140, p. A1133, 1965.

[69] P. A. Dirac, “Note on exchange phenomena in the thomas atom,” in *Mathematical Proceedings of the Cambridge Philosophical Society*, vol. 26, p. 376, Cambridge University Press, 1930.

[70] L. Hedin and S. Lundqvist, “On local density schemes,” *Le Journal de Physique Colloques*, vol. 33, no. C3, p. C3, 1972.

[71] D. M. Ceperley and B. Alder, “Ground state of the electron gas by a stochastic method,” *Physical Review Letters*, vol. 45, no. 7, p. 566, 1980.

[72] S. H. Vosko, L. Wilk, and M. Nusair, “Accurate spin-dependent electron liquid correlation energies for local spin density calculations: a critical analysis,” *Canadian Journal of Physics*, vol. 58, no. 8, p. 1200, 1980.

[73] J. P. Perdew and A. Zunger, “Self-interaction correction to density-functional approximations for many-electron systems,” *Physical Review B*, vol. 23, no. 10, p. 5048, 1981.

[74] L. A. Cole and J. P. Perdew, “Calculated electron affinities of the elements,” *Physical Review A*, vol. 25, no. 3, p. 1265, 1982.

[75] J. P. Perdew and Y. Wang, “Accurate and simple analytic representation of the electron-gas correlation energy,” *Physical Review B*, vol. 45, no. 23, p. 13244, 1992.

[76] A. D. Becke, “Density-functional exchange-energy approximation with correct asymptotic behavior,” *Physical Review A*, vol. 38, no. 6, p. 3098, 1988.

[77] C. Lee, W. Yang, and R. G. Parr, “Development of the colle-salvetti correlation-energy formula into a functional of the electron density,” *Physical Review B*, vol. 37, no. 2, p. 785, 1988.

[78] J. P. Perdew, K. Burke, and M. Ernzerhof, “Generalized gradient approximation made simple,” *Physical Review Letters*, vol. 77, no. 18, p. 3865, 1996.

[79] S. Blügel, *Computing Solids - Models, Ab-initio Methods and Supercomputing - Lecture Notes of the 45th IFF Spring School 2014*. Jülich: Forschungszentrum, Zentralbibliothek, 2014.

[80] R. S. Mulliken, “Electronic population analysis on LCAO–MO molecular wave functions. i,” *The Journal of Chemical Physics*, vol. 23, no. 10, p. 1833, 1955.

[81] S. Saha, R. K. Roy, and P. W. Ayers, “Are the hirshfeld and mulliken population analysis schemes consistent with chemical intuition?,” *International Journal of Quantum Chemistry*, vol. 109, no. 9, p. 1790, 2009.

[82] C. Fonseca Guerra, J.-W. Handgraaf, E. J. Baerends, and F. M. Bickelhaupt, “Voronoi deformation density (vdd) charges: Assessment of the mulliken, bader, hirshfeld, weinhold, and vdd methods for charge analysis,” *Journal of Computational Chemistry*, vol. 25, no. 2, p. 189, 2004.

[83] G. Seifert, H. Eschrig, and W. Bieger, “Eine approximative Variante des LCAO- Xα Verfahrens,” *Zeitschrift für physikalische Chemie*, vol. 267, p. 529, 1986.

[84] P. Blaudeck, T. Frauenheim, D. Porezag, G. Seifert, and E. Fromm, "A method and results for realistic molecular dynamic simulation of hydrogenated amorphous carbon structures using a scheme consisting of a linear combination of atomic orbitals with the local-density approximation," *Journal of Physics: Condensed Matter*, vol. 4, no. 30, p. 6389, 1992.

[85] D. Porezag, T. Frauenheim, T. Köhler, G. Seifert, and R. Kaschner, "Construction of tight-binding-like potentials on the basis of density-functional theory: Application to carbon," *Physical Review B*, vol. 51, no. 19, p. 12947, 1995.

[86] "Calculations of molecules, clusters, and solids with a simplified LCAO-DFT-LDA0 scheme, author=Seifert, G and Porezag, D and Frauenheim, Th, journal=International Journal of Quantum Chemistry, volume=58, number=2, pages=185, year=1996, publisher=Wiley Online Library,"

[87] M. Elstner, D. Porezag, G. Jungnickel, J. Elsner, M. Haugk, T. Frauenheim, S. Suhai, and G. Seifert, "Self-consistent-charge density-functional tight-binding method for simulations of complex materials properties," *Physical Review B*, vol. 58, p. 7260, 1998.

[88] T. Frauenheim, G. Seifert, M. Elsterner, Z. Hajnal, G. Jungnickel, D. Porezag, S. Suhai, and R. Scholz, "A self-consistent charge density-functional based tight-binding method for predictive materials simulations in physics, chemistry and biology," *Physica Status Solidi (b)*, vol. 217, no. 1, p. 41, 2000.

[89] T. Frauenheim, G. Seifert, M. Elstner, T. Niehaus, C. Köhler, M. Amkreutz, M. Sternberg, Z. Hajnal, A. Di Carlo, and S. Suhai, "Atomistic simulations of complex materials: ground-state and excited-state properties," *Journal of Physics: Condensed Matter*, vol. 14, no. 11, p. 3015, 2002.

[90] C. Köhler, G. Seifert, U. Gerstmann, M. Elstner, H. Overhof, and T. Frauenheim, "Approximate density-functional calculations of spin densities in large molecular systems and complex solids," *Physical Chemistry Chemical Physics*, vol. 3, no. 23, p. 5109, 2001.

[91] T. A. Niehaus, S. Suhai, F. Della Sala, P. Lugli, M. Elstner, G. Seifert, and T. Frauenheim, "Tight-binding approach to time-dependent density-functional response theory," *Physical Review B*, vol. 63, no. 8, p. 085108, 2001.

[92] G. Seifert, "Tight-binding density functional theory: An approximate Kohn-Sham DFT scheme," *The Journal of Physical Chemistry A*, vol. 111, no. 26, p. 5609, 2007.

[93] W. M. C. Foulkes and R. Haydock, "Tight-binding models and density-functional theory," *Physical Review B*, vol. 39, no. 17, p. 12520, 1989.

[94] H. Eschrig and I. Bergert, "An optimized lcao version for band structure calculations application to copper," *Physica Status Solidi (b)*, vol. 90, no. 2, p. 621, 1978.

[95] H. Eschrig, *Optimized LCAO Method and the Electronic Structure of Extended Systems (Research Reports in Physics)*. Berlin Heidelberg: Springer, 1989.

[96] J. C. Slater and G. F. Koster, "Simplified LCAO method for the periodic potential problem," *Physical Review*, vol. 94, no. 6, p. 1498, 1954.

[97] J. Nocedal and S. Wright, *Numerical Optimization*. Berlin Heidelberg: Springer Science & Business Media, 2006.

[98] A. Köster, *Entwicklung einer LCGTO-Dichtefunktionalmethode mit Hilfsfunktionen*. habilitation, Universität Hannover, 1998.

[99] G. Seifert and J.-O. Joswig, "Density-functional tight binding—an approximate density-functional theory method," *Wiley Interdisciplinary Reviews: Computational Molecular Science*, vol. 2, no. 3, p. 456, 2012.

[100] S. Grimme, "Density functional theory with london dispersion corrections," *Wiley Interdisciplinary Reviews: Computational Molecular Science*, vol. 1, no. 2, p. 211, 2011.

[101] V. R. Cooper, L. Kong, and D. C. Langreth, "Computing dispersion interactions in density functional theory," *Physics Procedia*, vol. 3, no. 3, p. 1417, 2010.

[102] M. Elstner, P. Hobza, T. Frauenheim, S. Suhai, and E. Kaxiras, "Hydrogen bonding and stacking interactions of nucleic acid base pairs: a density-functional-theory based treatment," *The Journal of Chemical Physics*, vol. 114, no. 12, p. 5149, 2001.

[103] L. Zhechkov, T. Heine, S. Patchkovskii, G. Seifert, and H. A. Duarte, "An efficient a posteriori treatment for dispersion interaction in density-functional-based tight binding," *Journal of Chemical Theory and Computation*, vol. 1, no. 5, p. 841, 2005.

[104] S. Grimme, "Accurate description of van der waals complexes by density functional theory including empirical corrections," *Journal of Computational Chemistry*, vol. 25, no. 12, p. 1463, 2004.

[105] S. Grimme, "Semiempirical gga-type density functional constructed with a long-range dispersion correction," *Journal of Computational Chemistry*, vol. 27, no. 15, p. 1787, 2006.

[106] J.-D. Chai and M. Head-Gordon, "Long-range corrected hybrid density functionals with damped atom–atom dispersion corrections," *Physical Chemistry Chemical Physics*, vol. 10, no. 44, p. 6615, 2008.

[107] A. K. Rappé, C. J. Casewit, K. Colwell, W. Goddard Iii, and W. Skiff, "UFF, a full periodic table force field for molecular mechanics and molecular dynamics simulations," *Journal of the American Chemical Society*, vol. 114, no. 25, p. 10024, 1992.

[108] V. May and O. Kühn, *Charge and Energy Transfer Dynamics in Molecular Systems*. New York: John Wiley & Sons, 2011.

[109] P. Drude, "Zur Elektronentheorie der Metalle," *Annalen der Physik*, vol. 306, no. 3, p. 566, 1900.

[110] A. Sommerfeld and H. Bethe, "Elektronentheorie der Metalle," in *Aufbau der zusammenhängenden Materie*, p. 333, Springer, 1933.

[111] R. A. Marcus, "On the theory of oxidation-reduction reactions involving electron transfer. i," *The Journal of Chemical Physics*, vol. 24, no. 5, p. 966, 1956.

[112] R. A. Marcus, "Electrostatic free energy and other properties of states having nonequilibrium polarization. i," *The Journal of Chemical Physics*, vol. 24, no. 5, p. 979, 1956.

[113] R. Marcus, "Chemical and electrochemical electron-transfer theory," *Annual Review of Physical Chemistry*, vol. 15, no. 1, p. 155, 1964.

[114] R. A. Marcus, "On the theory of electron-transfer reactions. vi. unified treatment for homogeneous and electrode reactions," *The Journal of Chemical Physics*, vol. 43, no. 2, p. 679, 1965.

[115] N. Sutin, "Theory of electron transfer reaction: Insights and hindsights," *Progress in Inorganic Chemistry, and Appreciation of Henry Taube*, vol. 30, p. 441, 2009.

[116] R. A. Marcus, "Electron transfer reactions in chemistry: theory and experiment (nobel lecture)," *Angewandte Chemie International Edition*, vol. 32, no. 8, p. 1111, 1993.

[117] P. A. Dirac, "The quantum theory of the emission and absorption of radiation," in *Proceedings of the Royal Society of London A: Mathematical, Physical and Engineering Sciences*, vol. 114, p. 243, The Royal Society, 1927.

[118] R. J. Cave and M. D. Newton, "Generalization of the mulliken-hush treatment for the calculation of electron transfer matrix elements," *Chemical Physics Letters*, vol. 249, no. 1-2, p. 15, 1996.

[119] R. J. Cave and M. D. Newton, "Calculation of electronic coupling matrix elements for ground and excited state electron transfer reactions: comparison of the generalized mulliken–hush and block diagonalization methods," *The Journal of Chemical Physics*, vol. 106, no. 22, p. 9213, 1997.

[120] Q. Wu and T. Van Voorhis, "Direct optimization method to study constrained systems within density-functional theory," *Physical Review A*, vol. 72, no. 2, p. 024502, 2005.

[121] Q. Wu and T. Van Voorhis, "Constrained density functional theory and its application in long-range electron transfer," *Journal of Chemical Theory and computation*, vol. 2, no. 3, p. 765, 2006.

[122] Q. Wu and T. Van Voorhis, "Extracting electron transfer coupling elements from constrained density functional theory," *The Journal of Chemical Physics*, vol. 125, no. 16, p. 164105, 2006.

[123] G. T. te Velde, F. M. Bickelhaupt, E. J. Baerends, C. Fonseca Guerra, S. J. van Gisbergen, J. G. Snijders, and T. Ziegler, "Chemistry with ADF," *Journal of Computational Chemistry*, vol. 22, no. 9, p. 931, 2001.

[124] H. Oberhofer and J. Blumberger, "Revisiting electronic couplings and incoherent hopping models for electron transport in crystalline C60 at ambient temperatures," *Physical Chemistry Chemical Physics*, vol. 14, no. 40, p. 13846, 2012.

[125] K. Senthilkumar, F. Grozema, F. Bickelhaupt, and L. Siebbeles, "Charge transport in columnar stacked triphenylenes: effects of conformational fluctuations on charge transfer integrals and site energies," *The Journal of Chemical Physics*, vol. 119, no. 18, p. 9809, 2003.

[126] A. Kubas, F. Hoffmann, A. Heck, H. Oberhofer, M. Elstner, and J. Blumberger, "Electronic couplings for molecular charge transfer: Benchmarking CDFT, FODFT, and FODFTB against high-level ab initio calculations," *The Journal of chemical physics*, vol. 140, no. 10, p. 104105, 2014.

[127] A. Kubas, F. Gajdos, A. Heck, H. Oberhofer, M. Elstner, and J. Blumberger, "Electronic couplings for molecular charge transfer: benchmarking CDFT, FODFT and FODFTB against high-level ab initio calculations. ii," *Physical Chemistry Chemical Physics*, vol. 142, no. 12, p. 129905, 2015.

[128] F. Günther, S. Gemming, and G. Seifert, "Hopping-based charge transfer in diketopyrrolopyrrole-based donor–acceptor polymers: A theoretical study," *The Journal of Physical Chemistry C*, vol. 120, no. 18, pp. 9581–9587, 2016.

[129] J. Nelson, J. J. Kwiatkowski, J. Kirkpatrick, and J. M. Frost, "Modeling charge transport in organic photovoltaic materials," *Accounts of Chemical Research*, vol. 42, no. 11, p. 1768, 2009.

[130] A. Saeki, Y. Koizumi, T. Aida, and S. Seki, "Comprehensive approach to intrinsic charge carrier mobility in conjugated organic molecules, macromolecules, and supramolecular architectures," *Accounts of Chemical Research*, vol. 45, no. 8, p. 1193, 2012.

[131] J. Cornil, S. Verlaak, N. Martinelli, A. Mityashin, Y. Olivier, T. Van Regemorter, G. D'Avino, L. Muccioli, C. Zannoni, F. Castet, *et al.*, "Exploring the energy landscape

of the charge transport levels in organic semiconductors at the molecular scale," *Accounts of Chemical Research*, vol. 46, no. 2, p. 434, 2012.

[132] T. Musho and N. Wu, "Ab initio calculation of electronic charge mobility in metal–organic frameworks," *Physical Chemistry Chemical Physics*, vol. 17, no. 39, p. 26160, 2015.

[133] J. Bardeen and W. Shockley, "Deformation potentials and mobilities in non-polar crystals," *Physical Review*, vol. 80, no. 1, p. 72, 1950.

[134] R. S. Sánchez-Carrera, S. Atahan, J. Schrier, and A. Aspuru-Guzik, "Theoretical characterization of the air-stable, high-mobility dinaphtho[2,3-b:2,3-f]thieno[3,2-b]-thiophene organic semiconductor," *The Journal of Physical Chemistry C*, vol. 114, no. 5, p. 2334, 2010.

[135] J. C. Slater, "The theory of complex spectra," *Physical Review*, vol. 34, no. 10, p. 1293, 1929.

[136] E. Condon, "The theory of complex spectra," *Physical Review*, vol. 36, no. 7, p. 1121, 1930.

[137] P.-O. Löwdin, "On the non-orthogonality problem connected with the use of atomic wave functions in the theory of molecules and crystals," *The Journal of Chemical Physics*, vol. 18, no. 3, p. 365, 1950.

[138] C. Schober, K. Reuter, and H. Oberhofer, "Critical analysis of fragment-orbital dft schemes for the calculation of electronic coupling values," *The Journal of Chemical Physics*, vol. 144, no. 5, p. 054103, 2016.

[139] W. Brütting and C. Adachi, *Physics of Organic Semiconductors*. New York: John Wiley & Sons, 2012.

[140] A. J. Heeger, "Semiconducting polymers: the third generation," *Chemical Society Reviews*, vol. 39, no. 7, p. 2354, 2010.

[141] S. R. Chaudhari, J. M. Griffin, K. Broch, A. Lesage, V. Lemaur, D. Dudenko, Y. Olivier, H. Sirringhaus, L. Emsley, and C. P. Grey, "Donor–acceptor stacking arrangements in bulk and thin-film high-mobility conjugated polymers characterized using molecular modelling and mas and surface-enhanced solid-state nmr spectroscopy," *Chemical Science*, vol. 8, no. 4, p. 3126, 2017.

[142] A. D. Becke, "Density-functional thermochemistry. III. the role of exact exchange," *The Journal of Chemical Physics*, vol. 98, no. 7, p. 5648, 1993.

[143] C. F. Guerra, J. Snijders, G. T. te Velde, and E. Baerends, "Towards an order-n DFT method," *Theoretical Chemistry Accounts*, vol. 99, no. 6, p. 391, 1998.

[144] E. J. Baerends, T. Ziegler, A. J. Atkins, J. Autschbach, D. Bashford, O. Baseggio, A. Bérces, F. M. Bickelhaupt, C. Bo, P. M. Boerritger, L. Cavallo, C. Daul, D. P. Chong, D. V. Chulhai, L. Deng, R. M. Dickson, J. M. Dieterich, D. E. Ellis, M. van Faassen, A. Ghysels, A. Giammona, S. J. A. van Gisbergen, A. Goez, A. W. Götz, S. Gusarov, F. E. Harris, P. van den Hoek, Z. Hu, C. R. Jacob, H. Jacobsen, L. Jensen, L. Joubert, J. W. Kaminski, G. van Kessel, C. König, F. Kootstra, A. Kovalenko, M. Krykunov, E. van Lenthe, D. A. McCormack, A. Michalak, M. Mitoraj, S. M. Morton, J. Neugebauer, V. P. Nicu, L. Noodleman, V. P. Osinga, S. Patchkovskii, M. Pavanello, C. A. Peeples, P. H. T. Philipsen, D. Post, C. C. Pye, H. Ramanantoanina, P. Ramos, W. Ravenek, J. I. Rodríguez, P. Ros, R. Rüger, P. R. T. Schipper, D. Schlüns, H. van Schoot, G. Schreckenbach, J. S. Seldenthuis, M. Seth, J. G. Snijders, M. Solà, S. M., M. Swart, D. Swerhone, G. te Velde, V. Tognetti, P. Vernooijs, L. Versluis, L. Visscher, O. Visser, F. Wang, T. A. Wesolowski, E. M. van Wezenbeek, G. Wiesenekker, S. K. Wolff, T. K. Woo, and A. L. Yakovlev, "ADF2017, SCM, Theoretical Chemistry, Vrije Universiteit, Amsterdam, The Netherlands, https://www.scm.com."

[145] A. M. Köster, R. Flores, G. Geudtner, A. Goursot, T. Heine, S. Patchkovskii, J. U. Reveles, A. Vela, and D. Salahub, "deMon, Version 1.2. Technical Report, 2004."

[146] M. W. Schmidt, K. K. Baldridge, J. A. Boatz, S. T. Elbert, M. S. Gordon, J. H. Jensen, S. Koseki, N. Matsunaga, K. A. Nguyen, S. Su, *et al.*, "General atomic and molecular electronic structure system," *Journal of Computational Chemistry*, vol. 14, no. 11, p. 1347, 1993.

[147] B. Aradi, B. Hourahine, and T. Frauenheim, "Dftb+, a sparse matrix-based implementation of the dftb method," *The Journal of Physical Chemistry A*, vol. 111, no. 26, p. 5678, 2007.

[148] R. Luschtinetz, *Theoretical studies towards a ferroelectric organic field-effect transistor based on functional thiophene molecules*. PhD thesis, Technischen Universität Dresden, 2012.

[149] R. Luschtinetz and G. Seifert, "Theoretical studies on the structural and electronic properties of π-stacked cyano-thiophene-based molecules," *Computational and Theoretical Chemistry*, vol. 1023, p. 65, 2013.

[150] S. Samdal, E. J. Samuelsen, and H. V. Volden, "Molecular conformation of 2, 2-bithiophene determined by gas phase electron diffraction and ab initio calculations," *Synthetic Metals*, vol. 59, no. 2, p. 259, 1993.

[151] V. Lukeš, J. Rimarčík, L. Rottmannová, K. Punyain, E. Klein, and A.-M. Kelterer, "On the applicability of the molecular dynamics scc-dftb treatment on optical spectra simulations for thiophene and phenyl containing oligomers," *Computational and Theoretical Chemistry*, vol. 999, p. 55, 2012.

[152] G. Visser, G. Heeres, J. Wolters, and A. Vos, "Disorder in crystals of the dithienyls and β-thiophenic acid," *Acta Crystallographica Section B: Structural Crystallography and Crystal Chemistry*, vol. 24, no. 4, p. 467, 1968.

[153] M. Lackinger, "On-surface polymerization–a versatile synthetic route to two-dimensional polymers," *Polymer International*, vol. 64, no. 9, p. 1073, 2015.

[154] F. Eisenhut, T. Lehmann, A. Viertel, D. Skidin, J. KruÌĹger, S. Nikipar, D. A. Ryndyk, C. Joachim, S. Hecht, F. Moresco, *et al.*, "On-surface annulation reaction cascade for the selective synthesis of diindenopyrene," *ACS Nano*, vol. 11, no. 12, p. 12419, 2017.

[155] J. Krüger, F. Eisenhut, T. Lehmann, J. M. Alonso, J. Meyer, D. Skidin, R. Ohmann, D. A. Ryndyk, D. PeÌĄrez, E. GuitiaÌĄn, *et al.*, "Molecular self-assembly driven by on-surface reduction: Anthracene and tetracene on au (111)," *The Journal of Physical Chemistry C*, vol. 121, no. 37, p. 20353, 2017.

[156] D. Skidin, O. Faizy, J. KruÌĹger, F. Eisenhut, A. Jancarik, K.-H. Nguyen, G. Cuniberti, A. Gourdon, F. Moresco, and C. Joachim, "Unimolecular logic gate with classical input by single gold atoms," *ACS nano*, vol. 12, no. 2, p. 1139, 2018.

[157] M. I. Muglali, A. Erbe, Y. Chen, C. Barth, P. Koelsch, and M. Rohwerder, "Modulation of electrochemical hydrogen evolution rate by araliphatic thiol monolayers on gold," *Electrochimica Acta*, vol. 90, p. 17, 2013.

[158] Y. Kim, T. J. Hellmuth, D. Sysoiev, F. Pauly, T. Pietsch, J. Wolf, A. Erbe, T. Huhn, U. Groth, U. E. Steiner, *et al.*, "Charge transport characteristics of diarylethene photoswitching single-molecule junctions," *Nano Letters*, vol. 12, no. 7, p. 3736, 2012.

[159] J. A. Boscoboinik, R. R. Kohlmeyer, J. Chen, and W. T. Tysoe, "Efficient transport of gold atoms with a scanning tunneling microscopy tip and a linker molecule," *Langmuir*, vol. 27, no. 15, p. 9337, 2011.

[160] M. Wykes, B. Milián-Medina, and J. Gierschner, "Computational engineering of low bandgap copolymers," *Frontiers in Chemistry*, vol. 1, p. 35, 2013.

[161] T. Dutta, K. B. Woody, S. R. Parkin, M. D. Watson, and J. Gierschner, "Conjugated polymers with large effective stokes shift: benzobisdioxole-based poly(phenylene ethynylene)s," *Journal of the American Chemical Society*, vol. 131, no. 47, p. 17321, 2009.

[162] Z. Zhao, Z. Wang, C. Ge, X. Zhang, X. Yang, and X. Gao, "Incorporation of benzothiadiazole into the backbone of 1, 2, 5, 6-naphthalenediimide based copolymers, enabling much improved film crystallinity and charge carrier mobility," *Polymer Chemistry*, vol. 7, no. 3, p. 573, 2016.

[163] G. Zhang, Y. Dai, K. Song, H. Lee, F. Ge, L. Qiu, and K. Cho, "Bis(2-oxo-7-azaindolin-3-ylidene)benzodifuran-dione-based donor–acceptor polymers for high-performance n-type field-effect transistors," *Polymer Chemistry*, vol. 8, no. 15, p. 2381, 2017.

[164] R. G. Brandt, W. Yue, T. R. Andersen, T. T. Larsen-Olsen, M. Hinge, E. Bundgaard, F. C. Krebs, and D. Yu, "An isoindigo containing donor–acceptor polymer: synthesis and photovoltaic properties of all-solution-processed ito-and vacuum-free large area roll-coated single junction and tandem solar cells," *Journal of Materials Chemistry C*, vol. 3, no. 8, p. 1633, 2015.

[165] F. Parenti, F. Tassinari, E. Libertini, M. Lanzi, and A. Mucci, "π-stacking signature in nmr solution spectra of thiophene-based conjugated polymers," *ACS Omega*, vol. 2, no. 9, pp. 5775–, 2017.

[166] "On the effect of prevalent carbazole homocoupling defects on the photovoltaic performance of [pcdtbt:pc71bm,"

[167] F. Lombeck, H. Komber, S. I. Gorelsky, and M. Sommer, "Identifying homocouplings as critical side reactions in direct arylation polycondensation," *ACS Macro Letters*, vol. 3, no. 8, p. 819, 2014.

[168] S. Broll, F. Nübling, A. Luzio, D. Lentzas, H. Komber, M. Caironi, and M. Sommer, "Defect analysis of high electron mobility diketopyrrolopyrrole copolymers made by direct arylation polycondensation," *Macromolecules*, vol. 48, no. 20, p. 7481, 2015.

[169] R. Baughman and R. Chance, "Point defects in fully conjugated polymers," *Journal of Applied Physics*, vol. 47, no. 10, p. 4295, 1976.

[170] Z. Liang, A. Nardes, D. Wang, J. J. Berry, and B. A. Gregg, "Defect engineering in π-conjugated polymers," *Chemistry of Materials*, vol. 21, no. 20, p. 4914, 2009.

[171] H. Sirringhaus, P. Brown, R. Friend, M. M. Nielsen, K. Bechgaard, B. Langeveld-Voss, A. Spiering, R. A. Janssen, E. Meijer, P. Herwig, *et al.*, "Two-dimensional charge transport in self-organized, high-mobility conjugated polymers," *Nature*, vol. 401, no. 6754, p. 685, 1999.

[172] B. McCulloch, V. Ho, M. Hoarfrost, C. Stanley, C. Do, W. T. Heller, and R. A. Segalman, "Polymer chain shape of poly(3-alkylthiophenes) in solution using small-angle neutron scattering," *Macromolecules*, vol. 46, no. 5, p. 1899, 2013.

[173] M. Böckmann, T. Schemme, D. H. de Jong, C. Denz, A. Heuer, and N. L. Doltsinis, "Structure of P3HT crystals, thin films, and solutions by uv/vis spectral analysis," *Physical Chemistry Chemical Physics*, vol. 17, no. 43, p. 28616, 2015.

[174] J.-L. Brédas, D. Beljonne, V. Coropceanu, and J. Cornil, "Charge-transfer and energy-transfer processes in π-conjugated oligomers and polymers: a molecular picture," *Chemical Reviews*, vol. 104, no. 11, p. 4971, 2004.

[175] G. R. Hutchison, M. A. Ratner, and T. J. Marks, "Intermolecular charge transfer between heterocyclic oligomers. effects of heteroatom and molecular packing on hopping transport in organic semiconductors," *Journal of the American Chemical Society*, vol. 127, no. 48, p. 16866, 2005.

[176] K. Sun, X. Tang, Y. Ran, R. He, W. Shen, and M. Li, "π-bridge modification of thiazole-bridged DPP polymers for high performance near-IR OSCs," *Physical Chemistry Chemical Physics*, vol. 20, no. 3, p. 1664, 2018.

[177] T. A. Niehaus, M. Elstner, T. Frauenheim, and S. Suhai, "Application of an approximate density-functional method to sulfur containing compounds," *Journal of Molecular Structure: THEOCHEM*, vol. 541, no. 1, p. 185, 2001.

[178] A. Förster, F. Günther, S. Gemming, and G. Seifert, "Influence of electric fields on the electron transport in donor–acceptor polymers," *The Journal of Physical Chemistry C*, vol. 121, no. 7, p. 3714, 2017.

[179] T. Liu and A. Troisi, "Understanding the microscopic origin of the very high charge mobility in PBTTT: Tolerance of thermal disorder," *Advanced Functional Materials*, vol. 24, no. 7, p. 925, 2014.

[180] A. Troisi, "Charge transport in high mobility molecular semiconductors: Classical models and new theories," *Chemical Society Reviews*, vol. 40, no. 5, p. 2347, 2011.

[181] A. Troisi, "The speed limit for sequential charge hopping in molecular materials," *Organic Electronics*, vol. 12, no. 12, p. 1988, 2011.

[182] B. Lüssem, M. Riede, and K. Leo, "Doping of organic semiconductors," *Physica Status Solidi (a)*, vol. 210, no. 1, p. 9, 2013.

[183] P. Wei, J. H. Oh, G. Dong, and Z. Bao, "Use of a 1 h-benzoimidazole derivative as an n-type dopant and to enable air-stable solution-processed n-channel organic thin-film transistors," *Journal of the American Chemical Society*, vol. 132, no. 26, p. 8852, 2010.

[184] Y. Karpov, T. Erdmann, I. Raguzin, M. Al-Hussein, M. Binner, U. Lappan, M. Stamm, K. L. Gerasimov, T. Beryozkina, V. Bakulev, and F. Günther, "High conductivity in molecularly p-doped diketopyrrolopyrrole-based polymer: The impact of a high dopant strength and good structural order," *Advanced Materials*, vol. 28, no. 28, p. 6003, 2016.

[185] E. F. Aziz, A. Vollmer, S. Eisebitt, W. Eberhardt, P. Pingel, D. Neher, and N. Koch, "Localized charge transfer in a molecularly doped conducting polymer," *Advanced Materials*, vol. 19, no. 20, p. 3257, 2007.

[186] F. Zhang and A. Kahn, "Investigation of the high electron affinity molecular dopant F6-TCNNQ for hole-transport materials," *Advanced Functional Materials*, vol. 28, no. 1, 2018.

[187] B. Lüssem, M. L. Tietze, H. Kleemann, C. Hoßbach, J. W. Bartha, A. Zakhidov, and K. Leo, "Doped organic transistors operating in the inversion and depletion regime," *Nature Communications*, vol. 4, p. 2775, 2013.

[188] M. L. Tietze, L. Burtone, M. Riede, B. Lüssem, and K. Leo, "Fermi level shift and doping efficiency in p-doped small molecule organic semiconductors: a photoelectron spectroscopy and theoretical study," *Physical Review B*, vol. 86, no. 3, p. 035320, 2012.

[189] C. Weichsel, L. Burtone, S. Reineke, S. I. Hintschich, M. C. Gather, K. Leo, and B. Lüssem, "Storage of charge carriers on emitter molecules in organic light-emitting diodes," *Physical Review B*, vol. 86, no. 7, p. 075204, 2012.

[190] T. Fukunaga, "Negatively substituted trimethylenecyclopropane dianions," *Journal of the American Chemical Society*, vol. 98, no. 2, p. 610, 1976.

[191] T. Fukunaga, M. D. Gordon, and P. J. Krusic, "Negatively substituted trimethylenecyclopropanes and their radical anions," *Journal of the American Chemical Society*, vol. 98, no. 2, p. 611.

[192] J. Gao, J. D. Roehling, Y. Li, H. Guo, A. J. Moulé, and J. K. Grey, "The effect of 2,3,5,6-tetrafluoro-7,7,8,8-tetracyanoquinodimethane charge transfer dopants on the conformation and aggregation of poly(3-hexylthiophene)," *Journal of Materials Chemistry C*, vol. 1, no. 36, p. 5638, 2013.

[193] L. Zhu, E.-G. Kim, Y. Yi, and J.-L. Brédas, "Charge transfer in molecular complexes with 2,3,5,6-tetrafluoro-7,7,8,8-tetracyanoquinodimethane (F4-TCNQ): A density functional theory study," *Chemistry of Materials*, vol. 23, no. 23, p. 5149, 2011.

[194] A. B. Padmaperuma, "Substituted molecular p-dopants: a theoretical study," *Advances in Materials Physics and Chemistry*, vol. 2, no. 03, p. 163, 2012.

[195] Y. Karpov, T. Erdmann, M. Stamm, U. Lappan, O. Guskova, M. Malanin, I. Raguzin, T. Beryozkina, V. Bakulev, F. Günther, *et al.*, "Molecular doping of a high mobility diketopyrrolopyrrole–dithienylthieno[3, 2-b]thiophene donor–acceptor copolymer with F6TCNNQ," *Macromolecules*, vol. 50, no. 3, p. 914, 2017.

[196] T. Erdmann, *High Charge Carrier Mobility Polymers for Organic Transistors*. PhD thesis, Technischen Universität Dresden, 2017.

[197] Y. Karpov, *Solution Processable Conducting Films based on Doped Polymers: Synthesis and Characterization*. PhD thesis, Technischen Universität Dresden, 2017.

[198] C. B. Nielsen, M. Turbiez, and I. McCulloch, "Recent advances in the development of semiconducting dpp-containing polymers for transistor applications," *Advanced Materials*, vol. 25, no. 13, p. 1859, 2013.

[199] K. E. Edgecombe and R. J. Boyd, "Atomic orbital populations and atomic charges from self-consistent field molecular orbital wavefunctions," *Journal of the Chemical Society, Faraday Transactions 2: Molecular and Chemical Physics*, vol. 83, no. 8, p. 1307, 1987.

[200] F. L. Hirshfeld, "Bonded-atom fragments for describing molecular charge densities," *Theoretical Chemistry Accounts: Theory, Computation, and Modeling (Theoretica Chimica Acta)*, vol. 44, no. 2, p. 129, 1977.

[201] V. Rühle and C. Junghans, "Hybrid approaches to Coarse–Graining using the VOTCA package: Liquid hexane," 2011.

[202] V. Rühle, A. Lukyanov, F. May, M. Schrader, T. Vehoff, J. Kirkpatrick, B. Baumeier, and D. Andrienko, "Microscopic simulations of charge transport in disordered organic semiconductors," *Journal of Chemical Theory and Computation*, 2011.

[203] V. Rühle, C. Junghans, A. Lukyanov, K. Kremer, and D. Andrienko, "Versatile Object-Oriented toolkit for Coarse-Graining applications," *Journal of Chemical Theory and Computation*, vol. 5, no. 12, p. 3211, 2009.

LIST OF OWN PUBLICATIONS

[1] **F. Günther**, S. Gemming, and G. Seifert, "Hopping–Based Charge Transfer in Diketopyrrolopyrrole-Based Donor–Acceptor Polymers: A Theoretical Study." *The Journal of Physical Chemistry C*, vol. 120, no. 18, p. 9581, 2016.

[2] Y. Karpov, T. Erdmann, I. Raguzin, M. Al-Hussein, M. Binner, U. Lappan, M. Stamm, K. L. Gerasimov, T. Beryozkina, V. Bakulev, D. V. Anokhin, D. A. Ivanov, **F. Günther**, S. Gemming, G. Seifert, B. Voit, R. Di Pietro, and A. Kiriy, "High Conductivity in Molecularly p-Doped Diketopyrrolopyrrole-Based Polymer: The Impact of a High Dopant Strength and Good Structural Order." *Advanced Materials*, vol. 28, no. 28, p. 6003, 2016.

[3] A. Förster, **F. Günther**, S. Gemming, and G. Seifert, "Influence of Electric Fields on the Electron Transport in Donor–Acceptor Polymers." *The Journal of Physical Chemistry C*, vol. 121, no. 7, p. 3714, 2017.

[4] Y. Karpov, T. Erdmann, M. Stamm, U. Lappan, O. Guskova, M. Malanin, I. Raguzin, T. Beryozkina, V. Bakulev, **F. Günther**, S. Gemming, G. Seifert, M. Hambsch, S. Mannsfeld, B. Voit, A. Kiriy, "Molecular Doping of a High Mobility Diketopyrrolopyrrole-Dithienylthieno[3, 2-b]thiophene Donor–Acceptor Copolymer with F6TCNNQ." *Macromolecules*, vol. 50, no. 3 , p. 914, 2017.

[5] **F. Günther**, A. Möbius, and M. Schreiber. "Structure Optimisation by Thermal Cycling for the Hydrophobic-Holar Lattice Model of Protein Folding." *The European Physical Journal Special Topics*, vol. 226, no. 4, p. 639, 2017.

Lists of Figures, Tables, and Abbreviations

LIST OF FIGURES

1.1 Most common representatives of the 1st, 2nd and 3rd generation of SCP. . 5
1.2 Energy level diagram of 2T, NDI, PT, PNDI, and P(NDI-2T) 6
1.3 Schematic sketch of the two models used to describe molecular p-doping. 7

3.1 Schematic plot of the transition from an energetic state of a monomer to the electronic band structure of an one-dimensional periodic structure. . . . 17
3.2 Schematic presentation of the electronic bands of metals, insulators and semiconductors. 18

4.1 Schematic plot of the two energy surfaces for the states $|\mu\rangle$ and $|\nu\rangle$ where the charge is either on *A* or *B*, respectively. Squares indicate the geometry of the charged fragments whereas circles represent those of the neutral states. The black dot stands for the charge which is transferred from *A* to *B*. 32

5.1 Labeling of the bond lengths (red) and bond angles (green) in *trans* (a) and *cis* (b) orientations. 41
5.2 Energy landscape for turning the thiophene rings in TDPP monomers. . . . 43
5.3 a) 2T in *cis* (left) and *trans* (right) configurations and b) Top (left)and side (right) view of 2TT model in *cis* orientation. c) Energy landscape for rotating the units from the *cis* (0°) to the *trans* (180°) configuration obtained using DFT with VWN and PBE functionals and DFTB. 44
5.4 Energy per twisted bond relative to the planar-*trans* configuration for different oligomer lengths *n* when rotating the central unit only (version A, left), twisting the chain (version B, center) or performing rotation in alternating directions (version C, right). 47
5.5 Labeling of the dihedral angle for oTT models. 48
5.6 Model of π-π stacked 3TT chains. 49

5.7 Energy landscape when one chain is shifted on top of the other for parallel (green) and antiparallel (red). 49
5.8 Interaction energy of two stacked 3TT chains for different dihedral angles φ in dependence of the stacking distance z. 50
5.9 STM image of P(DPP-2T) fabricated via on surface polymerization and Schematic plot how the positioning of two adjacent lines are translated into four distances d_i (dashed lines), four wide angles α_i (purple) and for small angles β_i (yellow). 51
5.10 Histograms of the distances (left) and angles α (right, purple) and β (right, yellow) obtained from Fig. 5.9. 51
5.11 Possible configurations for DPP-2T-DPP defining the relative positioning of neighboring DPP units. 52
5.12 STM images of P(DPP-2T) superimposed by DPP-2T-DPP models. 53
5.13 Top and side view of the structure (a), the HOMO (b) and the LUMO (c) of the TDPP-TT monomer in *trans*/*trans* configuration 54
5.14 Comparison of the HOMO and the LUMO energies obtained by different DFT functionals and DFTB for different configuration of TDPP-TT monomer. 55
5.15 MO diagram for TDPP-TT oligomers of different lengths and band structure of the infinite polymer. 57
5.16 Total DOS (black line) and pDOS the thiophenes T_1 and T_2 (green), the DPP (red) and the TT (blue) for P(TDPP-TT). 58
5.17 Top: pDOS of individual units of the TDPP-TT 9-mer model in comparison with the DOS of the 9-mer (black) and the DOS of an infinite chain (red). Bottom: Isosurface plot of HOMO and LUMO wave function as well as the localized in-gab state. 59

6.1 General structure of considered DA polymer models and systems considered for the donor unit. 61
6.2 The TDPP-TT model in *trans*/*trans* (a), *cis*/*trans* (b), *trans*/*cis* (c) and *cis*/*cis* (d) configurations. 63
6.3 Schematic sketch of considered π-π stacks. 65
6.4 Schematic sketch of the total energy for neutral, anionic and cationic state and Reorganization energies λ_0^{+1} , λ_{+1}^0 , λ_{-1}^0, and λ_0^{-1} for TDPP-T (□), TDPP-TT (○), TDPP-2T (△) and TDPP-TET (▽) in dependence of monomer length. 66
6.5 Interaction energies and the coupling elements for hole and electron transfer for parallel (a) and antiparallel (b) stacked chains in *trans*/*trans* configuration and isosurface plots of HOMO and LUMO (c). 67
6.6 Same as Figure 6.5 for *cis*/*trans* configuration. 68
6.7 Same as Figure 6.5 for *trans*/*cis* configuration. 69
6.8 Same as Figure 6.5 for *cis*/*cis* configuration. 70

7.1 Molecular structures of the considered p-dopants. 78
7.2 Experimentally measured conductivities for P(TDPP-TT) when doped with F4-TCNQ, F6-TCNNQ or CN6-cP in different MDRs of dopant and repeat unit of the DA polymer. 79
7.3 UV-vis spectra for P(TDPP-TT) films doped by CN6-cP at different MDRs as well as of the neat P(TDPP-TT) and CN6-cP. 80
7.4 Molecular structures of the considered P(TDPP-TT) models. 81
7.5 Energy level diagram for different p-dopants (left) and polymer models (right) as obtained from B3LYP calculations with DZP basis. 82
7.6 Charge transfer (left scale) as obtained using Mulliken (red), Hirshfeld (green), Voronoi (blue) population analyses and complex formation energies (black, right scale) when F6-TCNQ is placed on TT (a) or DPP (b) moieties. . 83
7.7 Calculated charge transfer and energy for the CT complex CN6-cP:2(TDPP-TT) for a stacking distance of 3 Å. 85
7.8 Isosurface plot of the LUMO of CN6-cP dopant and the HOMO of 2(TDPP-TT). 85
7.9 MO energy level diagram of the frontier orbitals for CN6-cP and TDPP-TT before and after formation of the CT complex. 87
7.10 Isosurface plots and irreproducible representation of LUMO of F4-TCNQ and F6-TCNNQ and HOMO of P(TDPP-TT) models. 89
7.11 Energy level diagram (bottom) and wave function populations for HOMO (lower central), LUMO (upper central) and LUMO+1 (top) of F6-TCNNQ on top of TT (left) and DPP (right) units in dependency on the rotational orientation. 90

B.1 TDPP-TT polymer chain (left) translated into a simple quantum well structure (right). 108
B.2 Electronic levels for finite quantum well structure of different number *n* of repeat units and Density of states. 108
B.3 Comparison of the DOS of the finite system consisting of 9 successive units and the infinite model. 109
B.4 Selected wave functions of the quantum well structure which consists of nine repeat units. 110

C.1 Representation of the alignment and the considered displacements for evaluate the coupling. 111
C.2 Dependence of the coupling element between two π-stacked thiophenes on rotation δ as well as shifts in x, y and z direction. 112
C.3 Same as Fig. C.2 for pyrrol dimer. 112
C.4 Same as Fig. C.2 for DPP dimer. 113
C.5 Same as Fig. C.2 for T-TT-T dimer. 113

C.6 Comparison of coupling elements of holes (green) and electrons (red) as obtained from FO-DFT using SCM ADF and the own FO-DFTB implementation based on the output of DFTB+ for the molecules discussed above. The lack line indicates the identity whereas the dashed lines give the correlation for T_{AB}^{h} and T_{AB}^{e}. 114

E.1 Calculated charge transfer and energy for the CT complex F4-TCNQ:4T complexes for a stacking distance of 3 Å. 118

LIST OF TABLES

4.1 Overview of further approximations for the geometry the elecronic density. 36

5.1 Bond lengths of TDPP monomer models in *cis* and *trans* configurations as obtained from DFT using different functionals and DFTB. The labeling is according to Fig. 5.1. 42

5.2 Bond angles of TDPP monomer models in *cis* and *trans* configurations as obtained from DFT using different functionals and DFTB. The labeling is according to Fig. 5.1. 42

5.3 Stability of the planar and the optimal-*cis* as well as of the optimal-*trans* conformations compared to the planar-*trans* isomers for 2T and 2TT models. Optimized dihedral angles are given in brackets. 45

5.4 Optimal dihedral angles φ_i, energy difference with respect to the planar-*trans* structure and energy barrier $\Delta E_{\text{barrier}}$ per dihedral angle of oTT chains of length n as obtained using the PBE functional. For the numbering of the dihedral angles, see Fig. 5.5. Due to the symmetry of the chains each value, except φ_0, describes two dihedral angles of the oligomer model. . . 48

5.5 Distances and angles of the optimized structures as obtained from DFTB calculations. For this, the positions of the carbon atoms of the methyl groups were considered. For the numbering of the atoms, see Fig. 5.11. . 52

5.6 Contributions of the left thiophene (T_1), the DPP, the central thiophene (T_2) and the TT units to HOMO and LUMO wave functions according to the GOP obtained from DFT using VWN, PBE, B3LYP functionals with DZP basis sets as well as from DFTB using the mio-1.1 parameter sets. 56

5.7 Contribution of T_1, DPP, T_2 and TT to the wave functions with energies in the given ranges as obtained from summing up the GOPs of the atoms constituting the units. 58

6.1 Coupling elements as obtained from the most stable configuration $\vec{R}_{opt}$ and the average value approaches explained in the text. The maximum and minimum value of each approach is highlighted in bold. Values are given in meV. 73
6.2 Mean reorganization energy λ, minimal, maximal and RMS of $\sqrt{\langle T_{AB}^2 \rangle_{QB}}$ as obtained for the DPP based DA polymers considering thiophene, TT, 2T and TET as the donor unit. CT rate k and charge carrier mobility μ as obtained from Marcus formula and Einstein relation using $T = 300$K and $d = 3.5$ Å. 74

7.1 charge transfer averaged over different rotational orientations when the dopant is positioned above the DPP or the TT moiety. 84
7.2 Orbital resolved gross orbital population (GOP) and MO energies of LUMO+1, LUMO and HOMO for CT complexes with F4-TCNQ, F6-TCNNQ, or CN6-cP on top of DPP-TT-DPP or TT-DPP-TT fragments. . . 88

D.1 Same as Tab. 6.1 of P(TDPP-T). 115
D.2 Same as Tab. 6.1 of P(TDPP-2T). 116
D.3 Same as Tab. 6.1 of P(TDPP-TET). 116

E.1 Comparison of CT as obtained from Mulliken, Hirshfeld and Voronoi population analysis. 117

LIST OF ABBREVIATIONS

2T	2,2′-bithiophene
2TT	2,2′-bithieno[3,2-b]thiophene
3TT	2,2′:5′,2″-terthieno[3,2-b]thiophene
4T	quatrothiophene
AO	atomic orbital
B3LYP	Becke three-parameter, Lee-Yang-Parr
BT	benzothiadiazole
CN6-cP	hexacyano-trimethylene-cyclopropane
CPDT	cyclopenta-dithiophene
CT	charge transfer
CV	cyclovoltametry
DA	donor-acceptor
DFT	density functional theory
DFTB	density functional based tight binding
DOS	density of states
DPP	diketopyrrolo[3,4-c]pyrrole
DZ	double-zeta
DZP	double-zeta polarised

F4-TCNQ	tetrafluoro-tetracyano-quinodimethane
F6-TCNNQ	2,2-(perfluoronaphthalene-2,6-diylidene)dimalononitrile
FO	fragment-orbital
GGA	generalized gradient approximation
GOP	gross orbital population
GTO	Gaussian-type orbitals
HF	Hartree-Fock
HOMO	highest occupied molecular orbital
IR	infra-red
KS	Kohn-Sham
LCAO	linear combination of atomic orbitals
LDA	local density approximation
LUMO	lowest unoccupied molecular orbital
LYP	Lee-Yang-Parr
MD	molecular dynamic
MO	molecular orbital
MP2	second-order Møller-Plesset perturbation theory
MDR	molecular doping ratios
NDI	naphthalenetetracarboxylic diimide
OE	organic electronic
OFET	field-effect transistor
OLED	organic light-emitting diode
OSC	organic solar cell
oTT	oligo[thieno[3,2-b]thiophene]
P3AT	poly(3-alkylthiophene)
P3HT	poly(3-hexylthiophene)
P(CPDT-BT)	poly(cyclopenta-dithiophene-benzothiadiazole)

P(DPP-2T)	poly[3,6-(dithiophene-2-yl)-diketopyrrolo[3,4-c]pyrrole]
P(NDI-2T)	poly(naphthalenetetracarboxylic-diimide-bithiophene)
P(TDPP-TT)	poly[3,6-(dithiophene-2-yl)-diketopyrrolo[3,4-c]pyrrole-thieno[3,2-b]thiophene]
PA	polyacetylene
PANI	polyaniline
PBE	Perdew-Burke-Ernzerhof
pDOS	projected density of states
PEDOT	poly(ethylene dioxythiophene)
PNDI	poly(naphthalenetetracarboxylic-diimide)
PPP	poly(p-phenylene)
PPy	polypyrrole
PT	polythiophene
RMS	root mean square
RR′-PPV	poly(2,5-dialkoxy-p-phenylene vinylene)
SCC	self-consistent charge
SCP	semiconducting polymer
STM	scanning tunnel microscopy
STO	Slater-type orbitals
SZ	single-zeta
TDPP	3,6-(dithiophene-2-yl)-diketopyrrolo[3,4-c]pyrrole
TDPP-TT	3,6-(dithiophene-2-yl)-diketopyrrolo[3,4-c]pyrrole-thieno[3,2-b]thiophene
TET	1,2-di(2-thienyl)ethylene
TFB	tetra-fluorobenzene
TT	thieno[3,2-b]thiophene
TZ	triple-zeta
TZ2P	triple-zeta douple-polarised
TZP	triple-zeta polarised
VWN	Vosko-Wilk-Nusair
XC	exchange-correlation

SELBSTSTÄNDIGKEITSERKLÄRUNG

Hiermit versichere ich, dass ich die vorliegende Arbeit ohne unzulässige Hilfe Dritter und ohne Benutzung anderer als der angegebenen Hilfsmittel angefertigt habe; die aus fremden Quellen direkt oder indirekt übernommenen Gedanken sind als solche kenntlich gemacht. Die Arbeit wurde bisher weder im Inland noch im Ausland in gleicher oder ähnlicher Form einer anderen Prüfungsbehörde vorgelegt.

Die Dissertation wurde an der Technischen Universität Dresden (Bereich Mathematik und Naturwissenschaften, Professur für Theoretische Chemie) und dem Helmholtz-Zentrum Dresden-Rossendorf e.V. (Institut für Ionenstrahlphysik und Materialforschung) unter Anleitung von Prof. Dr. rer. nat. habil. Gotthard Seifert und Prof. Dr. rer. nat. habil. Sibylle Gemming angefertigt.

Datum, Unterschrift